UNIVERSITY OF CALIFORNIA

Los Angeles

Development of High-Quality Graphene and Composite Materials for Energy Storage

A dissertation submitted in partial satisfaction of the

requirements for the degree of Doctor of Philosophy

in Chemical Engineering

by

Ran Tao

2020

ABSTRACT OF THE DISSERTATION

Development of High-Quality Graphene and Composite Materials for Energy Storage

by

Ran Tao

Doctor of Philosophy Candidate in Chemical Engineering

University of California, Los Angeles, 2020

Professor Yunfeng Lu, Chair

The critical energy crisis and environmental pollution associated with the fast fossil fuels consumption has greatly motivated the research and development of clean energy. Up to date, increasing attention has been put into renewable energy sources such as wind, solar, tidal, biomass, and geothermal. However, these energy sources are intermittent and not stable in nature, which bring an advanced energy storage system on request. The electrochemical energy storage (EES) system is considered very promising for effective and efficient usage of clean energy and therefore has been intensively investigated during past decades.

Lithium ion batteries (LIBs) are the most ubiquitous energy storage system among EES, which is commonly used in portable electronic devices and electric vehicles, due to their long cycle life, high energy density, and high stability. However, most cathodes (e.g. lithium-insertion compounds)

and anodes (e.g. graphite and silicon) suffer from either low intrinsic electrical conductivity or poor lithium diffusivity, limiting the power density of LIBs. To date, constructing a matrix with high electrical conductivity and Li^+ diffusion rate to form composite electrodes is one of the most effective ways to address the current challenges.

Carbon materials with excellent intrinsic conductivity and good designability are a good candidate to be applied in the composite electrode. Particularly, graphene is proposed as a conductive agent or act as a carbon matrix to form a composite electrode with other active electrode materials due to its excellent electron conductivity (2000 S cm^{-1})[1], high surface area (2630 m^2 g^{-1})[2] and high ambipolar charge-carrier mobility (10^5 cm^2 V^{-1} s^{-1})[3]. Such graphene composite electrodes are generally synthesized through a direct assembly or bottom-up growth, of which the former approach disperses graphene (or perhaps graphene oxide) with a precursor or an active material itself followed by a hydrothermal or spray-dry methods respectively to assemble the composites, while the later approach converts carbon precursor to graphene on the surface of active materials through chemical vapour deposition (CVD).

The direct assembly approach needs graphene with high dispersity which is associated with the degree of functionalization. However, such functionalized groups lead to defects and low conductivity. Despite the extensive efforts made, making graphene with both high conductivity and dispersibility remains challenging. The bottom-up growth approach usually applied the "substrate-graphene" after CVD to produce composite material or directly use it as an active material for LIBs. However, such precursors or active materials mostly have inappropriate catalytic property or cannot catalyze the formation of high-quality graphene at all, which gives a strict restriction on choosing substrates.

In this dissertation, we design and synthesize an edge-functionalized graphene with large lateral size (10 μm) to address the paradox of the direct assembly approach, such that the functional groups in the edge can provide the graphene with high dispersibility (10 mg mL^{-1} in water), while the well-retained graphene structure in the basal plane can provide the graphene with high conductivity (924 S cm^{-1}). The edge-functionalized graphene can be readily synthesized using an edge-to-interior exfoliation strategy based on controllable catalytic reaction between H_2O_2 and $FeCl_3$-graphite intercalation compound, which improves processing capability in composite fabrication and enables excellent conductivity as a conductive network in batteries.

Such edge-oxidized graphene (eoG) was then complexed with commercial $LiFePO_4$ as an example of its broad applications through a spray drying method. During the synthetical process, the large-size eoG anchored with commercial LFP nanoparticles folds, twists and encapsulates into spherical LFP-eoG composite, which minimize the lithium ion diffusion length, as well as the contact resistance between stacked graphene network and LFP, enabling effective transport of Li^+ and electrons. Such LFP-eoG composite cathode exhibits high reversible capacity (159.9 mA h g-1 at 0.5 C) and excellent rate performance (76.6 mA h g^{-1} at 20 C), which is 12 folds higher than LFP-GO with the same carbon content and 16 folds higher than commercial LFP (our primary particles of LFP-eoG). Moreover, the dense spherical morphology contributes to a higher tap density (1.2 g cm^{-3}), enabling high volumetric capacity of LFP-eoG composite electrodes (e.g. 193.8 mA h mL^{-1} at 0.5 C and 91 mA h mL^{-1} at 20 C).

Inspired by the graphite intercalation compounds (GICs) route to obtain eoG, we fabricate carbon nanotubes (CNTs) embedded graphite anode for high-power LIBs. Such CNT-graphite anode was synthesized through an intercalation of catalyst into graphite interlayers and the following CVD growth of CNTs. These embedded CNTs expand the interlayer spacing of graphite

and act as a transit reservoir for Li^+, which improve the lithium ion diffusion rate as well as electrical conductivity, enabling high reversible capacity (291.9 mA h g^{-1} at 1 C) and good rate performance (61.1 mAh g^{-1} at 5 C) for lithium ion batteries.

The dissertation of Ran Tao is approved.

Dante A. Simonetti

Vasilios Manousiouthakis

Yang Yang

Yunfeng Lu, Committee Chair

University of California, Los Angeles

2020

TO MY FAMILY

Contents

LIST OF FIGURES

LIST OF TABLES

Acknowledgements

Words are powerless to express my gratitude to so many people who have helped me to make my way here. During this doctoral journey, not only did I lean how to think as a researcher, but also leant how to live a life. I would not have gotten this far without them, so I would like to run out of my words to thank them all.

Firstly, I would like to express my deepest appreciation to my advisor, Professor Yunfeng Lu. I would not have leant so much without your guidance, patience, encouragement and endless support. Among Dr. Lu's numerous merits, I admire most for his passion towards science throughout his career and perseverance of all time. With such never-ending passion, Dr. Lu have spread his research from energy storage to life science, moved from science to industry, always going forward to address new challenges. And his perseverance has encouraged him to persist through all the hard time without self-doubt, leading him to the highest level. He set such a great example to me not only about the research but also about the life. Although I am far away from those outstanding students he has taught, I promise him, no matter what I am going to do, I will not let him down.

I would like to thank my doctoral committee members, Professor Yang Yang, Professor Vasilios Manousiouthakis and Professor Dante Simonetti. It is your insight questions and enlightening suggestions that helped me to think from different perspective and shape the frame of my PhD research. I leant a lot from the paper of Professor Yang's group about the graphene production and characterization. I leant from Professor Manousiouthakis to be strict about research while be happy about life. I also want to thank Professor Simonetti for his patience when I first came to UCLA, speaking a non-fluent English.

I would like to express my gratefulness for my undergraduate advisor, Professor Lin Guo and Professor Lidong Li, who gave me instruction and guidance when I did the first project. I also want to thank Dr. Yi Peng, who trained me with experimental skills and critical thinking. My undergraduate research experience was very helpful which built a good foundation for my PhD research.

I would like to express my sincerest appreciation to Dr. Runwei Mo, who joined Lu group as postdoc when we need him most and stayed firmly with the Lu group graphene team of all time. His broad knowledge, high moral standing, and strong responsibility help me to overcome every challenge throughout my doctoral journey. He has dedicated a lot coaching me in research and we experienced a lot together which helps me grow. I firmly believe you will become an excellent faculty in the near future.

To my dear other Lu group members and friends, it has been a great experience to work with and learn from them during these five years. You all make Lu group feels like a big family. I am proud to join this big family and I cherish the time we have been together. I would like to thank Dr. Fang Liu who helped me a lot when I first started the research in our group. I would like to express my appreciation to Dr. Gen Chen and Dr. Lu Zhang for your kind and patient instruction on experimental details. I would like to thank Dr. Zaiyuan Le, Dr. Li Shen, Dr. Gurong Shen, Dr. Xianyang Li for their kind help in research. I want to thank Chen Zhang, not only for his suggestion and help towards research, but also for winning the 16 times championships of battle cups together over the five years. I would also like to thank Dejia Kong, Shengxiang Ma, Jinhui Xu, Xinyi Tan and Wenyue Shi for helping me with the experiments and giving so much happy time in the lab. I also want to thank Dr. Xilai Jia, Dr. Xiao Zhu, Dr. Di Wu, Dr. Duo Xu, Xing Lu, Kang Peng,

Xinru Li, Jie Ren, Zhiyong Wang and etc. Thank you for all the good time in lab, office, classrooms and esports games.

I am deeply indebted to my parents, for their love, support and education. My father is a great man who experienced tough but legendary story throughout his study and career life. He taught me so much from math problems to methodology, but most importantly, how to be a man. They already have given me far more than I will ever be able to pay back. This dissertation is dedicated to my family.

Finally, I would express my special appreciations to my wife, Sijin Wang for her understanding, support and encouragement. We met at UCLA; it seems all I have done in my first 22 years was making my way here to you. I never thought the everything we experienced would happen in my own life just like the movie. Thank you for breaking in my life.

VITA

2011 – 2015	B.S., School of Chemistry Beihang University, China
2015 – 2020	Teaching Assistant, Graduate Researcher Department of Chemical and Biomolecular Engineering University of California, Los Angeles, USA
2019-2020	Graduate Division Award Department of Chemical and Biomolecular Engineering University of California, Los Angeles, USA
2018-2019	Member Materials Research Society

Chapter 1 Introduction and background

1.1 Energy storage

Energy is an essential commodity which keeps the human society moving. Although energy has numerous forms in nature, it can be sorted into two kinds: primary energy and secondary energy (Figure 1.1). Primary energy includes energy forms that can be found in nature without any conversion or transformation process (e.g. crude oil, coal, biomass, wind, solar, tidal, falling and flowing water, natural gas and etc.), while secondary energy are energy forms that are the results of the transformation of primary energy through energy conversion processes (e.g. electricity, gasoline, diesel, hydrogen, heat and etc.)[4]. However, most of the primary energy are non-renewable which cause the energy crisis with the fast fossil fuels consumption and increase the greenhouse gas emission associated with environmental pollution. Such problems have greatly motivated the research and development of clean energy. Up to date, increasing attention has been put into the renewable energy sources such as wind, solar, tidal, biomass and geothermal[5]. Nevertheless, these primary energy sources are intermittent and not stable in nature, which bring advanced energy storage system on request.

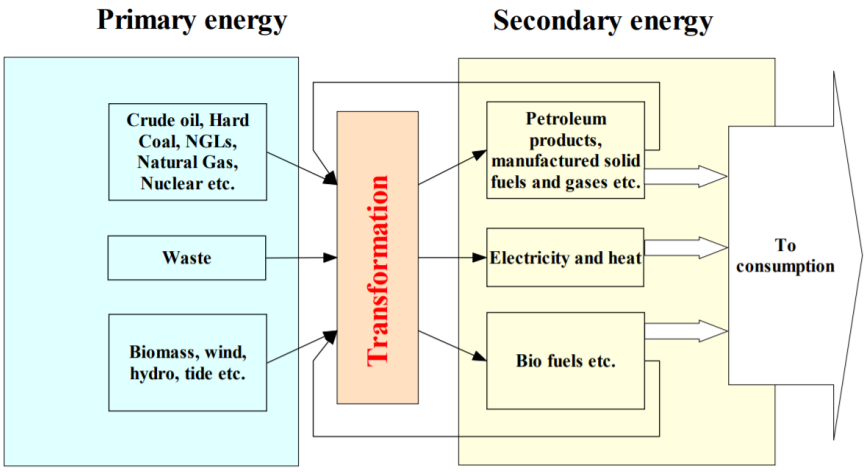

Figure 1.1 Primary and secondary energy[6]

Energy storage is an essential bridge between secondary energy and human consumers. On the one hand, energy storage serves as a "bank" of energy for some unsteady energy forms such as solar, wind and tidal energy to give a continuous stable supply. On the other hand, energy storage systems can gather and store the waste energy (e.g. the heat generated by thermal power generation) to increase the over-all energy efficiency. Various energy storage systems (ESS) possess different characteristics of power and energy density, lifetime, cycle efficiency, self-discharge rates, capital cost and scale, storage duration and technical maturity. These specific characteristics of ESS enable them to be applied in different applications.

1.1.1 Mechanical energy storage

Mechanical energy storage generally stores kinetic energy or potential energy, of which the former pattern is achieved by flywheels, while the latter pattern can be realized by compressed air energy storage and pumped hydro energy storage.

1.1.1.1 Flywheel energy storage (FES)

Flywheel energy storage system stores electrical energy in the form of rotational kinetic energy. As shown in Figure 1.2, FES is composed of composite flywheel linked with motor generator and magnetic bearing. The principle of this technology has been applied in experimental bus which was called "gyro-buses"[7]. As an energy storage device, FES have a discharge process to generate electrical energy and a charge process to regain the energy. During the charging phase, the electrical energy accelerated the motor which transferred the angular momentum to the rotor through a shaft. This rotor is the component that can store the kinetic energy. During the

discharging phase, the rotor transferred the angular momentum back to the generator through the same shaft and converted this kinetic energy to electrical energy.

FES model has many advantages such as low maintenance cost, long life cycle, high efficiency, free from depth of discharge effects, environmentally friendly, wide operating temperature and condition but the idling loses are the critical disadvantages which are caused by the external forces such as magnetic force or friction[8]. These good characteristics enable FES to be used in countless charge/discharge cycles and medium-term storage applications such as small-scale energy storage[9, 10], peak power buffer[10], wind diesel generator[11], photovoltaic system[12], harmonics[13], distribution network[14], UPS[15, 16], and high voltage stator[17].

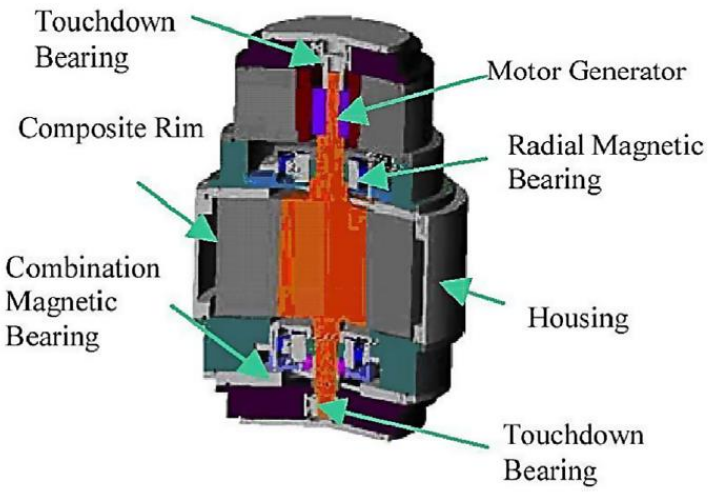

Figure 1.2 Flywheel device components[8]

1.1.1.2 Pumped hydro energy storage (PHES)

Pumped hydro energy storage stores electrical energy by pumping water uphill as gravity potential energy. As shown in Figure 1.3, the water is stored in upper reservoir and can be released to lower reservoir driving the generator located in powerplant chamber in order to produce

electricity power when needed. PHES is a quite mature and widely applied energy storage system around the world (Table 1). The first PHES system was constructed in Italy and Switzerland in 1890 and furtherly developed in the U.S. at the beginning of 1929. To date, PHES provide over 3% of global generation which is around 90 GW with the efficiency in the region of 70-85%.

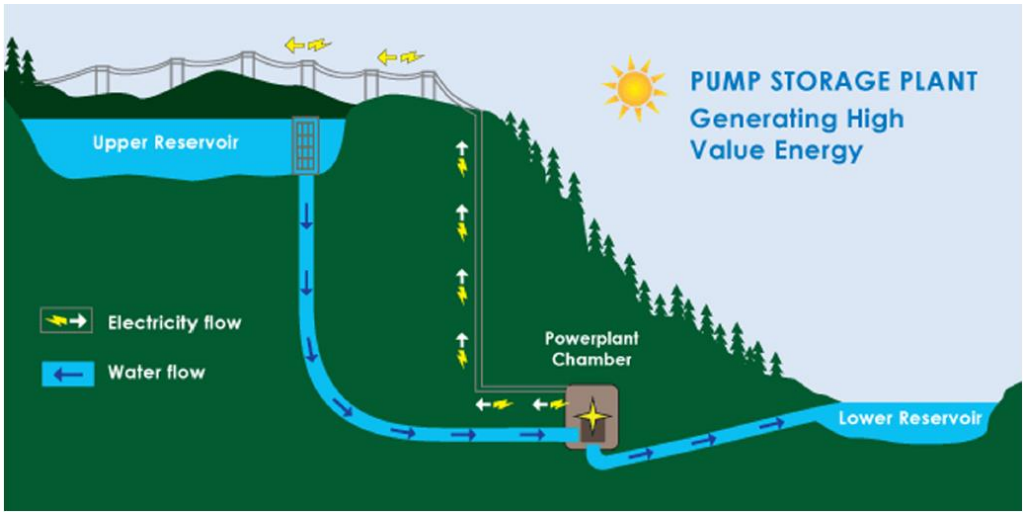

Figure 1.3 Pumped hydroelectric energy storage[4]

The advantage of PHES is clear to us: it has the largest storage capacity as compared to other energy storage systems. However, the disadvantages lie in several aspects: large capital cost, highly dependent on the local topography and direct environmental damage. Therefore, PHES only applied in the places where there is enough supply of water, adequate close land areas divided by adequate elevation.

Table 1.1 PHPS around the world[8]

Location	Plant name	Online date	Hydraulic head (m)	Max total rating (MW)	Hours of discharge	Plant cost
Australia	Tumut 3	1973	–	1690	–	–
China	Tianhuangping	2001	590	1800	–	$ 1080 M
	Guangzhu	2000	554	2400	–	–
French	Grand maison	1987	955	1800	–	–
Germany	Markersbach	1981	–	1050	–	–
	Goldisthal	2002	–	1060	–	$ 700 M
Iran	Siah Bisheh	1996	–	1140	–	–
Italy	Plastra edolo	1982	1260	1020	–	–
	Chiotas	1981	1070	1184	–	–
	Presenzano	1992	–	1000	–	–
	Lago delio	1971	–	1040	–	–
Japan	Imaichi	1991	524	1050	7.2	–
	Okuyoshino	1978	505	1240	–	–
	Kazunogowa	2001	714	1600	8.2	$ 3200 M
	Matanogawa	1999	489	1200	–	–
	Ohkawachi	1995	411	1280	6	–
	Okukiyotsu	1982	470	1040	–	–
	Okumino	1995	485	1036	–	–
	Okutataragi	1998	387	1240	–	–
	Shimogo	1991	387	1040	–	–
	Shin takesagawa	1981	229	1280	7	–
	Shin toyne	1973	203	1150	–	–
	Tamahara	1986	518	1200	13	–
Luxemborg	Vianden	1964	287	1096	–	–
Russia	Zagorsk	1994	539	1200	–	–
	Kaishador	1993	–	1600	–	–
	Dneister	1996	–	2268	–	–
South Africa	Drakensbergs	1983	473	1200	–	–
Taiwan	Minhu	1985	310	1008	–	$ 866 M
	Mingtan	1994	380	1620	–	$ 1338 M
UK/Wales	Dinorwig	1984	545	1890	5	$ 310 M
USA/CA	Castaic	1978	350	1566	10	–
USA/CA	Helms	1984	520	1212	–	$ 416 M
USA/MA	Nothrfield Mt	1973	240	1080	10	$ 685 M
USA/MI	Ludington	1973	110	1980	9	$ 327 M
USA/NY	Blenheim–gilboa	1973	340	1200	12	$ 212 M
USA/NY	Lewiston–Niagara	1961	–	2880	20	–
USA/SC	Bad creek	1991	370	1065	24	$ 652 M
USA/TN	Racoon Mt	1979	310	1900	21	$ 288 M
USA/VA	Bath county	1985	380	2700	11	$ 1650 M

1.1.1.3 Compressed air energy storage (CAES)

Compressed air energy storage system compresses the air using off peak electricity to store the potential energy in a reservoir either an underground cavern or aboveground pipes or vessels[18]. Then the air is released and heated followed to drive a turbine-generator to produce electricity power. It is noted that the off-peak base load electricity is cheaper than gas which is used to compress the air for CAES. The reservoir can be Hard rock cavern, salt cavern, depleted gas fields or an aquifer[8], among which hard rock cavern is 60% more expensive than salt cavern while aquifer cannot stand with high pressure air leading to a lower capacity. Hence, based on the application, people need to select adequate reservoir to meet specific parameters. The diagram of CAES is shown in Figure 1.4.

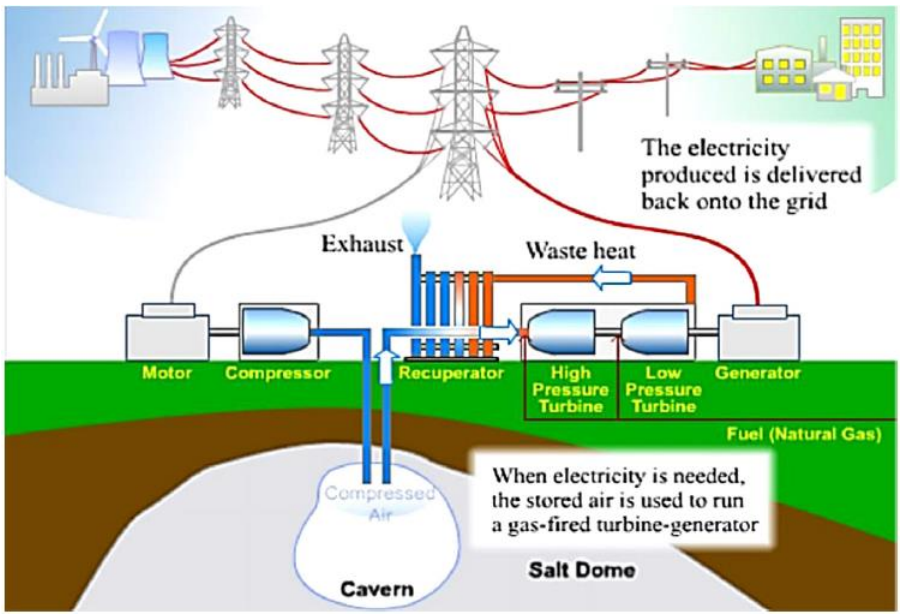

Figure 1.4 CAES plant schematic diagram[18].

The CAES principle was introduced in 1970s to provide load following and to meet the peak demand. After that the first plant of CAES came into being in Huntorf, Germany with a capacity of 290 mW to support a nuclear plant. Later in 1991, the second plant of CAES was built in Mcintosh, Alabama with a 110 mW capacity for 26h[19, 20]. Although CAES do have the advantages that it is able to produce electricity 3 times larger than a conventional gas turbine for a given amount of fuel[21], there is still a lot of risk in the development of CAES due to the complicate underground geology. Therefore, this technology is ideal for large bulk energy supply and demand but not suitable for small-scale energy storage such as vehicle and portable devices.

1.1.2 electrochemical energy storage

Electrochemical energy storage (EES) system is considered very promising for effective and efficient usage of clean energy and therefore has been intensively investigated during past decades.

1.1.2.1 Battery energy storage

The most common battery energy storage systems are shown in Figure 1.5[22]. Lead-acid battery with low cost and a relatively stable charge and discharge state is one of the oldest type of rechargeable battery, which was invented in 1859 by French physicist Gaston Plante. However, its large volume and high weight make it hard for the application in light and portable electric devices[23]. Nickel-Cadmium battery may be an option for portable electronic devices, but its severe memory effects lead to short life cycle and the toxicity of cadmium is not environment friendly[24]. In the late 1990s, early nickel-metal hydride (Ni/MH) batteries was invented by Singh et al.[25] and Rantik[26]. Comparing with lead-acid and nickel-cadmium system, Ni/MH has relatively high

energy density, high-rate capability, less prone to memory and lack of poisonous heavy metals; however the leakage problem inevitably limits specific capacity and life cycle[27].

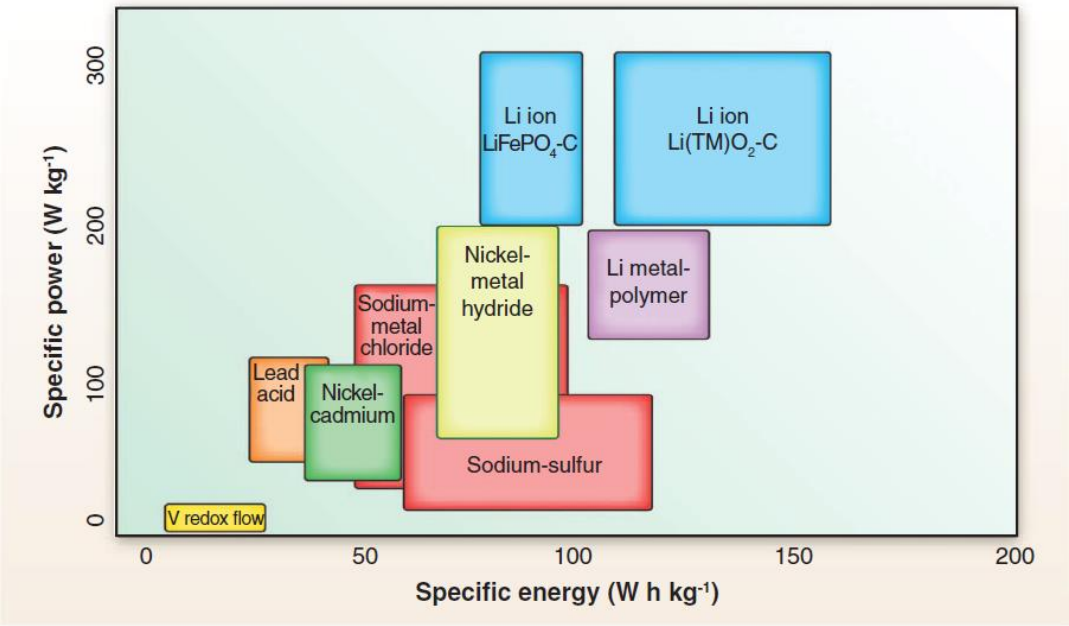

Figure 1.5 Gravimetric power and energy densities for different rechargeable batteries. Most of these systems are currently being investigated for grid storage applications.

Lithium ion batteries have readily become the most ubiquitous energy storage system. They are commonly used in portable electronic devices, because they have long cycle life, high energy and power density, do not suffer from memory effects[28], and have relatively lower energy required for production[5] (Figure 1.6). Such overwhelming advantage of lithium based system lies in lithium's low molecular weight, which provides high gravimetric energy density; small ionic radius, which is beneficial for diffusion; and low redox potential [E°(Li+/Li) =-3.04 V vs standard hydrogen electrode (SHE)] [29], which enables high-output voltages and thus high energy density[22].

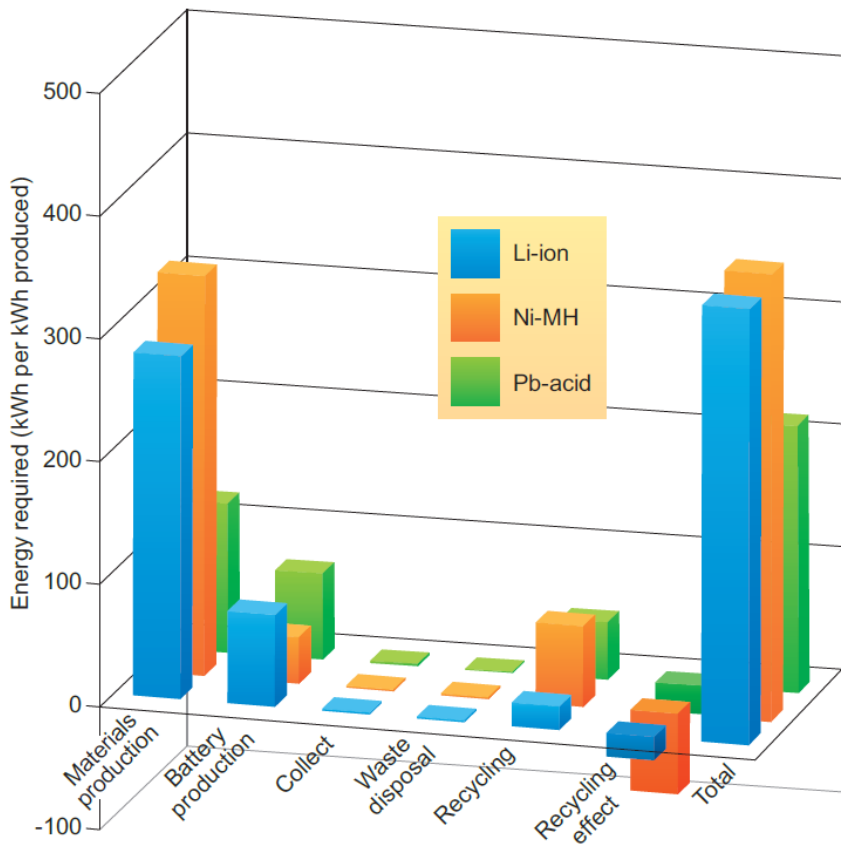

Figure 1.6 Energy required for the production of a 1 kWh electrochemical storage system. Data are from refs 6–9 and compare the energy cost for Li-ion, Ni–MH (nickel–metal hydride) and Pb–acid technologies. Materials production is clearly the main contributor to the energy cost of producing an electrochemical storage system.

In addition to the excellent electrochemical properties, production cost is another important factor. As shown in Figure 1.7, the energy cost for the lithium ion battery is lower than previous generation of batteries for portable electronic devices, Ni-MH batteries and its energy cost is only two times of commonly used lead acid batteries that can only be applied in large scale equipment. Moreover, lithium abundance on earth's crust (fraction of earth's crust is 1.8E-5) is much higher than other active materials such as mercury (fraction of earth's crust is 8E-8), Cadmium (fraction of earth's crust is 1.60E-7) and Pb (fraction of earth's crust is 1.3E-5) (Figure 3). In terms of

absolute quantities, the amount of Li available on the Earth's crust is sufficient to power a global fleet of automobiles[30].

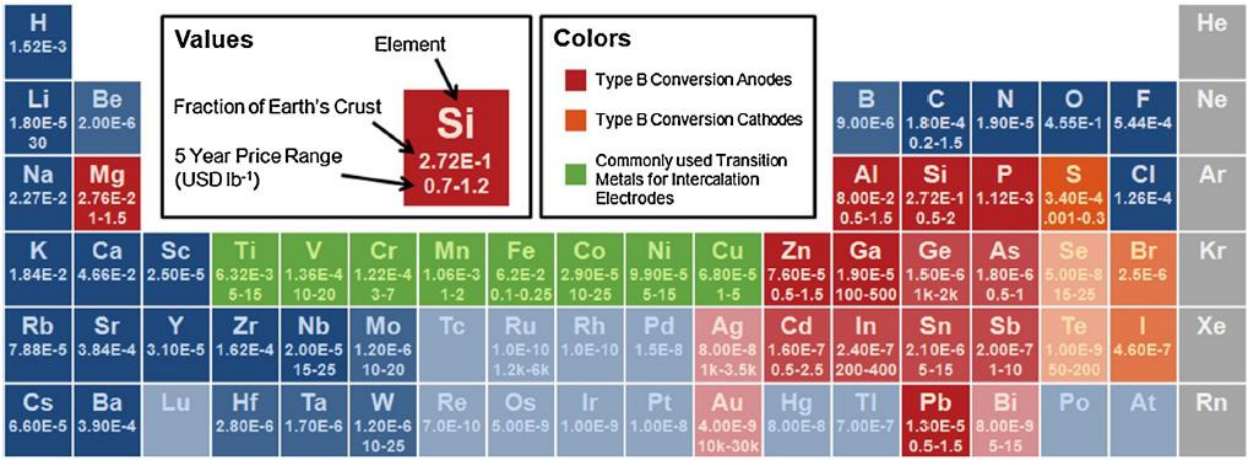

Figure 1.7 Availability of elements that may host Li as electrodes. Elements with abundance (as fraction of Earth's crust) below 10-5 are slightly faded, and elements below 10-7 are faded further. Prices are approximate 5-year ranges of metal prices (except Ge, which is a 3 year range)[31], 80–100 mesh natural graphite for carbon[32], and the Vancouver/USGS prices for sulfur[33].

1.1.2.2 Super capacitor energy storage

A supercapacitor generally is composed of two metal-foil electrodes, separator which is made of ceramic, glass or plastic film, and electrolyte (Figure 1.8). Supercapacitors store energy through the electric field of the electrochemical double layer produced by opposite charges when a voltage is applied.

Compared with batteries, supercapacitors can be charged substantially faster, provide higher power density and have longer cycle number up to 100,000 times. Moreover, supercapacitor exhibits high efficiency over 95% due to low resistance, resulting in reduced loss of energy and

rapider transport rate of ions[34]. Nevertheless, they have low energy density and high self-discharge rate due to the limited surface area of elecctrodes[35].

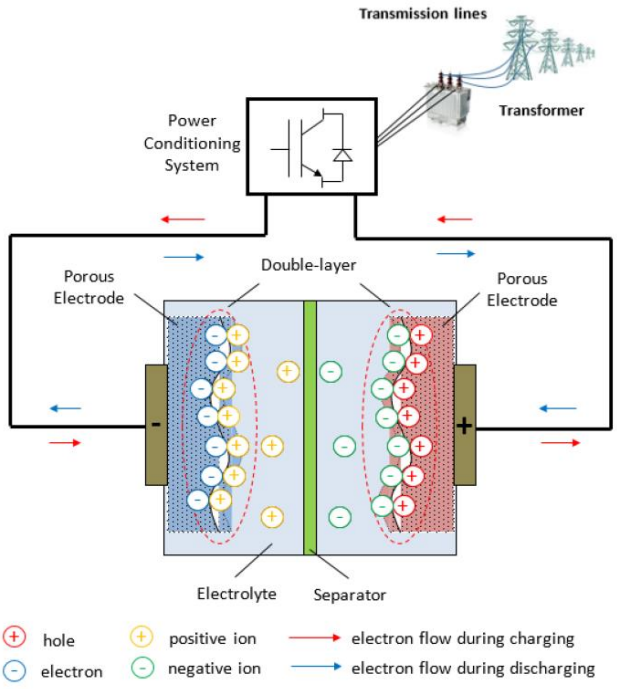

Figure 1.8 Schematic diagram of electrochemical double-layer capacitors[36]

Considering the advantages and disadvantage of supercapacitors, they are applied in starting engines, actuators, and electric vehicles (EV) or hybrid-electric vehicles (HEV) for transient load leveling. It is noted that supercapacitor provide great improvement in vehicle fuel efficiency under stop-and-go driving conditions when they are used for regenerative breaking.

1.1.2.3 Superconducting magnetic energy storage (SMES)

The principle of superconducting magnetic energy storage was first introduced in 1970s to improve the load of French electricity network[37]. It stores the energy through the magnetic field which has been cooled to a temperature below its superconducting critical temperature. The schematic of SMES is shown in Figure 1.9. The stored energy is proportional to the wire inductance and the square of direct current. This energy can be regained through a discharging process when the network demands the excess power[38].

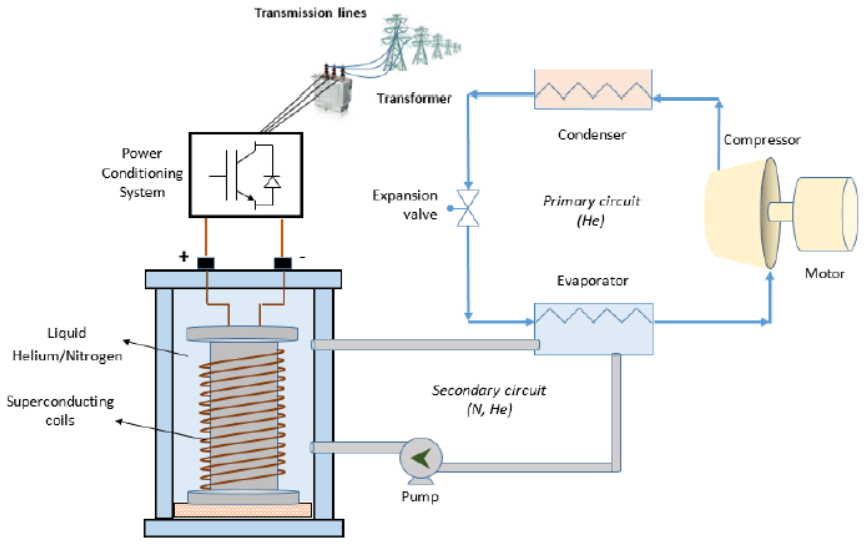

Figure 1.9 Schematic of superconducting magnetic energy storage systems[36]

There are two major advantages of SMES: the first one is the high efficiency up to 98%, due to the nearly zero resistance of superconducting coils under critical temperature[39]; the other one is that SMES can be cycled almost infinitely and are capable if discharging the near totality of the stored energy[40]. However, the drawbacks of SMES, such as extremely expensive cost ($1000-10,000/kW) and self-discharge issues, inevitably prevent it to fill a unique niche in the market.

Hence, SMES only applied in short term energy such as uninterruptible power supply (UPS), pulse power source for dedicated applications and flexible AC transmission[41].

1.1.3 Chemical energy storage (CES)

Chemical energy storage converts or stores electric energy in a form of chemical energy. During the charge phase, the electric energy is used to produce chemical compound which can be stored; while during the discharge phase, the chemical energy converts to electricity power through an electrochemical reaction. The chemical compounds which serve as energy storage mediums generally have high energy density, e.g. hydrogen, methane, hydrocarbons, methanol, butanol and ethanol. Among these chemical compounds, hydrogen is the most promising chemical for CES system. Hydrogen is the only carbon-free fuel and has the highest energy density compared to any known fuels which only have water as the product when applied in CES.

The hydrogen storage system is composed of three parts: electrolyzer unit, the storage component and an energy conversion[42]. To date, the commonly used electrolyzer technologies are alkaline (A), proton exchange membrane (PEM) and solid oxide (SO) electrolysis cells, while the fuel cell parts mainly used alkaline (AFC), proton exchange membrane (PEMFC), solid oxide (SOFC), phosphoric acid (PAFC) and molten carbonate (MCFC)[43].

The advantages of hydrogen storage system are the abilities to convert chemical energy to electricity without involving any intermediate energy-intensive steps and noisy moving parts, and it is also environmentally friendly. However, there is still lack of a effective and safe storage of hydron gas on large scale. Moreover, the low volumetric capacity and extremely high operating temperatures make this technology hard to be used in transport applications.

1.1.4 Thermal energy storage (TES)

Thermal energy storage is one of the most widely used energy storage systems. TES devices generally transfer and store electricity or other waste heat resources in the form of thermal energy. There are three main thermal energy storage systems: sensible heat storage, latent heat storage and thermochemical heat storage.

Sensible heat storage uses materials that do not undergo any phase change within the working temperature range. Concrete, cast ceramics and molten salts are often used as energy storage medium in this technology. The major drawback of sensible heat storage is the energy loss caused by the high freezing point (around 100 ℃). Latent heat storage systems store latent heat which generates as a result of phase change. The phase change temperature of certain materials for latent heat storage should match the thermal input source[38]. These materials often have a higher capacity of thermal energy compared with that of sensible heat storage due to the high latent heat associated with the phase change. Thermochemical heat storage involves a reversible reaction where the thermal energy is stored under the endothermic reaction step and released under exothermic reaction step (Figure 1.10). Several TES materials have studied for this technology, such as metallic hydrides (MgH_2 and CaH_2), carbonates ($PbCO_3$ and $CaCO_3$), hydroxides ($Mg(OH)_2$ and $Ca(OH)_2$), oxide (BaO_2 and Co_3O_4), ammonia system (NH_4HSO_4 and NH_3), and organic systems (CH_4/H_2O, CH_4/CO_2, C_6H_{12})[4].

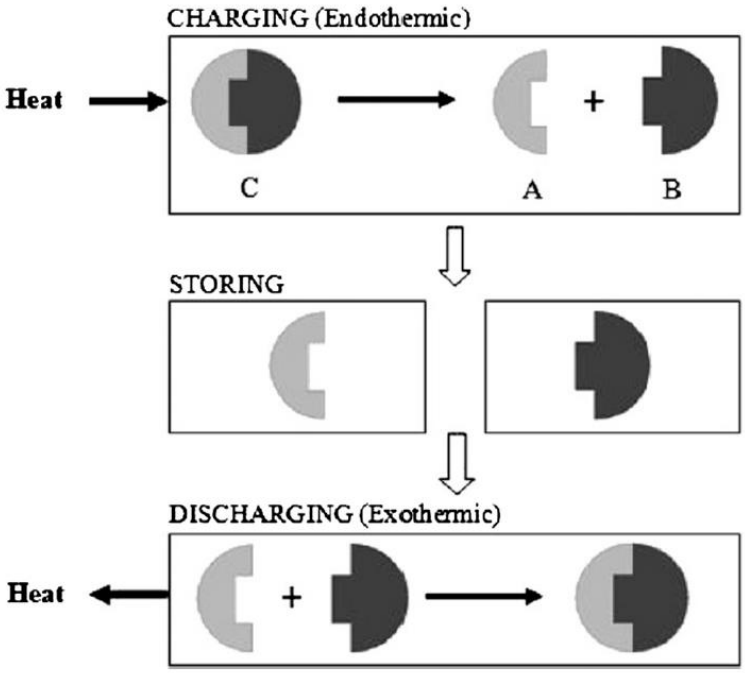

Figure 1.10 Process of thermochemical heat storage[38]

TES systems usually are classified into high-temperature systems and low-temperature systems based on the working temperature of the materials. High-temperature TES systems which operates over 200℃ are usually used in renewable energy technologies, waste heat recovery and thermal power systems. On the other hand, Low-temperature TES systems often used in building heating and cooling applications, solar water boiler and air heating system.

1.2 Carbon materials applied in energy storage

Carbon materials have been used and developed by human for over thousand years. From the beginning of such long history, carbon materials have been closely bound with energy pushing the human civilization to today's prosperity.

Humans started to use carbon to directly provide energy since we leant drilling wood to make fire, which only converts 15% of wood's energy to heat. In the 1880s, coal was used to generate electricity which exhibit around 37% energy efficiency. After 1950s, with the development of nanotechnologies, the advent of new forms of nanocarbon, particularly, graphite intercalation compounds, carbon nanotubes and graphene push the electrochemical energy storage to a new level. Supercapacitors using carbon-based materials as electrodes generally exhibit an efficiency of ~95%[4], while lithium-ion batteries using graphite as anode materials possess even higher energy efficiency around 97.5%[44]. As we can see, with the development of carbon materials, the energy efficiency of carbon-based energy storage systems significantly increased.

The extensive applications of carbon materials in energy storage contribute to the carbon atom structure and crystalline structure. The carbon atom with a ground state electronic configuration $(1s^2)(2s^2p_x2p_y)$ can form sp^3, sp^2 and sp^1 hybrid bond as a result of promotion and hybridization[45]. Most commonly used carbon materials such as graphite, graphite intercalation compounds, carbon nanotubes (CNTs) and graphene share the same basic unit structure of an extended hexagonal array of carbon atoms with sp^2 σ bonding and delocalized π bonding. The electrons shared in the delocalized π bonding contribute to the extremely high electrical conductivity (graphite~10^5 S/m, graphene~$2*10^5$ S/m). High surface area also improves the electrochemical activity of the overall energy storage systems. Good designability is another important characteristic that enables various

structure of carbon materials from 0-dimissional graphene quantum dots to 4-dimissional self-healing graphene, providing numerous possibilities of the application in different energy storage systems. In this section, we mainly introduced the development of four typical carbon materials for energy storage. They include: graphite, graphite intercalation compound, carbon nanotube, and graphene (Figure 1.11).

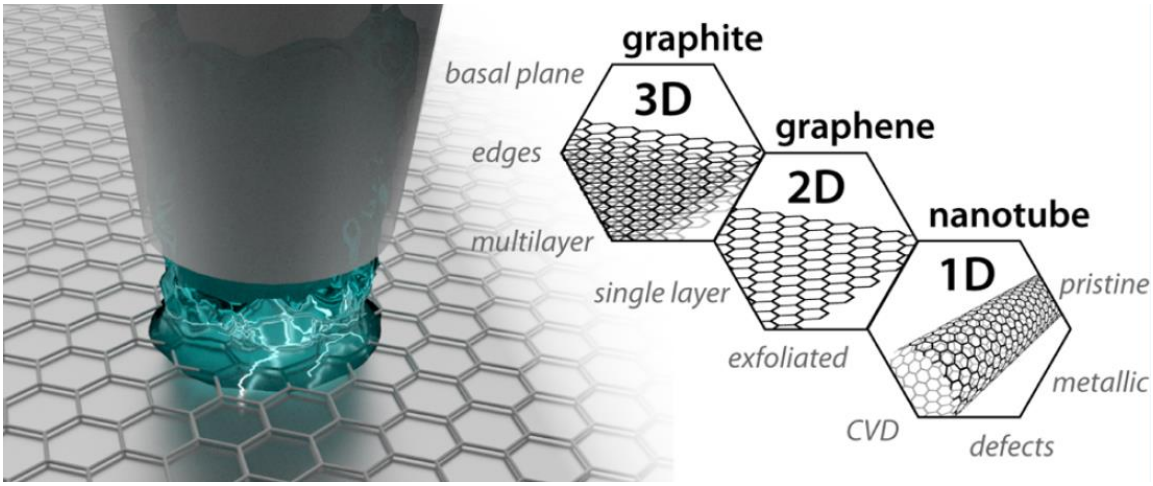

Figure 1.11 Schematic of typical carbon materials used for energy storage[46]

1.2.1 development of carbon materials

Carbon materials have a long developing history of human beings, but it is after the breakthrough of nanotechnology that nanocarbon materials experienced a rapid development in the last 50 years (Figure 1.12). This 50 years' history of research started with graphite, a material found in nature. Graphite is a layered quasi-2D material which is stacked by graphene layers in the AB Bernal configuration. In 1960, the electronic structure of graphite was revealed by McClure for the first time[47]. Then in 1982, Rajeeva R. Agarwal and J. Robert Selman found that lithium ion can have a reversible electrochemical intercalation with graphite[48]. After that, lithium ion battery

started to use graphite as anode materials instead of lithium metal, and thus significantly improve the safety of lithium-ion batteries.

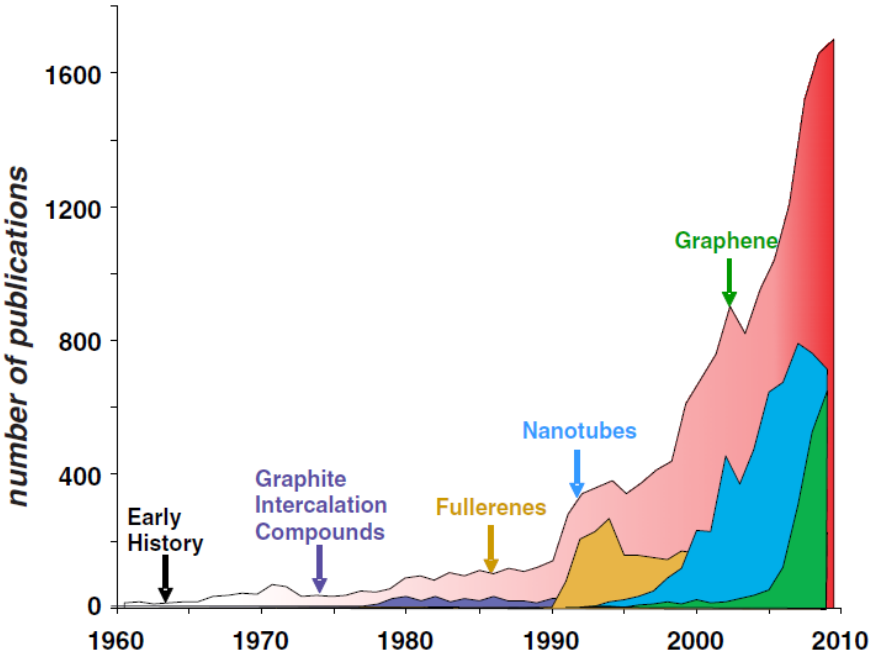

Figure 1.12 The number of annual publications on sp2 carbon materials in the last 50 years[49]

Although graphene was first isolated in 2004 by Novoselov et al[50], scientist attempted to study the single layer of graphene in the early 1970s. However, at that time, it is hard to isolate single layer graphene and conduct an effective characterization of single layer graphene. Instead, they embedded singe layers of graphene into a host material called graphite intercalation compound (GIC). This graphite intercalation compound allowed independent study of the graphene layer and intercalant layer[51]. For example, the intercalation process of Li metal is shown in Figure 1.13

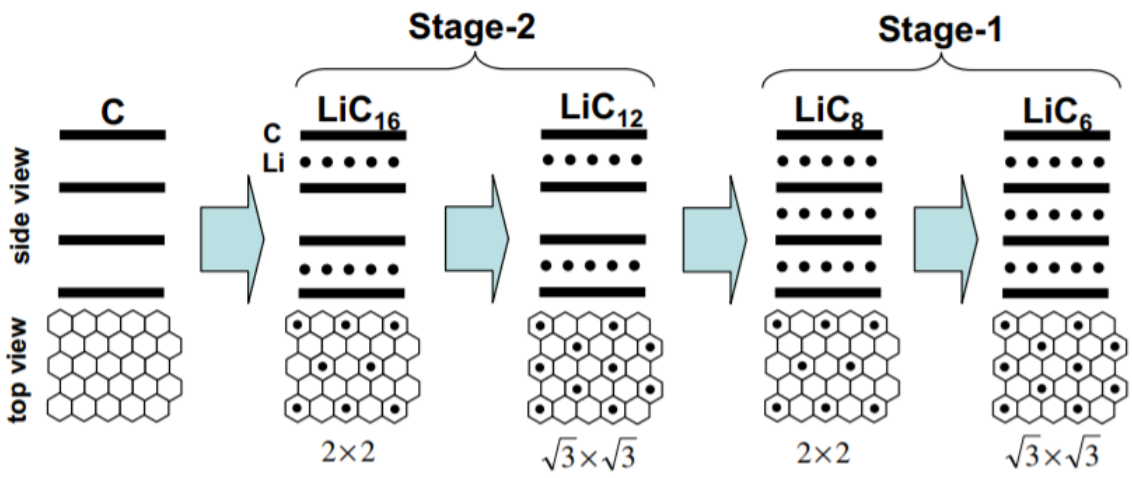

Figure 1.13 Li intercalation process to graphite[51]

In 1993, Iijima and Bethune first synthesized the single-wall carbon nanotube (SWNT)[52]. SWNT is considered a rolled graphene sheet as shown in Figure 1.14. Depending on the geometry of CNTs, they can exhibit metallic or semiconducting properties. CNTs and CNT-based composites are widely used in energy storage systems, such as supercapacitor[53-55], batteries[56-58] and fuel cells[59-61].

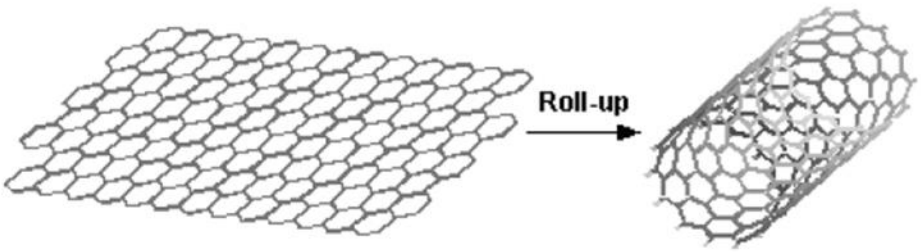

Figure 1.14 A monolayer graphene sheet rolled up to form an SWNT[49].

In the first decade of 21st century, single-layer graphene was first isolated in 2004[50], pushing the passion of studying carbon materials to a new level. Graphene is a defect-free carbon monolayer packed into a 2D honeycomb lattice. It is the first 2-D atomic crystal which has high electron conductivity (2000 S cm^{-1}) [1] and thermal conductivity (5000 W/mK)[62], ultrahigh surface area (2630 m^2 g^{-1}) [2], high carrier mobility at room temperature (~10000 cm^2 V^{-1} s^{-1})[50], and excellent mechanical stiffness, strength and elasticity (Young's modulus of 1 TPa and intrinsic strength of 130 GPa)[63] (Figure 1.15). These excellent properties of graphene lead to wide applications in different fields such as energy storage[64-66], polymer composites[67, 68] and photoelectric devices[69, 70]

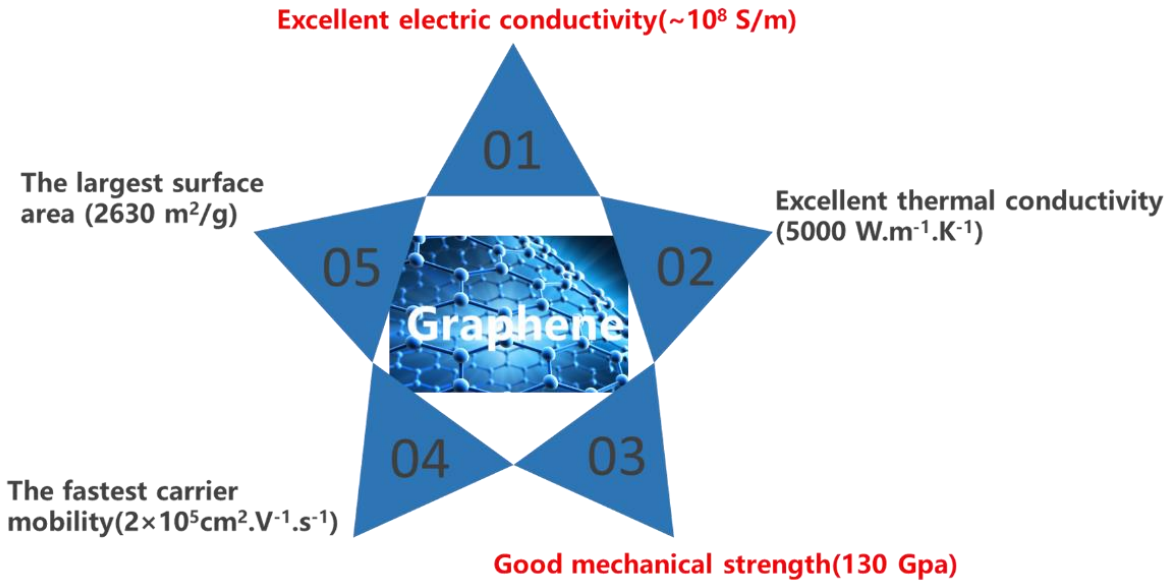

Figure 1.15 The physical properties of graphene

1.2.2 Graphite

Graphite has a layered structure which is stacked by an extended hexagonal array of carbon atoms with sp^2 σ bonding and delocalized π bonding in the sequence of ABABA. As shown in

Figure 1.16, this structure results in a hexagonal unit cell with dimension c=6.71 Å and a=2.46 Å[71]. The interlayer spacing of graphite is 3.35 Å, which is a large difference compared with in-plane C-C distance 1.42 Å. This fact suggests that the contribution to the interlayer bonding from π bond overlap is negligible[45]. Therefore, most researchers consider the interlayer potentials belong to the Van del Waals type. However, some evidence from scanning probe microscopical images of the graphite surface indicates that there may be some π orbital interaction between planes[72].

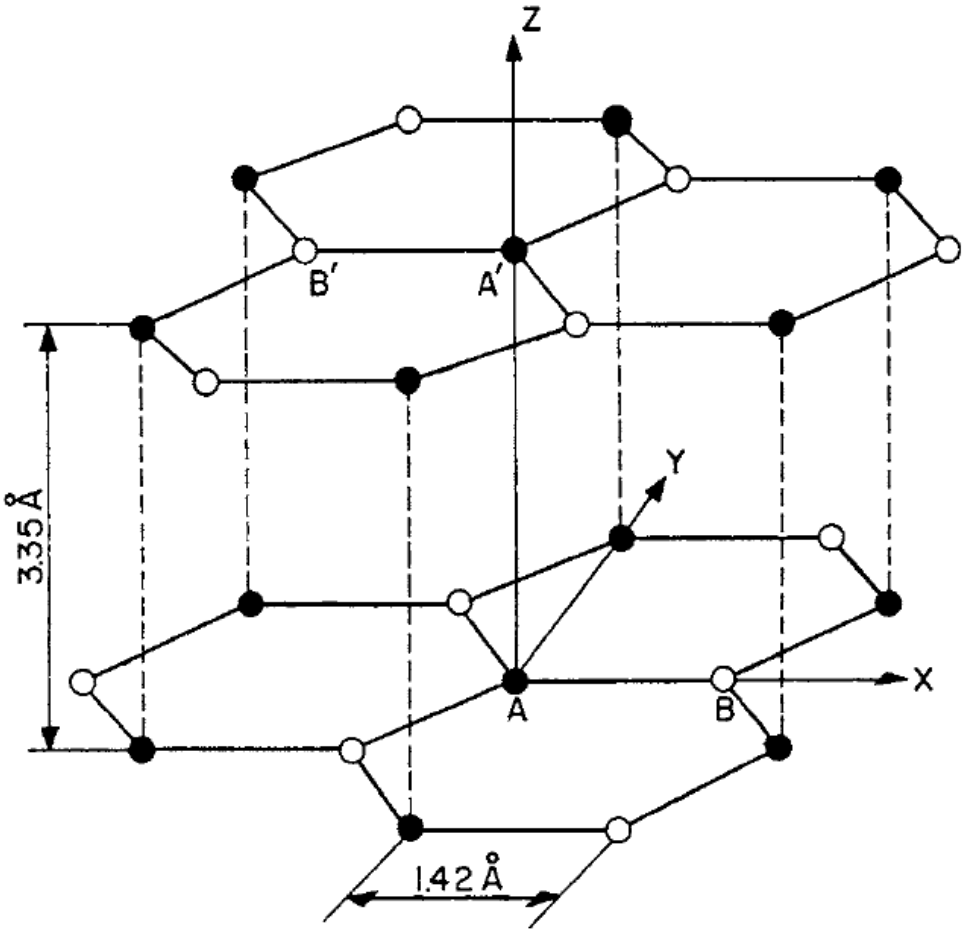

Figure 1.16 The crystal structure of graphite. The primitive unit cell is hexagonal, with dimensions a =2.46 Å and c=6.71 Å. The in-plane bond length is 1.42 A°. There are four atoms per unit cell, namely A, A', B and B'. The atoms A and A', shown with full circles, have neighbors directly

above and below in adjacent layer planes; the atoms B and B', shown with open circles, have neighbors directly above and below in layer planes 6.71 Å away.[73]

Graphite has a good electrical and thermal conductivity within the layers and a poor electrical and thermal conductivity perpendicular to the layers due to the anisotropy. The electrical conductivity (σ_a, σ_c), mobilities (μ_a, μ_c), relation times (τ_a, τ_c), mean free paths (l_a, l_c) and electron density (n) at various temperature for pyrolytic graphite are shown in table 1.2.[74] The subscript a and c are the direction that paralleled to the in-plane of graphite and perpendicular to the in-plane of graphite, respectively.

Table 1.2 Electrical properties of graphite[74]

Parameters	Unit	300K	77.5K	4.2K
σ_a	10^4 S cm^{-1}	2.26	3.87	33.2
σ_c	S cm^{-1}	5.9	3.3	3.8
σ_a/σ_c	10^4	0.38	1.2	8.8
μ_a	10^4 cm^2/V s	1.24	5.75	7.0
μ_c	cm^2/V s	3.3	5.0	8.0
τ_a	10^{-13} s	3.5	16.2	196
τ_c	10^{-14} s	0.95	1.6	2.7
l_a	10^3 Å	0.7	3.2	39
lc	Å	0.95	1.6	2.7
n	10^{18} cm^{-3}	11.3	4.2	3.0

This high electrical conductivity and typical layered structure of graphite contribute to a wide application in energy storage. Since Rajeeva R. Agarwal and J. Robert Selman first applied graphite as anode materials in lithium-ion batteries in 1986[48], graphite anode have been deeply studied and finally was commercialized. R. Yazami and Ph. Touzain used an electrochemical method to synthesize lithium intercalation compounds for lithium-ion batteries[75]. They proved that the polyethylene oxide with lithium perchlorate was an effective polymer electrolyte to achieve the electrochemical intercalation of lithium into graphite. The capacity for the first time achieved 340 Ah/kg. Later, researchers started to use graphite with functional groups as anode materials for LIBs. Thierry Cassagneau and Janos H. Fendler prepared nanometer-thick polyelectrolytes and graphite/graphite oxide nanoplatelets on a conducting substrate through a self-assembly method. The electrode exhibited high density of 1232 mA h g^{-1}[76]. Although graphite has good electrical conductivity, the specific capacity and energy density of graphite anode is limited. Researchers started to combine other active materials with high specific capacity with graphite, trying to develop electrode materials with high energy and power density. Graphite intercalation compounds are one of the most popular graphite composites materials that we would like to talk in the next section.

1.2.3 Graphite intercalation compounds

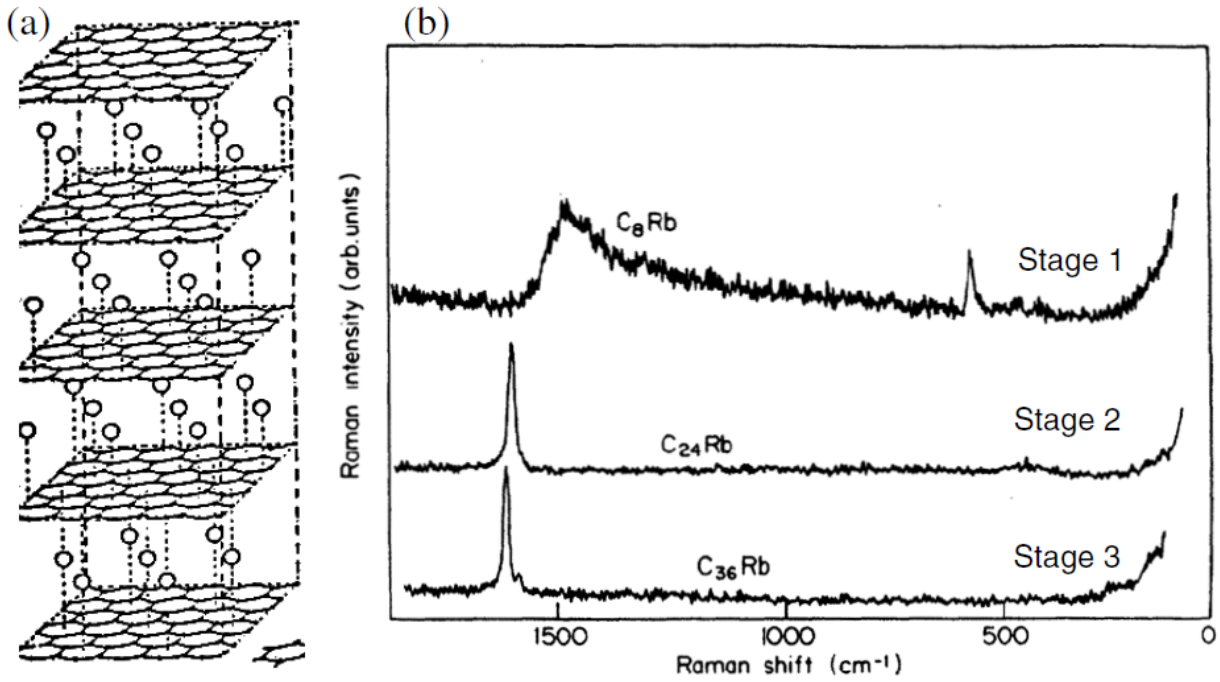

Figure 1.17 a The structure of a stage 1 graphite intercalation compound, showing an intercalate layer sandwiched between single graphene layers.[51] **b** The Raman spectra of stage 1, 2 and 3 rubidium intercalated graphite, in which a single layer of rubidium is intercalated between one, two and three graphene layers, respectively.[77]

As shown in Figure 1.17a, we can see the intercalant was intercalated into every single layer of graphene to form a stage 1 graphite intercalation compound. On the one hand, some guest intercalant species such as alkali metal donates electrons to graphene layers forming a donor graphite intercalation compound. On the other hand, intercalants such as ferric chloride accepts electrons from graphene layer forming an acceptor graphite intercalation compound in which graphene layers turn to be positive charged. These graphite intercalation compound exhibit different optical, transport, thermal, vibrational and spectroscopic properties with pristine graphene[49]. As shown in Figure 1.17b, stage 1 C_8Rb possessed a broader d peak at 1400 and more cm^{-1} extensive Rb peak at ~580 cm^{-1}, indicating a larger graphite interlayer spacing and larger

amount of Rb which was intercalated into graphene interlayers. Because for the stage 1 compound, every single layer of graphene was sandwiched by intercalant, while every two layers of graphene was sandwiched by intercalant for the stage 2 compound. Later, electrodes of different GICs have been applied in primary and secondary batteries. The high electrical conductivity and ion diffusion rate of GIC contributed to a better performance than pristine graphite. Moreover, alkali metal-GICs can store large amount of hydrogen due to the functional space in alkali metal, thus making it a competitive candidate of hydrogen storage materials. After 2010s, GICs were used to prepare graphene sheets through liquid phase exfoliation methods.

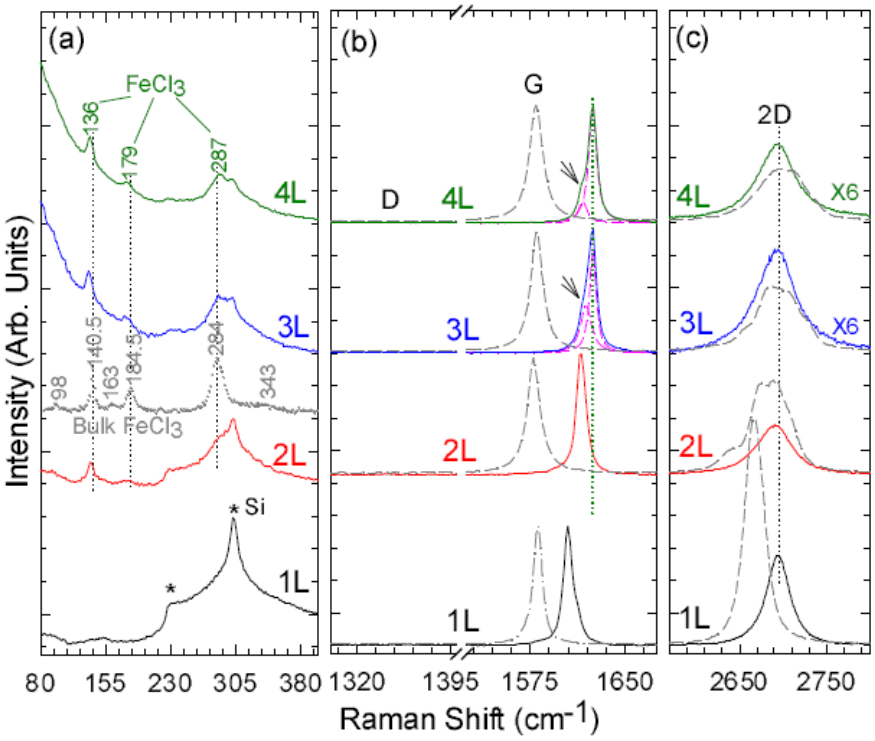

Figure 1.18 Raman spectra of pristine (dashed lines) and doped/intercalated (solid lines) 1-4L flakes, measured for 532nm excitation. (a) Low frequency region. (b) D- and G-region. (c) 2D-region. In (a) we also report the Raman spectrum of bulk FeCl3 (dotted gray line) for comparison. Vertical dotted lines are guides to the eye.[78]

Ferric chloride is reported to successfully insert into graphite flakes which proved by Raman scattering[78]. Figure 1.18 shows the Raman spectra of $FeCl_3$ intercalated 1 to 4 layers (L) graphene flakes compared to bulk $FeCl_3$. Clearly, typical 3 Raman modes from $FeCl_3$ are observed in 2-4L $FeCl_3$ intercalated graphene flakes, indicating that each graphene layer behaves as a decoupled heavily intercalated monolayer. These 3 $FeCl_3$ modes upshift ~3 cm^{-1} because Cl atoms simultaneously occupy preferred sites associated with the graphene lattice, which results in the loss of the Cl atoms long-range two dimensional order, since their in-plane structure is incommensurate with the graphene host lattice[79]. The 2D line shape for 2-4 L $FeCl_3$ intercalated graphene changed from multiple peaks to a single Lorentzian, which indicated the single layer graphene between two intercalant layers. Moreover, the G peak of $FeCl_3$ intercalated single layer (1L) graphene in Raman spectrum is ~1627 cm^{-1} which is higher than intercalated 2 and 3 L ~1623 cm^{-1} and 1625 cm^{-1}, indicating the doping on both top and bottom surfaces of single layer graphene (Figure 19 a). Based on this evidence, the author provides schematic diagrams of $FeCl_3$ intercalated 1-3L flakes.

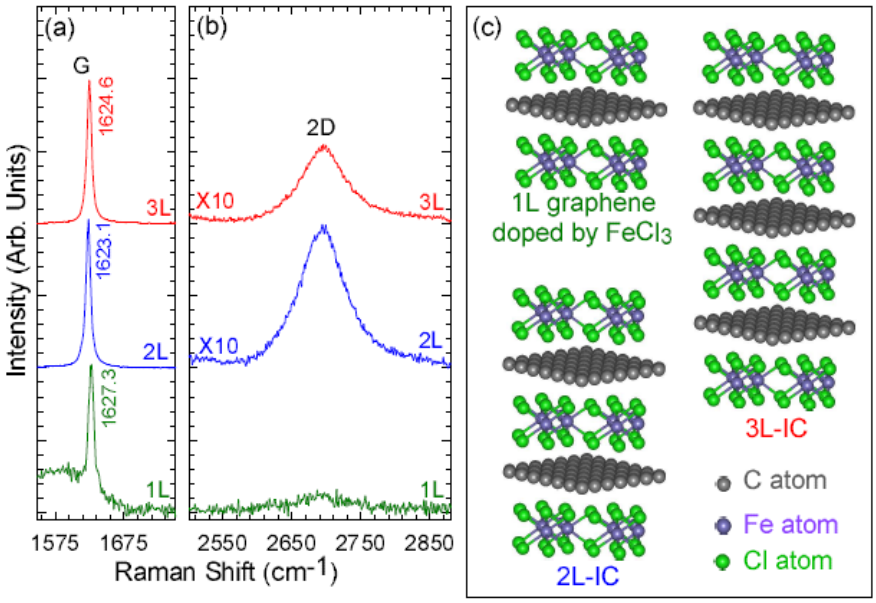

Figure 1.19 (a) G and (b) 2D band of Stage-1 flakes with 2/3L, and doped SLG, measured at 532nm for samples kept in the sealed quartz tube used for intercalation/doping. (c) Schematic diagrams of FeCl3 doped/intercalated 1-3L flakes[78].

Nickel chloride also has the potential to be a good intercalant for graphene due to the similar chemical properties between nickel and iron elements. Several researchers has demonstrated the possibility to insert nickel chloride into graphene interlayers[80 81 82]. The point is that graphene with nickel-based intercalants composite can serve as a precursor to synthesis nickel-rich NMC graphene composite. Copper chloride and palladium chloride can also intercalate into graphene interlayers, but the high cost of these raw materials is unsuitable for mass production and they cannot catalyze the bubbling exfoliation reaction between H_2O_2 and TM chloride intercalated graphite composite.

1.2.4 Carbon nanotube (CNT)

Carbon nanotube was first successfully synthesized by Iijima et al. in 1991[83]. It possesses high elastic modulus up to 1 TPa with high strength 10-100 times higher than the strongest steel under a same fraction of the weight. In additional to the excellent mechanical properties, CNT also shows good electrical ($4*10^4$ S m^{-1}) [84] and thermal conductivity (3500 W $m^{-1}K^{-1}$ [85]). It can be also stable over 2800℃ in vacuum. These outstanding physical and chemical property make CNTs (or perhaps CNT based composites) one of the most competitive materials for the applications of mechanical energy storage systems[86-88], supercapacitor[53, 89-91], lithium-ion batteries[56-58, 92] and thermal energy systems[93-95].

There are two kinds of carbon nanotube: single-walled carbon nanotubes (SWCNTs) and multi-walled carbon nanotubes (MWCNTs) which are composed of concentric SWCNTs[96]. CNTs

generally can be visualized as a sheet of graphene that has been rolled into a tube. To better understand the atomic structure of CNTs, we used vectors to describe the tube chirality or helicity. As shown in Figure 1.20, the chiral vector $\vec{C}_h$ which indicate the roll-up behavior is described by the equation:

$$\vec{C}_h = n\vec{a}_1 + m\vec{a}_2$$

and the integer (n, m) are the number of steps along the zig-zag carbon bonds of the hexagonal lattice and $\vec{a}_1$ and $\vec{a}_2$ are unit of vectors[96]. There are two limiting cases referring to as zig-zag (0°) and armchair (30°) based on the geometry of the carbon bonds around the circumference of the CNTs (Figure 21).

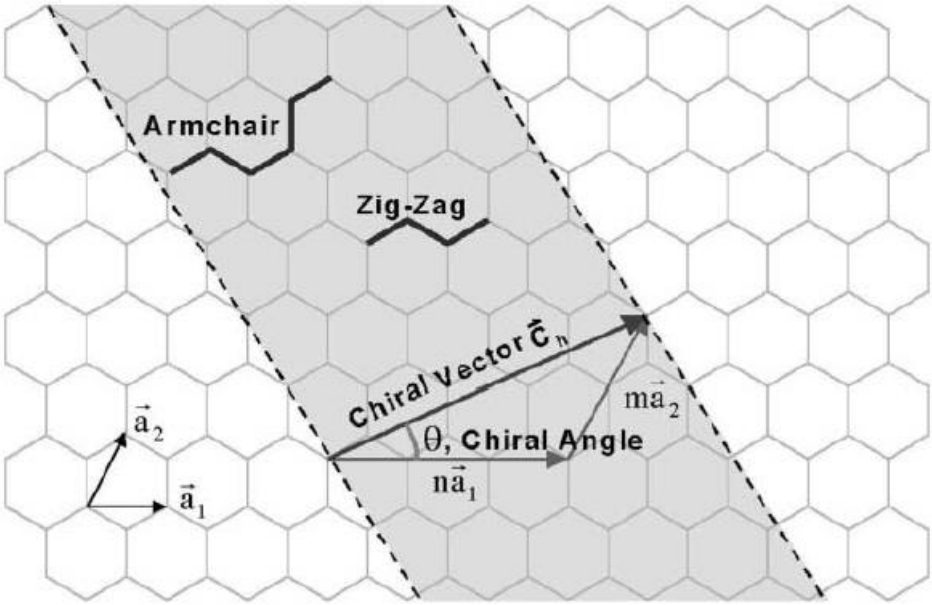

Figure 1.20 Schematic diagram showing how a hexagonal sheet of graphite is 'rolled' to form a carbon nanotube[96].

If we fold and roll the graphene sheet into a carbon nanotube, the assembled CNTs are shown in Figure 1.21. According to the different chiral vector, the zigzag nanotube has a chiral vector of (n, 0), while the armchair nanotube has a chiral vector of (n, n).

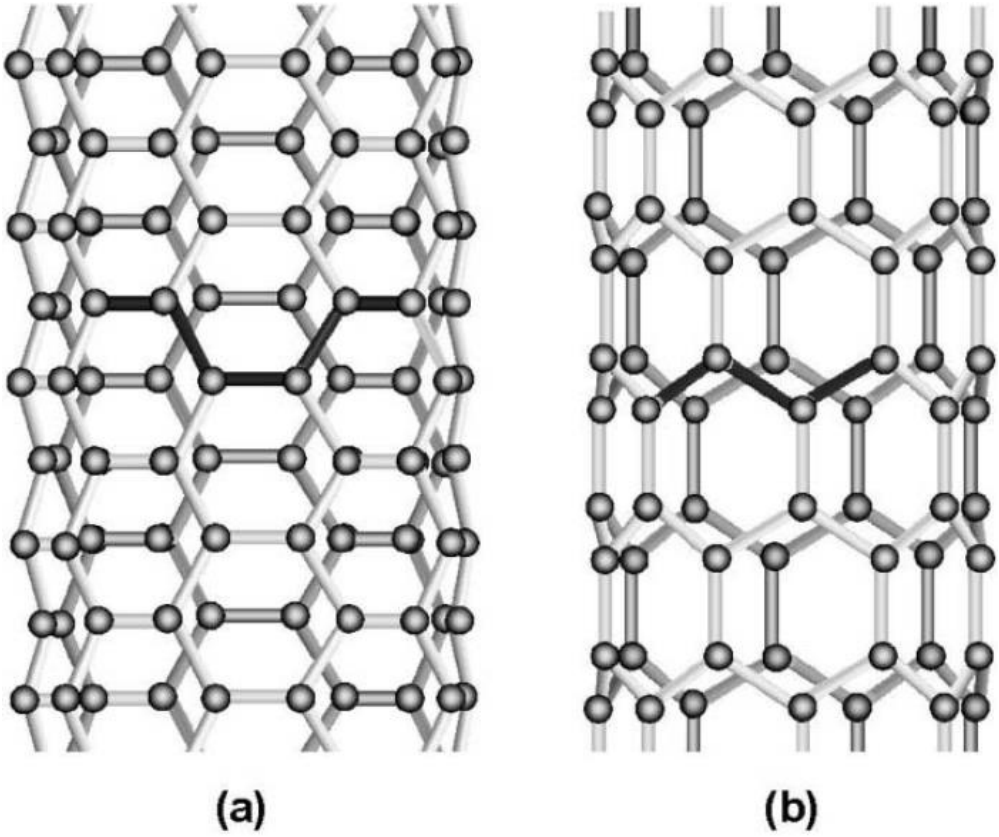

Figure 1.21 Illustrations of the atomic structure of (a) an armchair and (b) a zigzag nanotube.

The reason why people want to study the atomic structure of CNTs and classify them is that the chirality of CNTs has significant impact on physical and chemical properties. It is reported that although the CNTs can be either metallic or semiconducting which is decided by the tube chirality[97].

There are mainly three production methods of CNTs: arc-discharge, laser ablation, and chemical vapor deposition (CVD). Based on the applications of CNTs, a large amount of CNTs is

needed to be directly used as active materials or to make CNTs based composite materials. Among these three production methods of CNTs, CVD can produce the CNTs with the least amount of impurities and more amenable to large-scale production. Actually, many companies around the world have already achieved the commercialization of CNTs. ENN which is one of the biggest energy company in China have developed large scale CVD production line and sells the CNTs product as an effective conductive additives for Lithium-ion batteries.

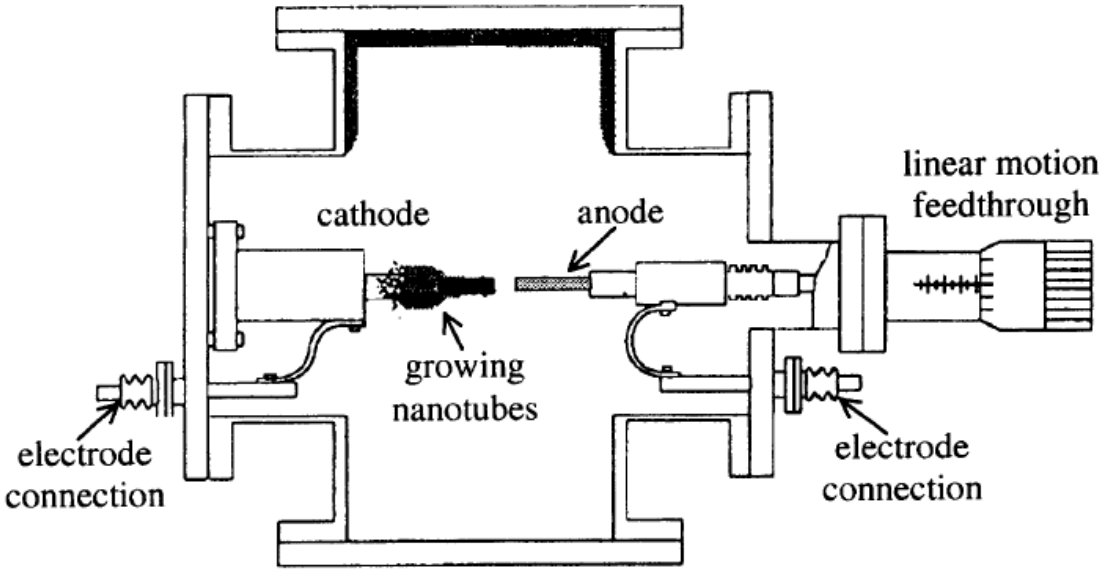

Figure 1.22 Schematic illustration of the arc-discharge technique[98]

The arc discharge technique is shown in Figure 1.22, Iijima first used this technique to synthesize carbon nanotubes[83]. The arc discharge technique used two high-purity graphite rods as anode and cathode. These two rods are put under a helium atmosphere and are applied by a voltage to generate a stable arc. The material then deposits on the cathode to form a build-up consisting of an outside shell of fused material and a softer fibrous core containing nanotubes and other carbon impurities[96].

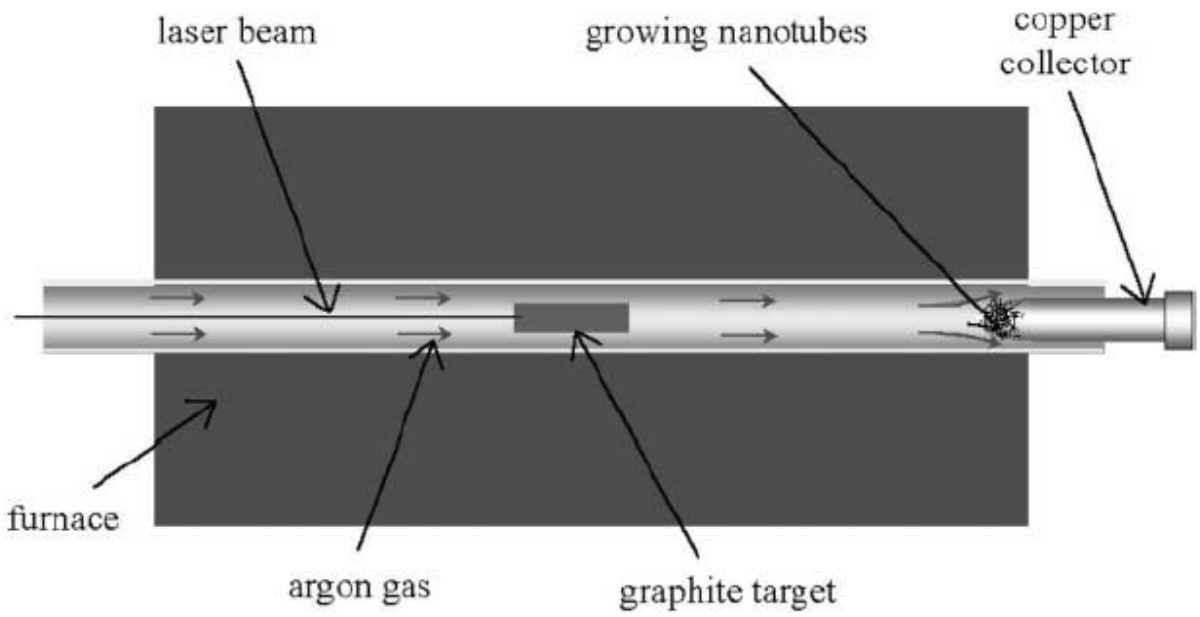

Figure 1.23 Schematic of the laser ablation process[99]

Figure 1.23 shows the laser ablation technique to synthesize carbon nanotube. The laser is used to vaporize a graphite target held in a controlled atmosphere oven at 1200℃. Nickel and cobalt are used as catalyst to produce the CNTs. The final product of CNTs are collected on a water-cooled target.

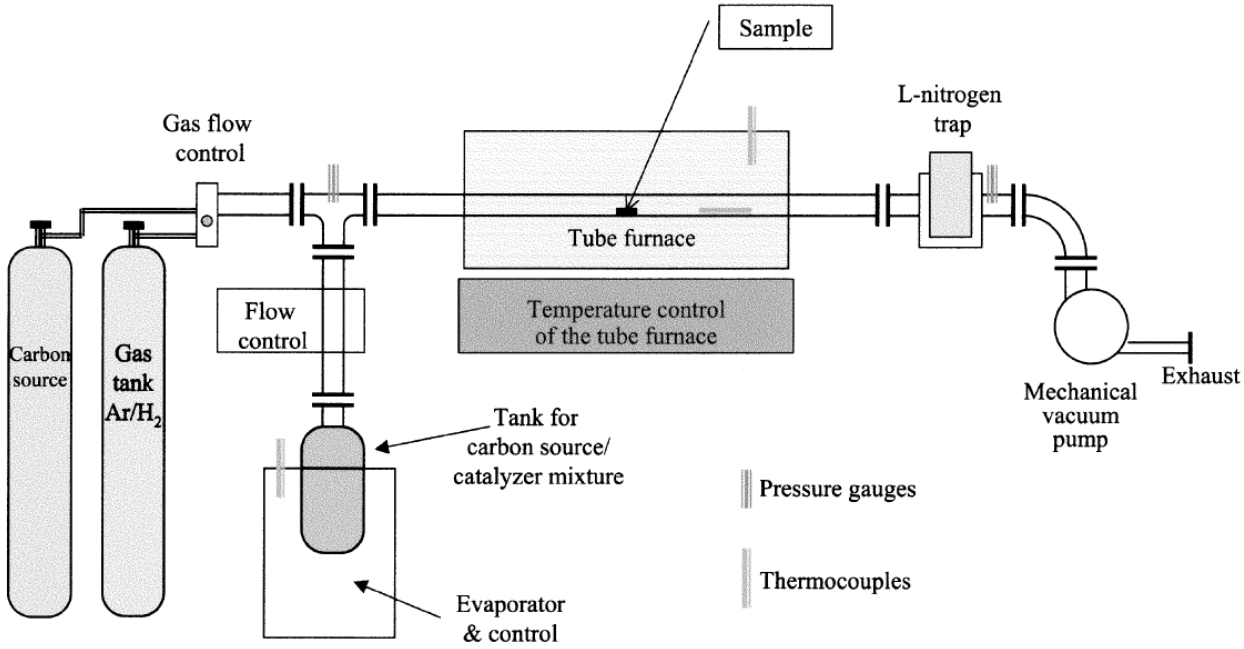

Figure 1.24 Schematics of the experimental setup used for CVD of multiwalled carbon nanotubes onto substrates using the floating catalyst method. The gas flow provides oxygen-free atmosphere for the pre-growth interval, and the carbon source-catalyst solution is evaporated from a separate bubbler. Temperature and pressure measurement and control is provided[100].

Although arc discharge and laser ablation techniques do have the ability to synthesize single-walled carbon nanotubes or multi-walled carbon nanotubes, they remain some problems such as limited volume of products and considerate amounts of undesirable by-products. Later, CVD are developed to solve these problems. The CVD technique is shown in Figure 1.24, the carbon source such as methane, acetonitrile, carbon monoxide decomposed into carbon radicles in the high temperature zone of tube furnace. These carbon radicles then deposited and assembled on the surface of catalyst such as nickel and iron. After the continuous reaction on the surface of catalysts, the length of CNTs was increased and finally formed a tubular structure with one end open.

1.2.5 Graphene

Graphene is a defect-free carbon monolayer packed into a 2D honeycomb lattice. It is the first 2-D atomic crystal which has excellent electronic and thermal conductivity, mechanical stiffness, strength and elasticity (table 1.3) [101 102]. Since it was first isolated in 2004[50], people have witnessed the boom of graphene in the field of electronic devices[103 104 105], optical devices[106 107 108] and electrochemical energy storage[101 109 110] (Figure 1.25). Currently, graphene is the hottest material for electrochemical energy storage, for several reasons: 1) The electron conductivity of graphene achieve around 2000 S cm^{-1}, which reduced overpotential and decreased charge-transfer resistance and thus increase the energy density and rate performance; 2) it has high surface area up to 2630 m^2 g^{-1}, which provide big chances for supercapacitor; 3) graphene has a Young's modulus of 1 TPa and intrinsic strength of 130 GPa[63], which can be used as carbon host for flexible batteries. Graphene can not only act as active materials by directly taking part in energy-storage mechanism, but also as a carbon matrix to form graphene-based composite materials. Although graphene has so many attractive properties for energy storage, the biggest challenge lies in the mass production. Due to its peculiar nature, the electrochemical properties of graphene are extremely depend on its method of production [101].

Table 1.3 Graphene properties compared with other carbonaceous materials[85].

	Graphene	Carbon nanotube	Fullerene	Graphite
Dimensions	2	1	0	3
Hybridization	sp^2	Mostly sp^2	Mostly sp^2	sp^2

Hardness	Highest (for single layer)	High	High	High
Tenacity	Flexible, elastic	Flexible, elastic	Elastic	Flexible, non-elastic
Experimental SSA ($m^2 g^{-1}$)	~1500	~1300	80-90	~10-20
Electronical conductivity ($S\ cm^{-1}$)	~2000	Structure-dependent	10^{-10}	Anisotropic: 2-3× 10^{4*}, $6^{\dagger}$
Thermal Conductivity ($W\ m^{-1}K^{-1}$)	4840-5300	3500	0.4	Anisotropic: 1500-2000*, 5-10†

*a direction, †c direction

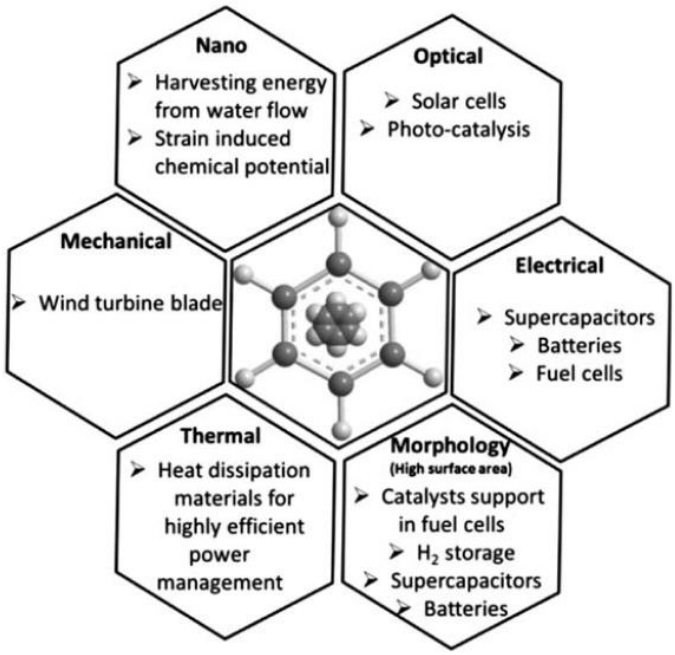

Figure 1.25 Relationship between graphene properties and their applications in energy solutions[111].

1.2.5.1 graphene production methods

Since graphene was first isolated in 2004, researchers have studied different production methods varied from physical exfoliation to chemical synthesis.

Mechanically exfoliation is the earliest method to obtain single layer graphene. Novoselov et al. prepared graphene film by repeated peeling small mesas of highly oriented pyrolytic graphite. For the first time, they proved the structure of single layered graphene which exhibit a strong ambipolar electric field effect[50].

Synthesis on Silicon carbide is another effective way. Since silicon atoms in SiC will sublimate under high temperature over 1000℃, A thin graphitic carbon layer can be formed on the carbon or silicon surface of SiC. This method can obtain high quality graphene, but the high cost of SiC and high reaction temperature make it hard for mass production[112].

Chemical vapor deposition is an efficient method to synthesis various amorphous and quality graphene. Since the catalyst activity used in CVD varies, people are able to control graphene layers by selecting related catalyst. For example, Xuesong Li et al. successfully synthesized high quality and uniform graphene films on copper foils by CVD process[113]. Because copper has lower catalyst activity than other metals such as nickel and magnesium, graphene catalyzed by copper tend to have fewer layer and exhibit better electrochemical properties, but the yield is very limited. Miller et al. produced vertically oriented graphene nanosheet by using nickel as catalyst, which have larger yield than graphene catalyzed by copper[114]. Also, it is the first time that graphene structure designed by controlling the amorphous of catalyst. Zongping Chen el al. reported a three-dimensional form-like graphene macrostructure by nickel foam template-directed CVD[115]. This interconnected flexible network of graphene showed conductivity up to 10 S cm^{-1} when combined with 99.5 wt% poly(dimethyl siloxane), which is ~6 orders of magnitude higher than chemically derived graphene-based composites.

Graphene can be also obtained by liquid phase exfoliation. Graphite intercalation compounds such as $KMnO_4$ in hummer's method was intercalated into graphene interlayer or the edge of graphene and then it disperses into a liquid environment to reduce the strength of the van der Waals attraction between graphene layers. By trigger the reaction between graphite intercalation compounds and other chemicals, it will release large amount of heat or bubbles which induce the exfoliation of graphite into graphene sheets. Suyun Tian et al. developed a controllable edge oxidation and bubbling exfoliation method to produce water dispersible graphene[116]. The reaction between intercalated $KMnO_4$ and hydrogen peroxide produce large amount of oxygen bubbles, which exfoliated the graphite into graphene sheets (Figure 1.26).

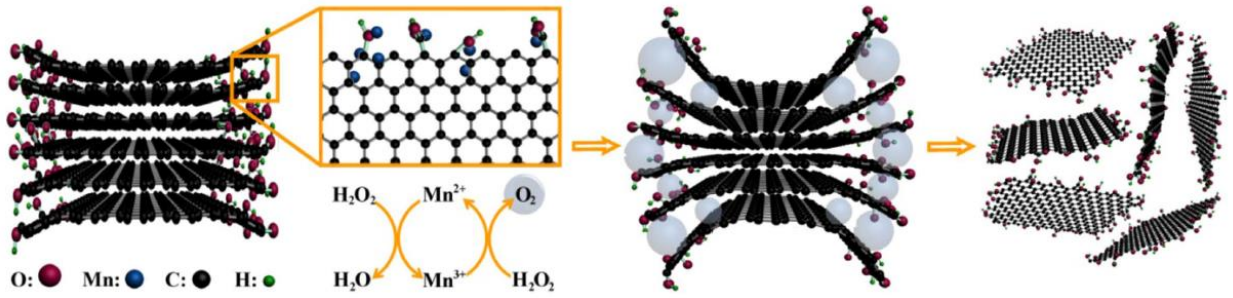

Figure 1.26 Bubbling exfoliation of edge oxidized graphite for water soluble graphene. (a) Schematic diagram of preparation process. Left: oxidation at graphite edges; middle: bubbling and exfoliation; right: dispersion.[117]

Reduction of graphene oxide (GO) is another effective way to synthesize graphene. Graphite pellets are first oxidized and then ultrasonically exfoliated in an aqueous solution to form GO. After exfoliation of graphite oxide the suspension may be further processed by centrifugation, and can then be deposited as a thin film on almost any surface and reduced (albeit partially) in situ back to the parent graphene state[118]. Voiry et al. adopted microwave method to reduce GO into pristine graphene, which has much higher I_{2D}/I_G in the Raman spectra than other rGO indicating the reorganization of the carbon bonding during microwave reduction[119].

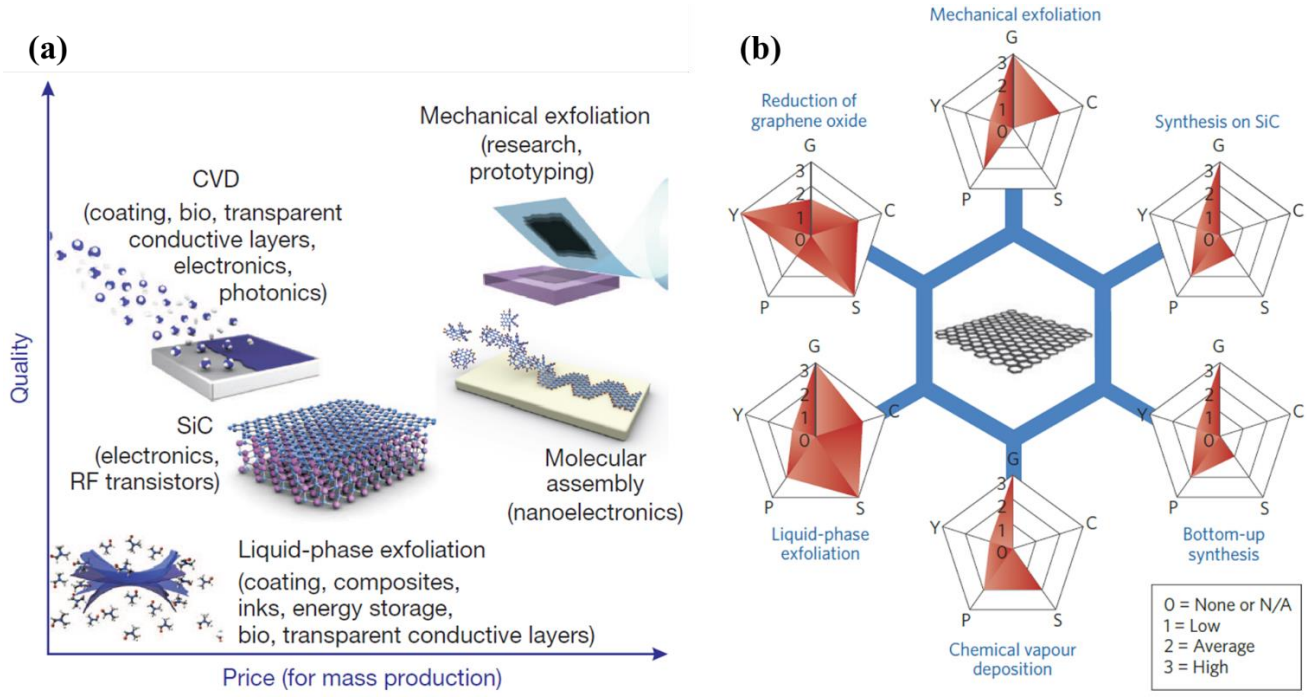

Figure 1.27 a There are several methods of mass-production of graphene, which allow a wide choice in terms of size, quality and price for any particular application[118]. **b** Schematic of the most common graphene production methods. Each method has been evaluated in terms of graphene quality (G), cost aspect (C); a low value corresponds to high cost of production), scalability (S), purity (P) and yield (Y) of the overall production process[101].

So far, people developed plenty of methods to synthesis graphene, but only a few of them can be applied in industrial mass production. Figure 1.27 shows the relation between price for mass production methods and the quality of graphene. Liquid-phase exfoliation has the lowest cost and impressive yield, however, the electrochemical performance and mechanical properties are low. The reduction of GO has the same problem with liquid-phase exfoliation, because it is hard to remove majority of defects on graphene oxide through normal reduction methods. Graphene synthesized by CVD exhibit high electron and thermal conductivity, moreover it can assemble into different framework to accommodate active materials with different character. But low yield and high cost render it only applied in computer chips and other precision instrument. Other synthesis

method such as synthesis on SiC, mechanical exfoliation of high oriented graphite and molecular assembly also suffered from these problems. In a word, to meet the requirement of industrial mass production, we need to develop a rapid, high efficiency and low-cost production approach to produce high yield graphene with good quality.

1.3 Graphene and graphene-based composites for Lithium-ion battery

1.3.1 Lithium-ion battery

Basically, Lithium ion batteries are composed of several parts: anode, electrolyte and cathode as shown on Figure 1.28. The anode side of lithium ion battery commonly use carbon-based materials; at the cathode side, lithium metal oxide is often used as active materials due to their stable crystal structure, high voltage window and thus high-energy densities. Both electrodes are able to reversibly insert and remove Li^+ from their respective structures. On charging, Li ions are removed or deintercalated from the layered oxide compound and intercalated into the graphite layers. The process is reversed on discharge. The electrodes are separated by a nonaqueous electrolyte that transports Li^+ between the electrodes[120].

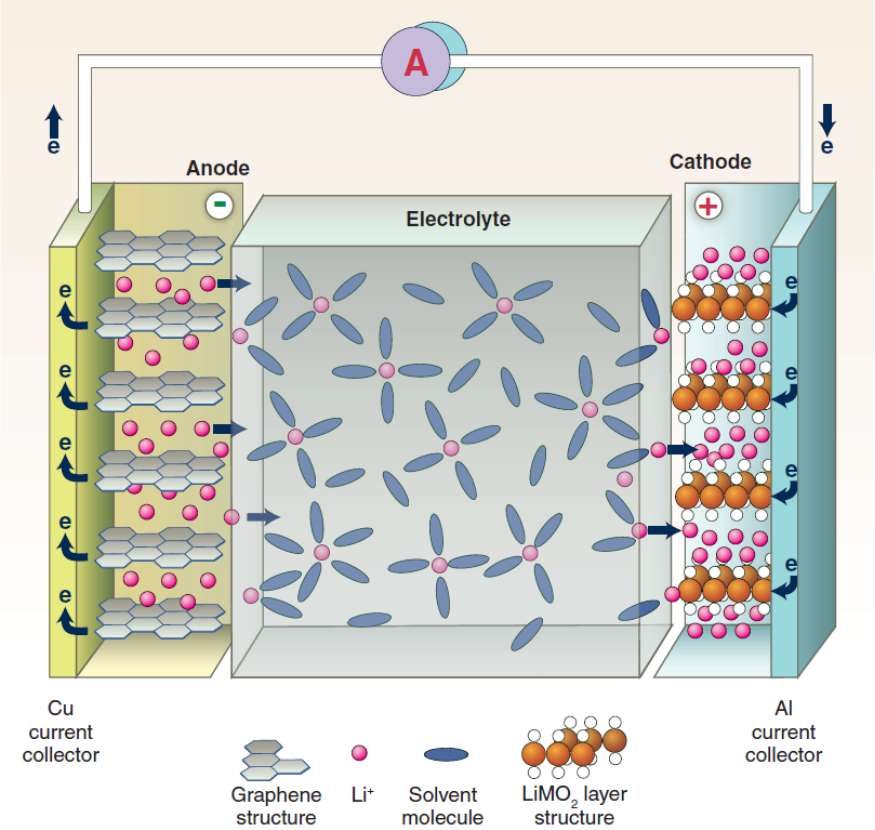

Figure 1.28 Schematic of a lithium ion battery with graphitic carbon anode and lithium metal oxide cathode. [120]

During the discharge process, the anode releases lithium ions into the electrolyte which is typically a lithium salt such as $LiPF_6$ dissolved in organic solvent, and then Li^+ ions transport to the cathode through this electrolyte where Li^+ ions was absorbed by cathode active materials:

$$Anode: Li_xC_6 \leftrightarrow xLi^+ + xe^- + 6C$$

$$Cathode: Li_{1-x}MO_2 + xLi^+ + xe^- \leftrightarrow LiMO_2$$

Similarly, during charge process, cathode releases lithium ions which then transfer to anode through electrolyte[121].

Nowadays, although lithium ion batteries have become the primary choice as power source for portable devices, researchers still need to develop new type of cathode, anode materials and new energy storage structure systems such as solid electrolyte batteries to improve the gravimetric energy density, power density, lifespan and safety for lithium ion batteries.

1.3.2 Cathode materials for lithium ion batteries

Since commercial cathode materials' available capacity is still lower than graphite or other carbon host lithium anode, it is very urgent to develop new type of cathode materials to improve the energy densities of whole battery system.

Commercial Li-ion batteries (LIBs) utilize intercalation-type cathode materials, mostly olivine $LiFePO_4$ (LFP), spinel LiMn2O4 (LMO), layered LiCoO2 (LCO), $LiNi_xMn_yCo_zO_2$ (NMC) and $LiNi_{0.8}Co_{0.15}Al_{0.05}O_2$ (NCA). These materials show specific capacities of up to ~200 mAh g^{-1} [122]. Tithium insertion compounds into 3 groups based on their crystal structure as shown in Table 1.4[123]. $Li[M]O_2$ (M=Ni, Co) has the same crystal structure with typical layered α-$NaFeO_2$ (space group R3m, No. 166): the transition metal and lithium ions occupy the octahedral sites of alternating layers with an "O3-type" stacking sequence like "ABCABC". $LiMn_2O_4$ (LMO) is the $A[B_2]O_4$ cubic spinel-type structure in the Fd3m space group (O_h^7 factor group): Mn ions occupy half of the octahedral interstices to form a 3D framework of edge-sharing MnO_6 octahedra, while lithium ions occupy tetrahedral sites, which share common faces with four neighboring empty octahedral sites at the16c position as shown in Figure 1.29. Olivine $LiFePO_4$ belongs to orthorhombic system (*Pnma* space group, No. 62): in this structure, lithium and iron located in half the octahedral sites and phosphorus ions occupy 1/8 of the tetrahedral sites, thus to form a

distorted hexagonal close-packed oxygen framework which enables the transportation of lithium ions.

Table 1.4 Electrochemical characteristics of the three classes of insertion compounds.[123]

Framework	**Compound**	**Specific capacity[a] (mAh g^{-1})**	**Average Potential (V vs. Li^0/Li^+)**
Layered	$LiCoO_2$	272 (140)	4.2
	$LiNi_{1/3}Mn_{1/3}Co_{1/3}O_2$	272 (200)	4.0
	$LiNi_{0.8}Co_{0.15}Al_{0.05}O_2$	279 (200)	3.7
Spinel	$LiMn_2O_4$	148 (120)	4.1
Olivine	$LiFePO_4$	170 (160)	3.45
	$LiFe_{1/2}Mn_{1/2}PO_4$	170 (160)	3.4/4.1

a Value in parenthesis indicates the practical specific capacity of electrode.

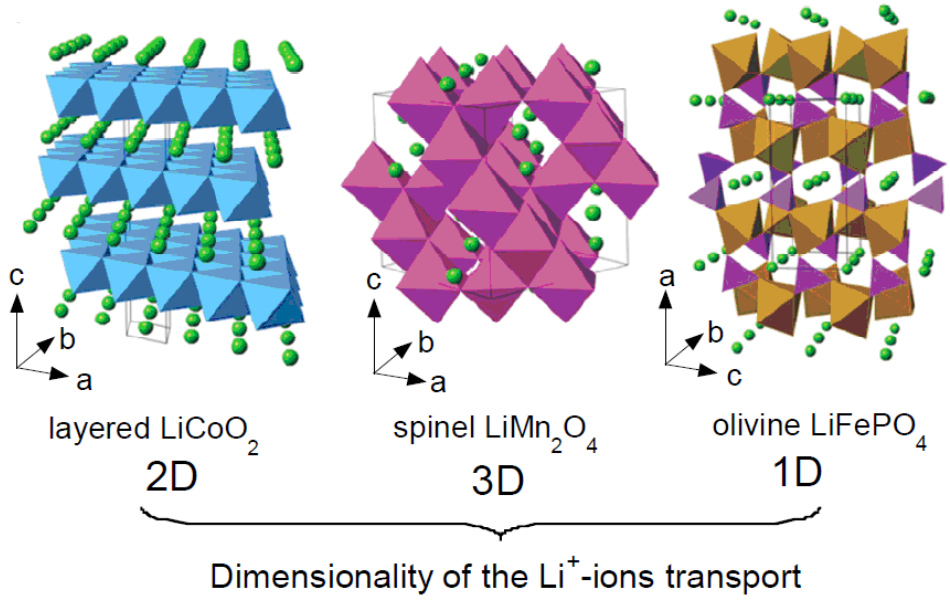

Figure 1.29 Crystal structure of the three lithium-insertion compounds in which the Li^+ ions are mobile through the 2-D (layered), 3-D (spinel) and 1-D (olivine) frameworks.

However, their limitations in energy density, cycle life, rate performance, cost and safety issues still impede mass application in long-range electric vehicles and large-scale grid application[124]. To improve the energy density of traditional cathode materials for LIBs, researchers developed other appealing active materials on the top of LMO and NMC. One is the high voltage spinel $LiNi_{0.5}Mn_{1.5}O_4$, which has 658 Wh kg^{-1} energy density; the other one is Ni-rich layered-structure NMC with nickel content $\geqslant 0.5$ (typically $LiNi_{0.5}Mn_{0.3}Co_{0.2}O_2$, $LiNi_{0.6}Mn_{0.2}Co_{0.2}O_2$ and $LiNi0_{.8}Mn_{0.1}Co_{0.1}O_2$), which has around 800 Wh kg^{-1} energy density; and Li-rich Mn-rich (LMR) layered-structure materials with 900 Wh kg^{-1} energy density[125] (Figure 1.30). We can find that these three new types of cathode have much higher energy density than traditional commercial cathode materials which provide the possibility to make electric vehicles with higher driving mileage for EVs to compete with traditional gasoline vehicles in the future.

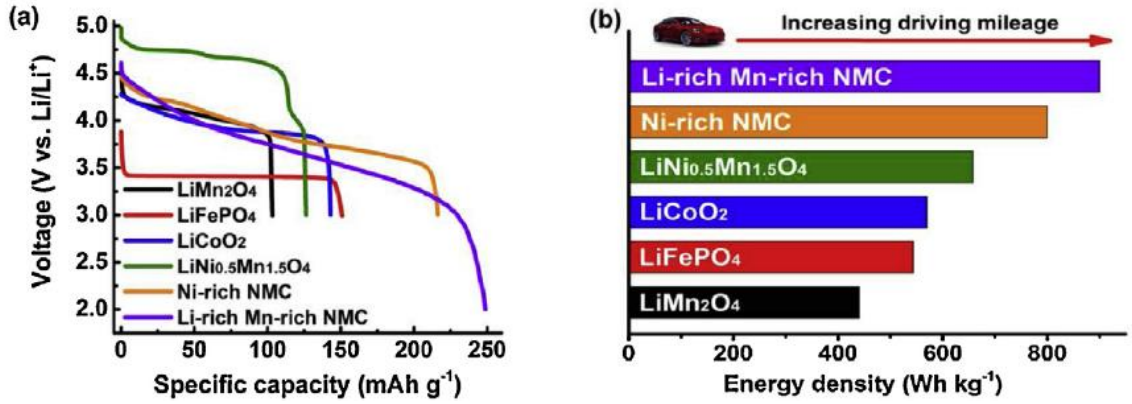

Figure 1.30 a Typical discharge voltage profiles of different cathode materials. **b** Energy density profiles of different cathode materials.

1.3.2.2 High Voltage Spinel cathode $LiNi_{0.5}Mn_{1.5}O_4$

Spinel cathode $LiNi_{0.5}Mn_{1.5}O_4$ is an attracting cathode material for LIBs due to its high energy density (658 Wh kg^{-1}), which is 1.5 times than previous generation spinel cathode LMO, high operating voltage up to 4.7V and good rate performance. There are two types of phase structures among $LiNi_{0.5}Mn_{1.5}O_4$, one is ordered $P4_332$ and the other one is disordered Fd–3 m. Figure 1.31 (c-d) shows these two structures: Ordered $LiNi_{0.5}Mn_{1.5}O_4$ with space group $P4_332$ has Li at tetrahedral 8a sites, Ni at octahedral 4b sites and Mn at octahedral 12d sites and O ions occupied at 8c and 24e sites, which allows all Ni^{2+} ions coordinated with six nearest neighboring Mn^{4+} atoms in the crystal lattice; Disordered $LiNi_{0.5}Mn_{1.5}O_4$ with space group Fd–3 m phase, Ni and Mn distribute randomly in the octahedral 16d sites in a ratio of 1:3, while Li and O are located in 8a and 32e sites.

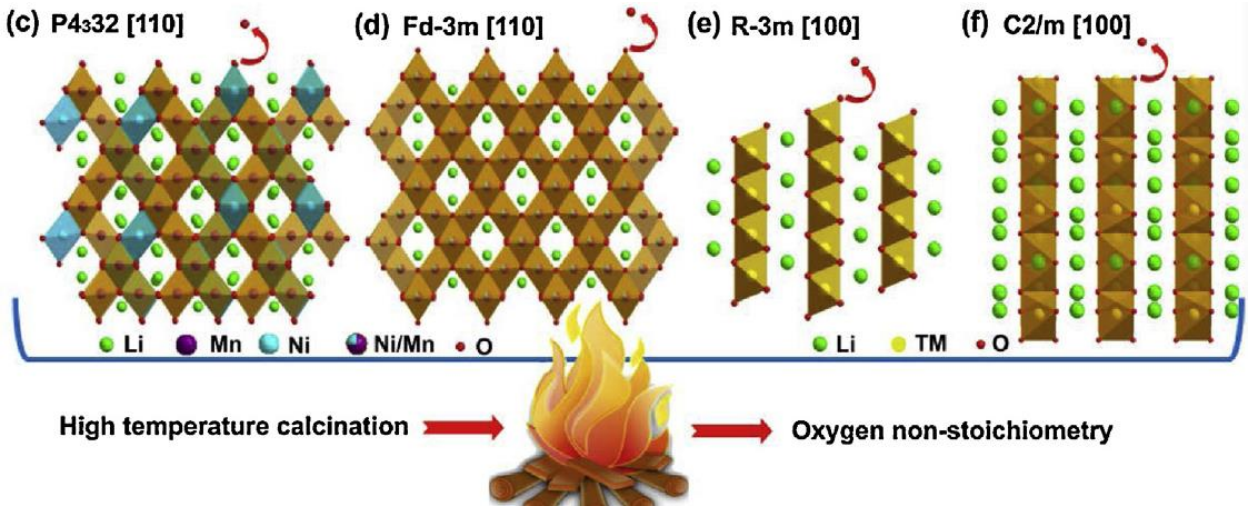

Figure 1.31 (c–f) Atomic models showing the (c) ordered spinel structure with space group P4332, (d) disordered spinel structure with space group Fd-3m, (e) layered structure with space group R-3m, and (f) monoclinic structure with space group C2/m. The fire represents the high temperature

calcination process that leads to the formation of non-stoichiometry in the as-prepared materials. TM = transition metal.

Due to the structural difference caused by oxygen non-stoichiometry which relate to the calcination temperature, the ordered and disordered $LiNi_{0.5}Mn_{1.5}O_4$ behave quite differently during the electrochemical charge/discharge processes. As shown in Figure 1.32 (a), the electronic conductivity of disordered Fd-3 m $LiNi_{0.5}Mn_{1.5}O_4$ is 2.5 orders of magnitude higher than that of ordered $P4_332$ spinel structure[126]. In the typical discharge curves of $LiNi_{0.5}Mn_{1.5}O_4$, the first two plateau around 4.7V is related to the redox reaction: $Ni^{4+}\leftrightarrow Ni^{3+}\leftrightarrow Ni^{2+}$. However, at 4.0 V, disordered spinel phase showed a voltage plateau related to the redox of Mn^{3+} which contributes to the overall capacity of $LiNi_{0.5}Mn_{1.5}O_4$. Moreover, as shown on Figure 1.32 (c), disordered spinel (800℃ calcination) exhibits superior capacity retention as compared to the ordered spinel (700℃ calcination), because disordered spinel $LiNi_{0.5}Mn_{1.5}O_4$ tends to have better electron conductivity and lithium ion diffusivity[127].

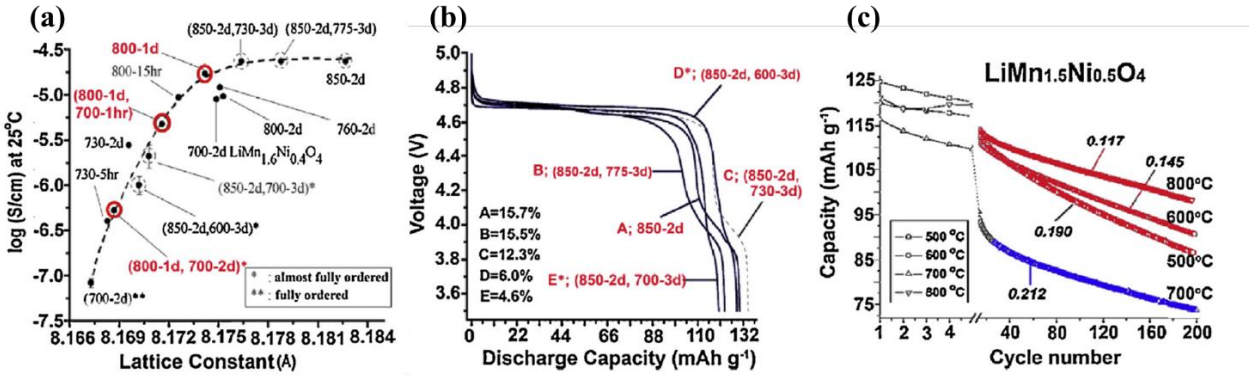

Figure 1.32 (a) Room-temperature conductivities of LiNi0.5Mn1.5O4pellets with respect to their lattice constants[126]. (b) Galvanostatic discharge curves of LiNi0.5Mn1.5O4. The percentage of capacity in the regionof ~4.0 V is also provided[126]. (c) Cycling performance of $LiNi_{0.5}Mn_{1.5}O_4$ prepared at different temperatures[127].

1.3.2.3 Ni-rich layered NMC cathodes

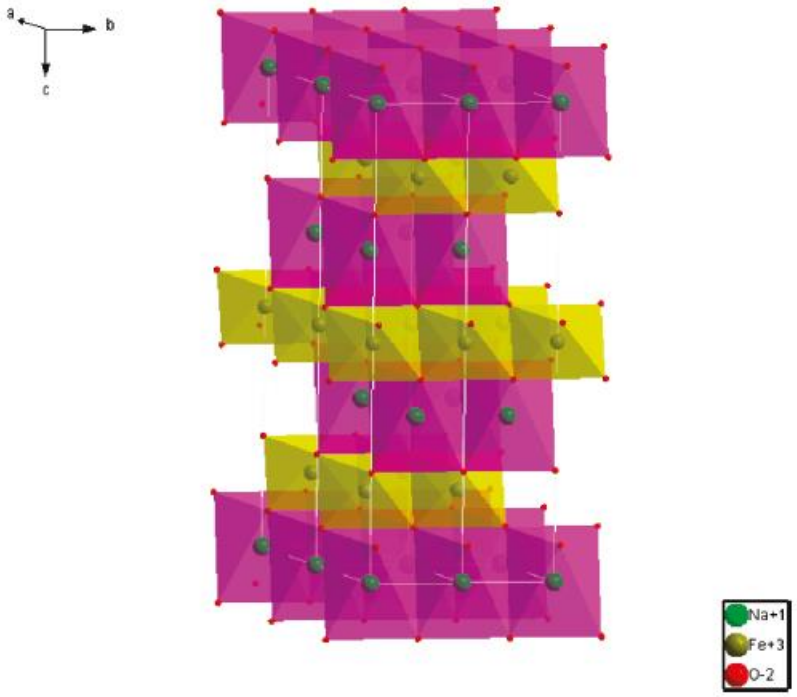

Figure 1.33 Structure of R-NaFeO2 (R3m). [128]

Ni-rich $LiNi_xMn_yCo_zO_2$ (NMC, $x \geqslant 0.5$) has the typical layered crystal structure with space group R-$NaFeO_2$ (R-3 m) as shown on Figure 6 (e). In the composition of NMC, nickel mainly contributes to the capacity of NMC cathode due to the transition of multivalent state during reduction reaction; Mn plays an important role in preventing the collapse of NMC crystal structure due to the insertion and extraction of lithium ion during discharge/charge process; Cobalt provides the good ability for high-rate performance. Therefore, Ni-rich NMC cathodes can provide higher capacity of 200-220 mAh g^{-1} than $LiNi_{1/3}Mn_{1/3}Co_{1/3}O_2$ (NMC 111) around

160 mAh g^{-1}, which make it become a promising cathode candidate. However, nickel-rich NMC still has some problems hindering its mass application for LIBs cathode materials. One of the biggest problem is the cation mixing between nickel and lithium ions, because the ionic radius of Ni^{2+} (0.069 nm) and Li^{+} (0.076nm) is very close, it is easy for Ni^{2+} to transfer into Li ions crystallographic 3a sites, at the same time, Li ions will transfer into 3b sites (Figure 1.33)[128]. In this way, Ni^{3+} is oxidized to Ni^{4+} during charge process and cause partially collapse of NMC lattice, which seriously lower the diffusivity of lithium ion in the NMC channel and finally deteriorate the electrochemical performance.

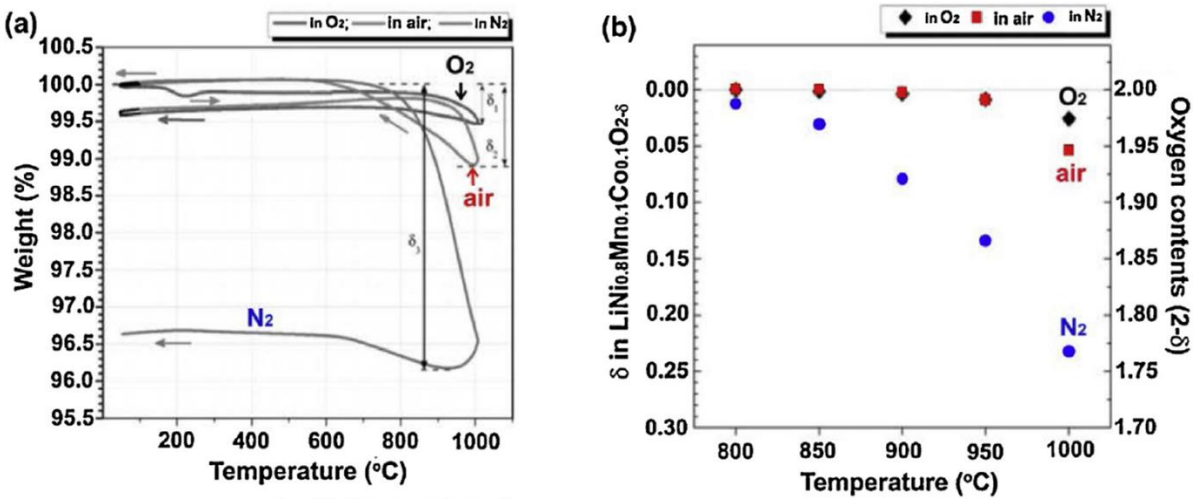

Figure 1.34 (a) TG curves for Ni-rich LiNi0.8Mn0.1Co0.1O2-δ samples heated and cooled sequentially in O2, air, and N2 atmospheres. (b) Oxygen content/non-stoichiometry as a function of temperature in different atmospheres. [129]

There are several modify methods that can impede cation mixing phenomena in Ni-rich NMC. The choice of appropriate calcination temperature and calcination atmosphere is one of the key roles in Li/Ni cation mixing. As we know, calcination temperature and atmosphere are key factors to decide the extent of non-stoichiometry in Ni-rich NMC cathode. Unlike the Co- and Mn- based

cathode, Ni-based cathode are more susceptible to oxygen loss which lead to the reduction of Ni from Ni^{3+} to Ni^{2+} whose ionic radius is closed to Li^{+}, thus make it easier to have a cation disorder process. It is studied by Idris et al. that increasing oxygen loss is observed to occur at temperature higher than 700℃ in N_2, 800℃ in air and 900℃ in pure O_2[129](Figure 1.34). Lee et al. studied the effect of calcination temperature and atmosphere on the structure and electrochemical performance of $LiNi_{0.6}Mn_{0.2}Co_{0.2}O_2$ (NMC 622)[130]. Typically, the oxygen in the calcination atmosphere increase the ratio of Ni^{3+}/Ni^{2+}, leading to a decrease of cation disorder between Li^{+} and Ni^{2+} according to the XPS data (Figure 1.35 (a-c)). Moreover, the presence of oxygen in the calcination also brings the uniformity of oxidation state of Ni ions from NMC surface to the bulk. For the electrochemical performance, as shown on Figure 1.35 (d-e), NMC 622 obtained in O_2 atmosphere shows higher specific capacity, better rate and long-term cycling performance (with capacity of 170 mAh g^{-1} at 0.1C and 89% capacity retention after 100 cycles). Therefore, Synthesize the Ni-rich NMC at an oxidative atmosphere and relatively low temperature is an effective way to reduce the oxygen non-stoichiometry of NMC and thus prevent the cation mixing and improve the electrochemical performance.

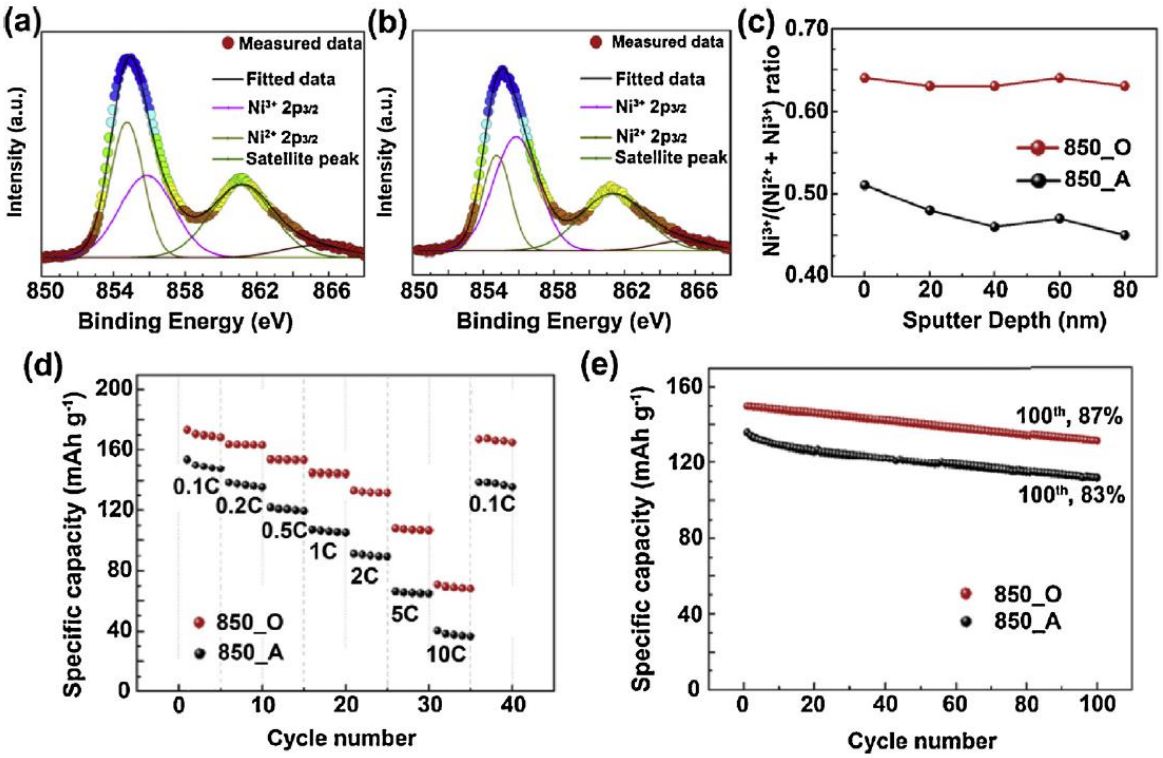

Figure 1.35 (a, b) Ni 2p3/2 X-ray photoelectron spectroscopy (XPS) spectral fitting for Ni-rich LiNi0.6Mn0.2Co0.2O2 prepared under different conditions: (a) 850 A (calcined in air at 850 ◦C) and (b) 850 O (calcined in O2 at 850 ◦C). (c) $Ni^{3+}/(Ni^{2+} + Ni^{3+})$ ratio as a function of sputtering depth for 850 A and 850 O. (d) Rate performance and (e) cycling performance of 850 A and 850 O tested at 1C rate. [130]

Doping modification is another effective method to reduce the Ni^{2+}/Li^{+} cation mixing phenomena. Jeffrey W. Fergus et al. believed that doping some metal ions can stabilize the structure of Ni-based cathode and increase lithium ions diffusivity[131]. Generally, these metal ions have similar ion radius with Li^{+}, stronger ionic force with oxygen and do not have Janh-Teller effect like nickel. Pouillerie et al. substituted a small amount of magnesium for nickel in $LiNO_2$ and they found that the Mg^{2+} migrate from the slab to the interslab to form a new cationic distribution in the lattice during first cycle[132]. These Mg^{2+} ions in the interslab space screen the O^{2-}—O^{2-} repulsion, thus act as pillars at the end of the deintercalation process to prevent the interslab

collapse. Yuan et al. studied the doping effect of Al, Mg, Li on $LiNi_{0.8}Mn_{0.1}Co_{0.1}O_2$ (NMC 811) cathode[133]. The doping of Mg^{2+} and Al^{3+} decrease the lattice parameter and increase I_{003}/I_{004} on XRD patterns (Figure 1.36 (a)) which indicate that the total amount of Ni^{2+} occupied in the Li layer, since the Mg^{2+} was preferentially located in the Li layer . The Mg-substituted sample performed high discharge capacity and the lowest capacity loss after 20 cycles with 92.5% capacity retention (Figure 10 (b)).

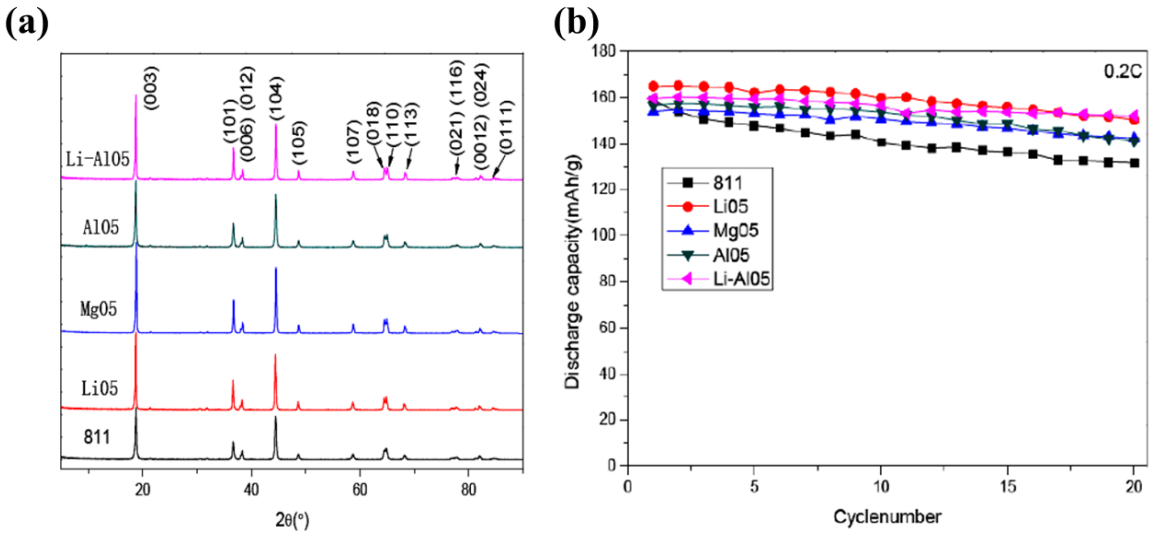

Figure 1.36 (a) XRD patterns of 811 with different ions doping (b) cycling performance of 811 with different ions doping at 0.2C[133].

Coating modification can also stabilize Ni-rich NMC crystal structure by preventing the crystal transformation, the dissolution of transition metals and side reaction between electrolyte and cathode. Chen et al. proved that TiO_2 coated on the surface of NMC 622 can significantly improve its discharge capacity, cycling stability and rate capability. This is because TiO_2 layer can suppress the interface reaction between the cathode and electrolyte, thus stabilizing the interface and reducing the impedance growth during cycling[134]. Graphene is a promising coating material candidate for two reasons: 1) good hydrophobic property, which keeps Ni free of moisture and

thus improve the cycling stability; 2) excellent electron conductivity, which can improve the capacity and rate performance of Ni-rich NMC cathode.

1.3.2.4 LMR layered-structure cathode

Lithium-rich Mn-rich LMR layered cathode materials with a composition of $xLi_2MnO_3 \cdot (1-x)LiMO_2$ (M=Mn, Ni, Co, or combinations), have been demonstrated to deliver even higher energy density of 900 Wh kg^{-1} than the high voltage spinel $LiNi_{0.5}Mn_{1.5}O_4$ and Ni-rich NMC cathodes[125, 135, 136]. Basically, LMR has two phase structure: one is trigonal R-3 m phase (Figure 6 (e)) integrated with C2/m Li_2MnO_3-like phase (Figure 6 (f)); the other one is sole homogeneous solid solution with C2/m monoclinic symmetry, as shown on Figure 6 (f). The electrochemical results show that LMR can deliver a capacity of 250 mAh g^{-1} at 0.1C, 60℃ (Figure 1.37)[137]. However, the rate performance of LMR is still limited due to its poor electron conductivity and lithium ion diffusivity and slow charge transfer reactions that occur at the electrode/electrolyte interface[138].

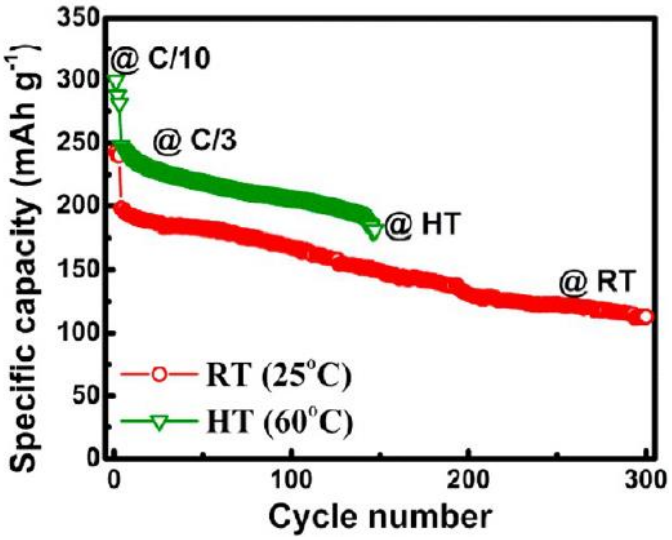

Figure 1.37 Cycling performance at RT(~25 °C) and HT(60 °C). [137]

In all, up-to-date emerging technologies on lithium-insertion compounds cathode for LIBs give us insights to develop high capacity, long life-time and low-cost cathode materials. However, due to the inherent properties of poor electron conductivity and lithium diffusivity, it is hard for lithium-insertion compounds to achieve high rate performance to fulfill the high-power demand of EVs. At this point, as one of the hottest carbon host, graphene with both excellent electronic conductivity and good lithium ions diffusivity provide attractive chances for this situation.

1.3.3 Anode materials for lithium ion batteries

Anode materials is of the same importance with cathode materials in lithium ion batteries. They together decide the energy capacity, rate performance and cycle life of the whole battery system. The performance of lithium-ion batteries not only depends on the intrinsic properties of anode materials such as theoretical specific capacity, lithium ion diffusion rate and electronic conductivity, but also hinges on the architecture design, particle size and component state.

Although some anode materials exhibit outstanding inherent properties which make it a competitive candidate electrode of lithium-ion batteries, the issues accompanied with discharge/charge process such as volume expansion, side reactions, irreversible structure transitions make it impossible to directly applied in LIBs and commercialize. Table 1.5 shows several anode materials and their advantages as well as disadvantages. For example, Silicon has ultra-high gravimetric capacity (3579 mA h g^{-1}) compared to carbon materials (e.g. graphite, 372 mA h g^{-1}) and transition metal oxide (600-1000 mA h g^{-1}) which brings it an inborn advantage as

anode materials. But silicon experiences a volume expansion during the lithiation process, which cracks active materials, lower the reversible capacity and cause safe issues. Graphite is very stable during the insertion and extraction process of lithium, but the low lithium ion diffusion rate lead to a limited rate performance.

Table 1.5 The advantage and disadvantage of different anode materials[139-144].

	ADVANTAGES	DISADVANTAGES
CARBON	(1) High electronic conductivity	(1) Low specific capacity
	(2) Nice hierarchical structure	(2) Low rate capacity
	(3) Abundant and low-cost resources	
ALLOYS	(1) High specific capacity (400-2300 mA h g^{-1})	(1) Low electronic conductivity
	(2) Good stability	(2) Large volume change (100%)
TRANSITION METAL OXIDE	(1) High specific capacity (600-1000 mA h g^{-1})	(1) Low coulombic efficiency
	(2) Nice stability	(2) Large potential hysteresis
SILICON	(1) High specific capacity (3579 mA h g^{-1})	(1) Large volume expansion (300%)
	(2) Rich, low-cost, clean resources	(2) Safety issues

Therefore, nanotechnology is needed to design and fabricate specific architectures of active anode materials to solve their problems. Firstly, By using nanotechnologies, the nanoscale materials have much shorter lithium diffusion length than traditional materials, which contribute to accelerate lithium ion diffusion rate according to the equation:

$$\tau = \frac{{L_{ion}}^2}{D_{Li}}$$

Where L_{ion} is the lithium ion diffusion length, which is relevant to the size of particles and architecture of lithium ion transport path; D_{Li} is the diffusion coefficient, which is a inherent property of the materials. Secondly, the nanosizing of active materials will significantly increase the surface area. This enlarged surface area helps to improve the adsorption of Li^+ in the electrolyte and thus contributes to a higher battery capacity as a result of the modification of the phase transition boundary and the augmentation of the surface and interfacial area[144-147]. Thirdly, some nanotechnologies can help to build a functional architecture to solve the intrinsic drawbacks of active materials. For example, an edge-activated graphite-silicon electrode exhibited better rate performance than graphite anode caused by the improvement of lithium ion diffusion rate on the graphite surface[148] (Figure 1.38 a); And a yolk shell carbon-silicon composite which has a vacancy between the silicon core and carbon shell can accommodate the volume expansion of silicon during the lithiation process[149] (Figure 1.38b).

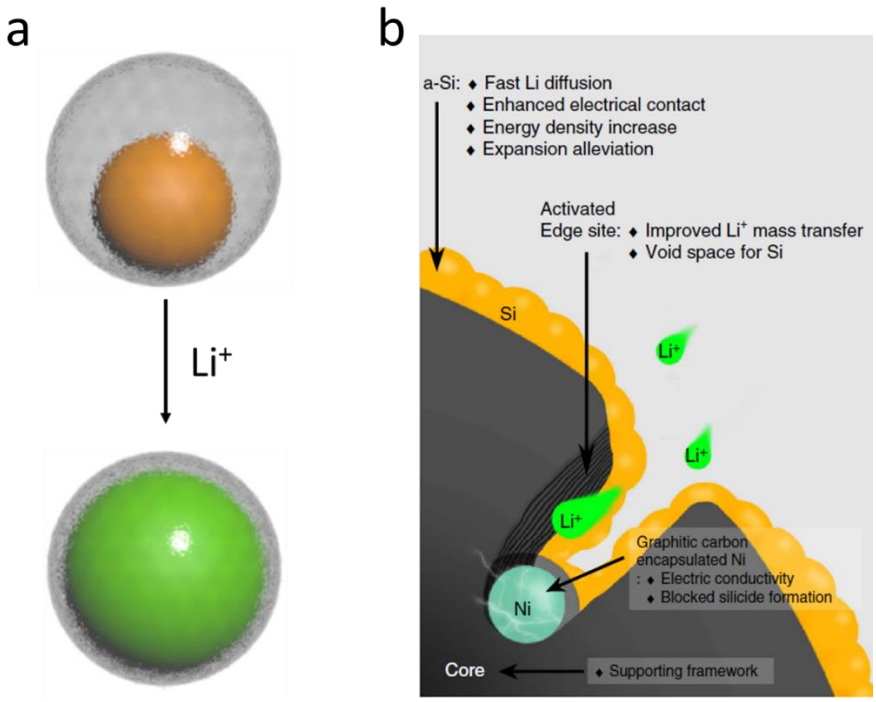

Figure 1.38 a A magnified schematic of an individual Si@void@C particle showing that the SiNP expands without breaking the carbon coating or disrupting the SEI layer on the outer surface[149]. b Cross-sectional illustration showing the detailed structural characteristics of Si/Edge-activated graphite[148].

1.3.3.1 Carbonaceous anode

Carbonaceous anode materials are one of the earliest active materials that have applied in lithium ion batteries. The structure of carbon materials is quite stable during the charge/discharge process. Thus, they have better cyclability and less side reaction than silicon, alloy or metal oxide. Moreover, carbonaceous anodes exhibit lower discharge plateau of potential than metal oxides, chalcogenides, and polymers[150], leading to a higher energy density when matched with a cathode. Apart from some no-graphitized soft carbon and hard carbon which have large irreversible capacity and low density, most carbonaceous anode materials are involved with graphene layer structures.

Graphite is the most successful commercialized anode material in LIBs. It has a layered structure which is stacked by graphene layers in the sequence of ABABA. This layered structure creates an ideal container for lithium ions that Li^+ can easily insert or extract in the graphite interlayers. The intercalation process occurs with the formation of Li-carbon alloys (Li_xC_n) in a reversible reaction[151]:

$$Li_xC_n \overset{Charge/discharge}{\Longleftrightarrow} xLi^+ + xe^- + C_n \ (n = 6)$$

It is noted that highly crystalline graphite can form a stage-1 lithium-graphite intercalation compound where every six carbon atoms take one lithium atom. Ideally, this reversible process can possess a theoretical capacity of 372 mA h g^{-1}.

Rajeeva R. Agarwal and J. Robert Selman first discovered the reversible intercalation behavior of Li ions into graphite interlayers in 1986[48], and used Li intercalated graphite to substitute lithium metal as anode in LIBs, which significantly improve the safety of LIBs. Graphite anodes can keep stable structure after long charge/discharge cycles and exhibit high initial coulombic efficiency, but improvement of their gravimetric capacity and rate performance is still required. Expanded graphite and graphite intercalation compounds were then used as anodes of LIBs. Fei Wang et al. develop a new type anode material using $FeCl_3$-graphite intercalation compounds (Figure 1.39)[152]. The $FeCl_3$ existed in the graphite interlayers can provide more capacity by reacting with Lithium ions:

$$FeCl_3 + 3Li^+ + 3e^- \leftrightarrow Fe + 3LiCl$$

Thereby, $FeCl_3$-GICs exhibits a reversible capacity as 500 mA h g^{-1} with 100% capacity retention after 400 cycles. This $FeCl_3$-GICs anode gives a promising carbon matrix model for LIBs. Compared with other carbon coating methods, GICs provide a more stable buffer matrix to

accommodate volume change and increase the overall electronic conductivity of composites electrode.

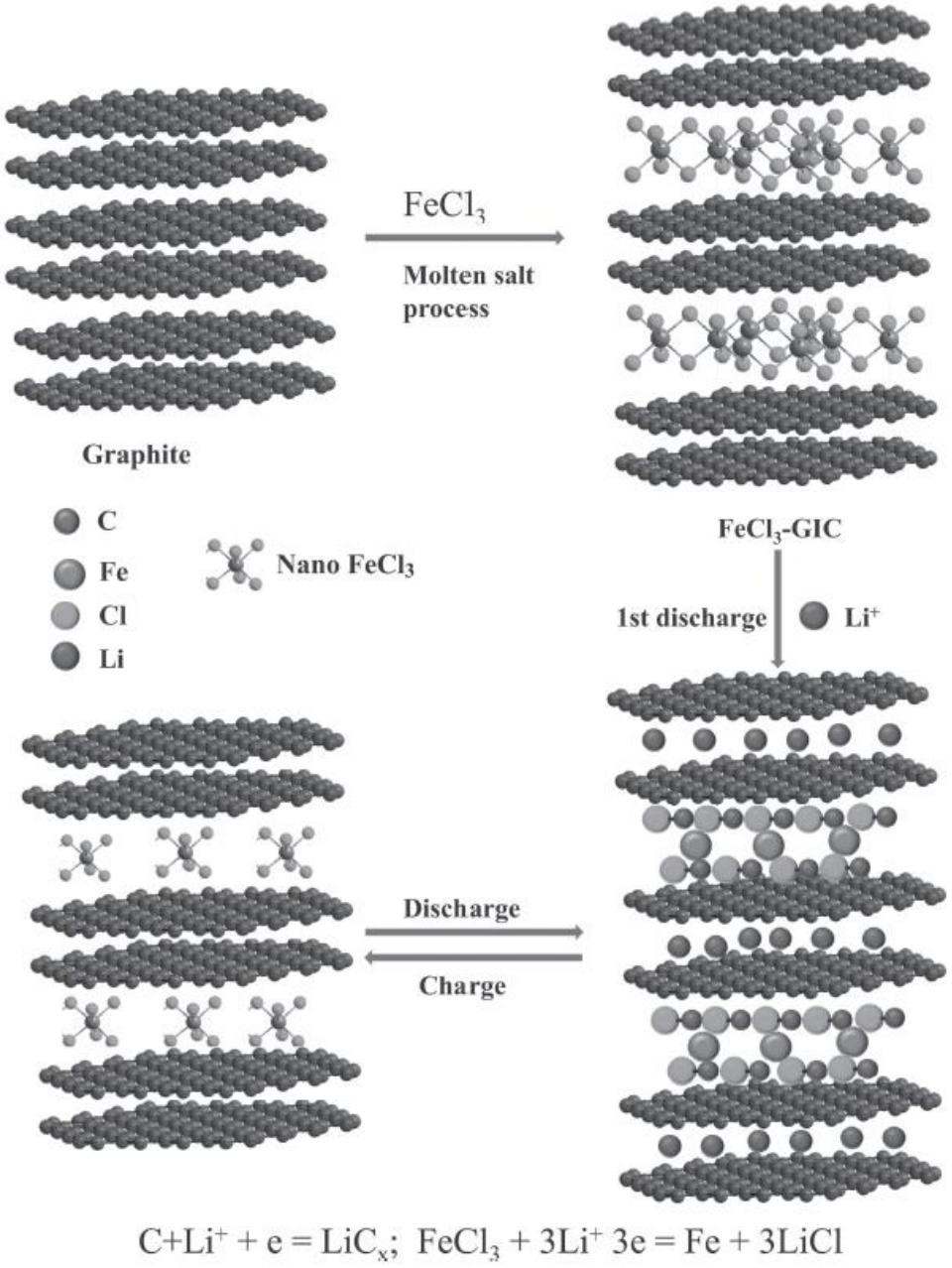

Figure 1.39 Schematic illustration of the structure and the mechanism of Li reactivity of $FeCl_3$-GIC[152].

In addition to graphite and graphite-based composite anodes, graphene derived anode materials also show good electrochemical performance. They include: 1-D carbon nanotubes, 2-D graphene sheets and 3-D graphene.

1-Dimmensional CNTs generally can be visualized as a sheet of graphene that has been rolled into a tube. Compared with traditional graphite anodes, CNTs have been proven to have higher capacity up to 1116 mA h g^{-1}, because the lithium ions can be adsorbed to both the internal and external walls of CNTs[153, 154] and delocalization of electrons of CNTs increase the degree of lithium intercalation[155]. However, the coulombic efficiency decreases a lot after long cycles, due to the barrier for the extraction of lithium ions during the discharge process[156, 157]. To solve this problem, researchers tried to combine CNTs with other active materials such as metal oxide[158-160], chalcogenides[161, 162] or other forms of carbonaceous materials[163, 164] (Figure 1.40).

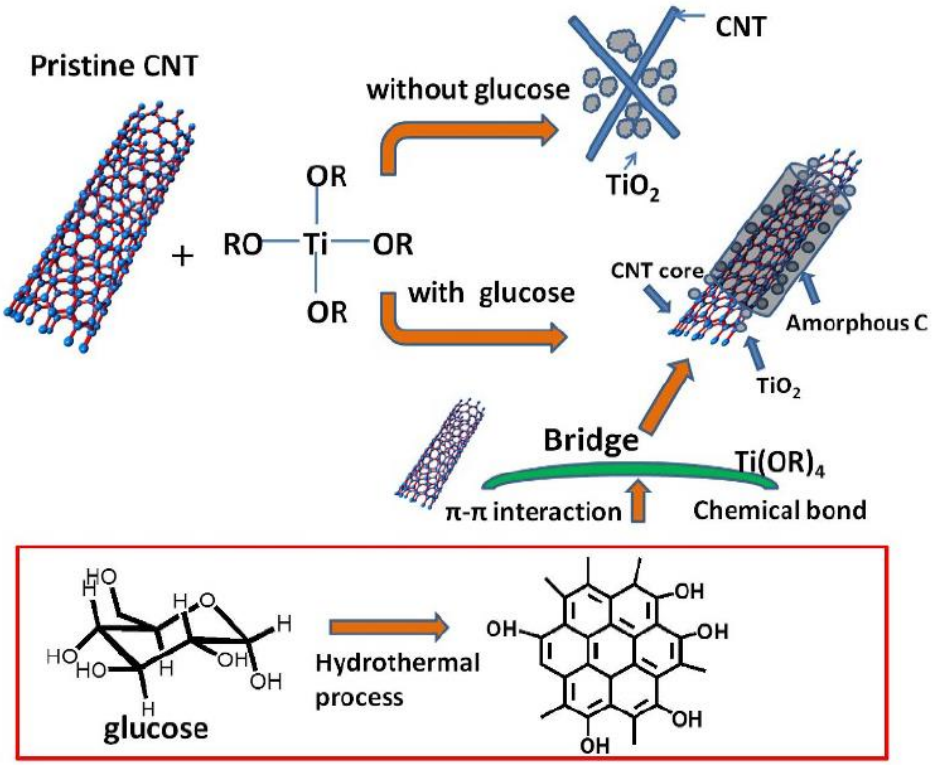

Figure 1.40 Schematic illustration of the one-pot hydrothermal routine to prepare CNT@TiO2-C nanocable with the assistance of glucose[160]

2-Dimmensional graphene sheets are also used as anode materials for LIBs, solely or in hybrid form[165] (Figure 1.41). The advantages of 2-D graphene sheets as anode materials are the ultra-high electronic conductivity, excellent mechanical strength and elasticity, high lithium storage capacity and high surface area. Since the lithium ions can be adsorbed in both sides of the graphene sheets, the graphene sheets anode exhibits high specific capacity up to 672 mA h g^{-1}. However, it suffers from unavoidable irreversible capacity and low initial coulombic efficiency due to the side reaction of lithium ions with oxygen containing defects and formation of SEI on the defect spots[121].

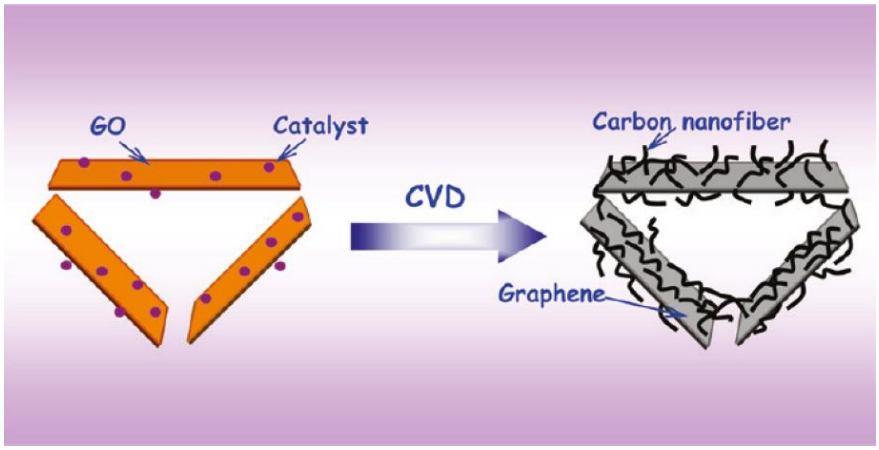

Figure 1.41 Illustrations of the fabrication of GNS/CNF composite via a CVD approach using a fluidized bed reactor[165]

3-D graphene is reported to be another competitive anode material for LIBs. Runwei Mo et al. synthesized a nitrogen-doped mesoporous graphene through CVD with MgO as the catalyst and template[64] (Figure 1.42). It shows high reversible capacity and outstanding rate performance (e.g., 1,138 mA h g^{-1} at 0.2 C or 440 mA h g^{-1} at 60 C). However, this 3-D graphene have to proceed a

microwave treatment to decrease the content of defects on graphene which complicate the fabrication process, otherwise the defects of MgO catalyzed graphene will lead to a low initial coulombic efficiency.

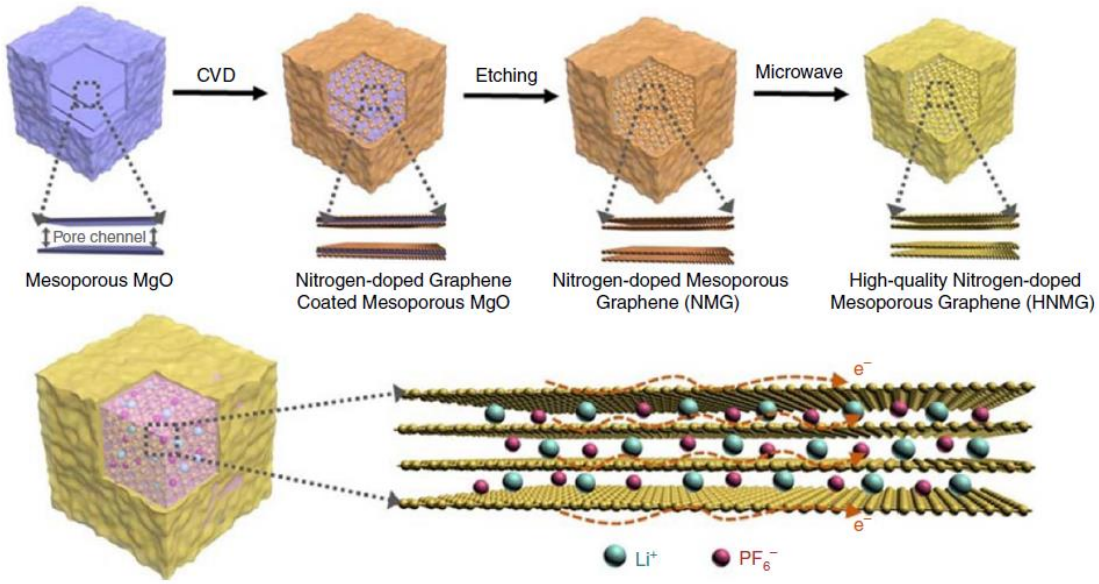

Figure 1.42 A schematic illustrating the synthesis of high-quality, nitrogen-doped, mesoporous graphene (HNMG) particles[64]

1.3.3.2 Spinel structured $Li_4Ti_5O_{12}$ (LTO) anode

Spinel structured $Li_4Ti_5O_{12}$ was first reported by Thackeray's group in 1994[166]. $Li_4Ti_5O_{12}$ shows a capacity of ~170 mA h g^{-1} which is lower than graphite (372 mA h g^{-1}), but it has much better cyclic stability due to zero strain or volume change during the charge and discharge processes[145, 167]. However, poor electrical conductivity (10^{-13} S cm^{-1}) and moderate Li^+ diffusion coefficient (10^{-9} to 10^{-13} cm^2 s^{-1}) contribute to a limited rate performance.

Conductive coating and minimize the particle size are good solutions to overcome the challenges. For example, Zhujun Yao et al. combine N-doped $Li_4Ti_5O_{12}$ with highly conductive TiC/C skeleton to improve the rate performance of LTO[168] (Figure 1.43). The conductive skeleton

TiC/C was prepared through a CVD process, then LTO was grown on the surface of TiC/C using a hydrothermal approach. N-LTO@TIC/C composites were finally synthesized after a NH_3 doping process. It shows an enhanced rate capability of 143 mA h g^{-1} at 10C and 122 mA h g^{-1} at 50C. Jaiswal et al. studied the size impact on electrochemical performance. They fabricated $Li_4Ti_5O_{12}$ with different size distribution of 50 nm and 200 nm through pyrolysis, which possessed specific capacity of 148 and 138 mA h g^{-1} at 0.04C and 5C, respectively[169].

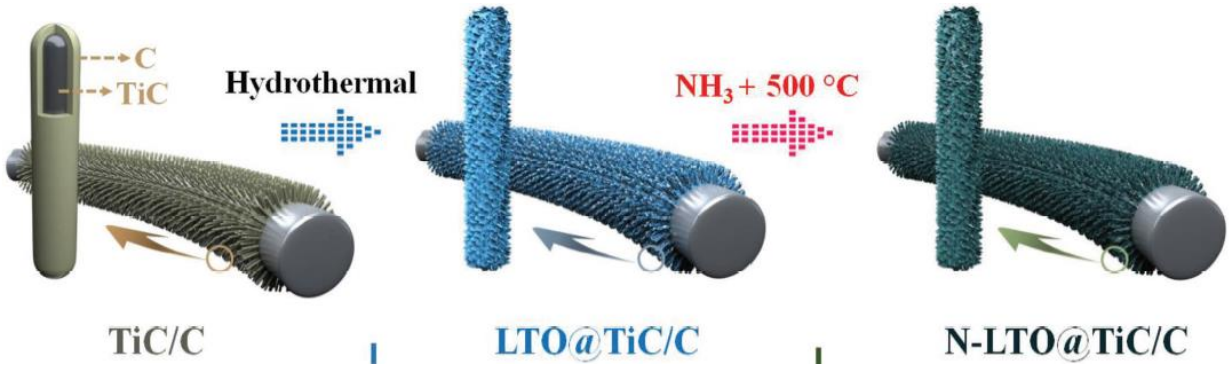

Figure 1.43 Fabrication schematics of N-LTO@TiC/C core–branch arrays[168]

1.3.3.3 Silicon based anode

Silicon is one of the most promising anode material of lithium ion batteries due to its ultra-high theoretical capacity up to 4212 mA h g^{-1}, because every silicon atom can accommodate 4.4 lithium atoms, forming the alloy $Li_{4.4}Si$. However, the major drawback of silicon anode is the volume expansion (400%) during the lithiation process and formation of SEI layer at low potential[121]. This huge volume expansion rate will crack the active materials leading to a capacity fading and poor cyclability. To solve the major problem of silicon, two directions of research are involved, of which the former solution is to minimize the particle size while the latter is to design a architecture to accommodate the volume change and make the composites more stable.

Li et al. synthesized Si nanoparticles with a diameter of 78 nm, which exhibits a high reversible capacity of 1700 mA h g^{-1} at a voltage window of 0-0.8 V[170]. Kim et al. synthesized N-Si nanoparticles with a diameter of 5-20 nm with a carbon coating, which possessed ~3500 mA h g^{-1} charge capacity with a retention of 96% up to 40 cycles[171].

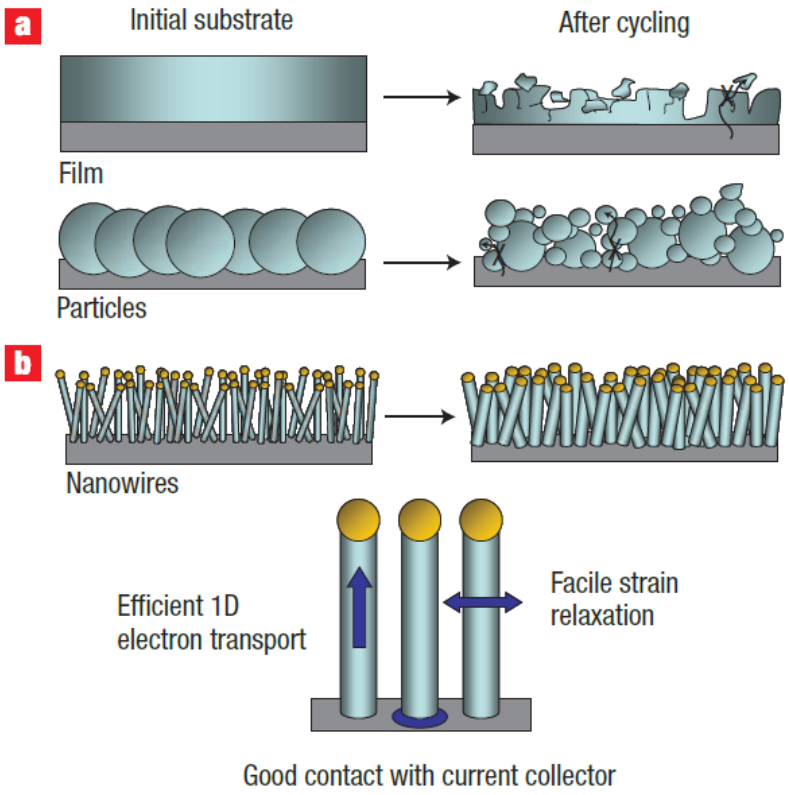

Figure 1.44 Schematic of morphological changes that occur in Si during electrochemical cycling. a, The volume of silicon anodes changes by about 400% during cycling. As a result, Si films and particles tend to pulverize during cycling. Much of the material loses contact with the current collector, resulting in poor transport of electrons, as indicated by the arrow. b, NWs grown directly on the current collector do not pulverize or break into smaller particles after cycling. Rather, facile strain relaxation in the NWs allows them to increase in diameter and length without breaking. This NW anode design has each NW connecting with the current collector, allowing for efficient 1D electron transport down the length of every NW[140].

The architecture of Si anodes developed from 1-D nanowire to 3-D yolk-shell sphere. Candace K. Chan et al. synthesized 1-D Si nanowire anode material of LIBs through a vapor-liquid-solid

process[140]. It can accommodate large strain without pulverization and exhibits a high capacity of ~2100 mA h g^{-1} even at 1 C rate (Figure 1.44). 2-D silicon nanosheets were successfully fabricated through the magnesiothermic reduction of mesoporous silica by Song Chen et al[172] (Figure 1.45). The reversible capacity of carbon coated Si nanosheets can achieve 1072.2 mA h g^{-1} at 4 A g^{-1} after 500 cycles.

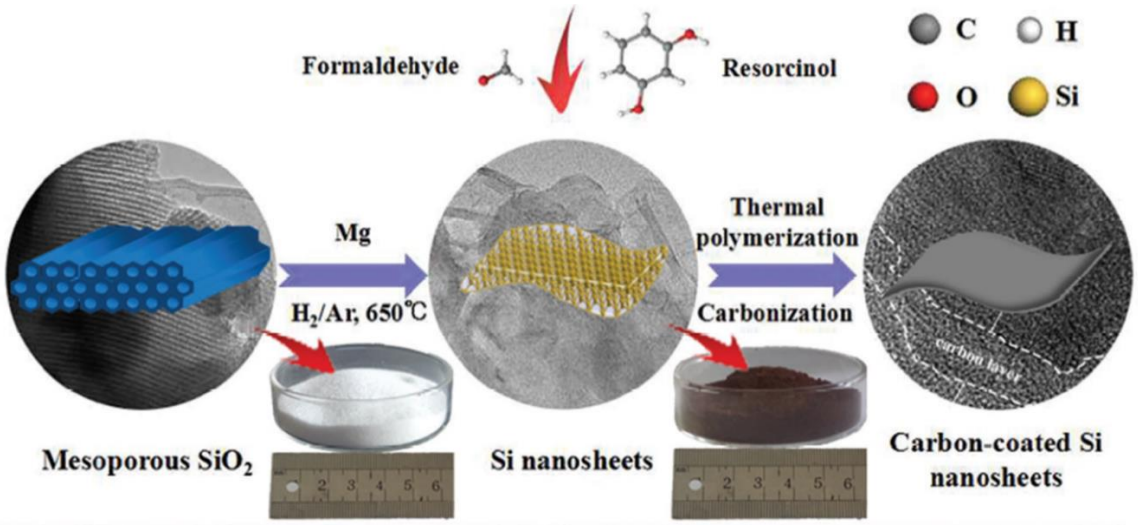

Figure 1.45 Schematic illustration for the synthesis of nanosheets[172]

3-D yolk-shell Si nanoparticles was first reported by Nian Liu et al. in 2012[149] (Figure 1.46). In this work, commercially available Si nanoparticles were sealed inside carbon shells with rationally designed void space. This void space in between the particles and the shell helps to accommodate the volume expansion of Si during the lithiation process. Thereby the yolk-shell Si nanoparticles exhibited high capacity of ~2800 mA h g^{-1} at 0.1C and long cycle life (1000 cycles with 74% retention rate).

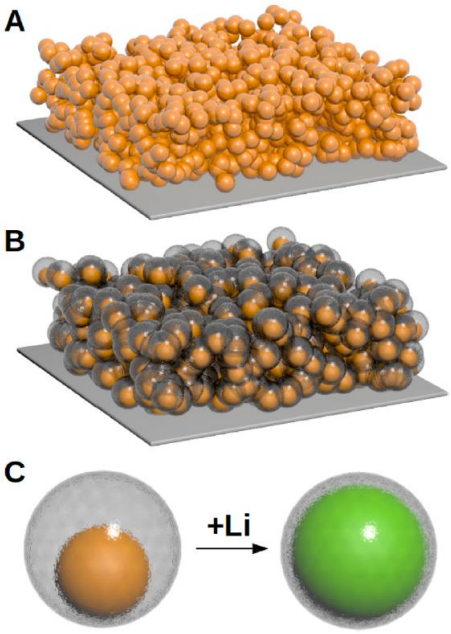

Figure 1.46 Schematic of the materials design. (A) A conventional slurry coated SiNP electrode. SEI on the surface of the SiNPs ruptures and reforms upon each SiNP during cycling, which causes the excessive growth of SEI and failure of the battery. The expansion of each SiNP also disrupts the microstructure of the electrode. (B) A novel Si@ void@C electrode. The void space between each SiNP and the carbon coating layer allows the Si to expand without rupturing the coating layer, which ensures that a stable and thin SEI layer forms on the outer surface of the carbon. Also, the volume change of the SiNPs is accommodated in the void space and does not change the microstructure of the electrode. (C) A magnified schematic of an individual Si@void@C particle showing that the SiNP expands without breaking the carbon coating or disrupting the SEI layer on the outer surface[149].

1.3.4 Graphene-based composite materials for lithium ion batteries

In addition to be directly used as an active material as we discussed in section 1.3.2, graphene can be proposed as a conductive agent in lithium ion batteries or act as a highly conducting carbon matrix to form composite electrode with other active materials.

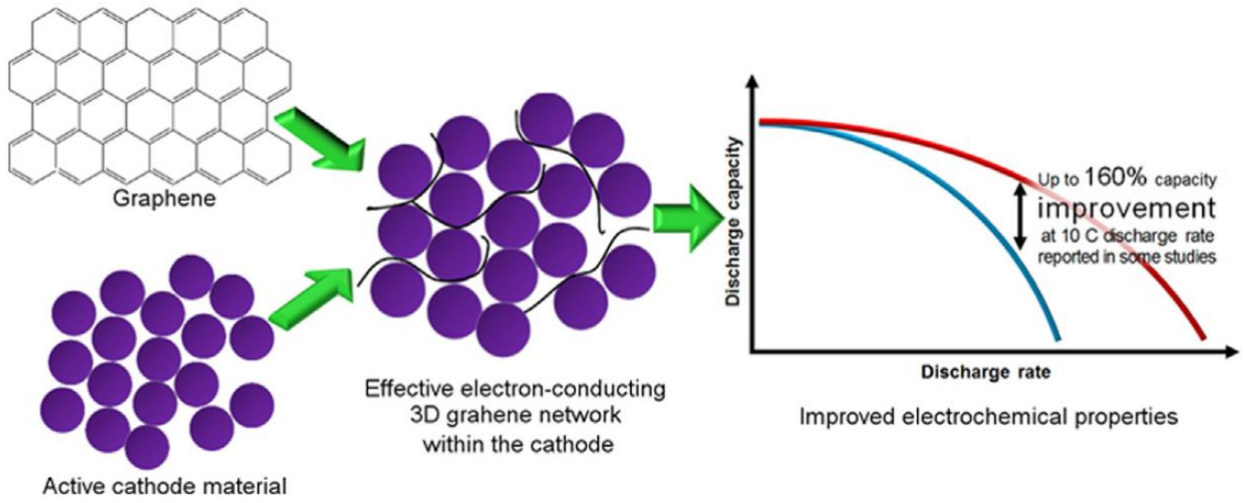

Figure 1.47 Schematic of making graphene-based composite cathode materials and the improvement of electrochemical performance after adding graphene[173]

Compared with conventional carbon additives or carbon coating such as soft or hard carbon as well as polymer derived carbon, graphene has highly crystalline structure that sp^2 bonded carbon atoms are packed into hexagonal 2-D honeycomb lattice. Within this more crystalline structure, the electrons shared in the delocalized π bonding contribute to the extremely high electrical conductivity (2000 S/cm). Moreover, the high surface area (theoretically 2630 $m^2 g^{-1}$) contributes to more contact area or loading space for active materials. That means we can use less amount of graphene to achieve the same level of electrical conductivity compared to traditional carbon matrixes. The schematic of assembling graphene with other active materials is shown in Figure 1.47, the graphene network provides effective electron-conducting and ion-conducting transport for active materials. It can improve the overall electrical conductivity and Li^+ diffusion rate of composites, and thus improve the electrochemical performance. However, the technologies of making graphene composites materials varies, depending on what the exact graphene we used in composites.

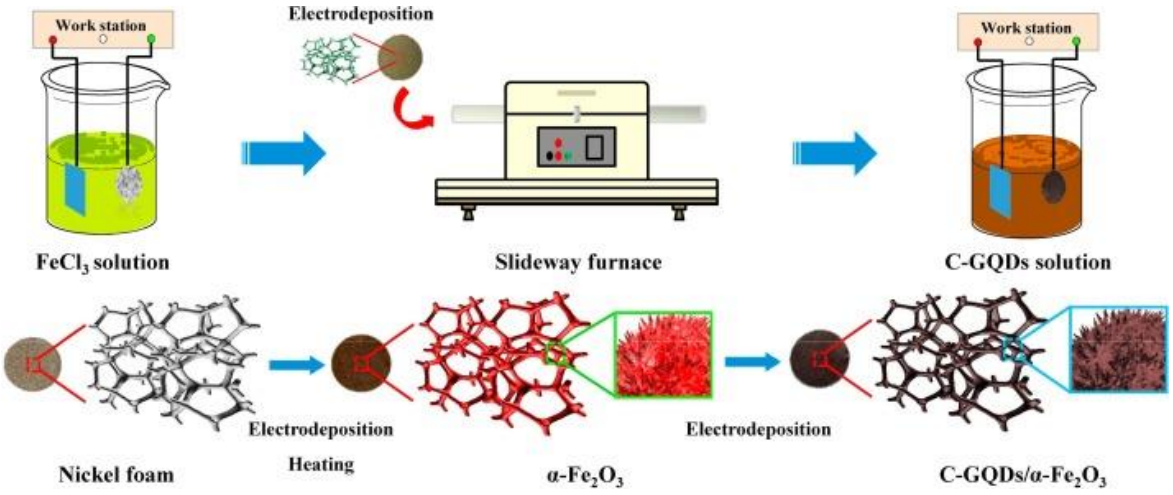

Figure 1.48 Schematic of synthesizing C-QODs/ α-Fe_2O_3 nanocomposites through an electrodeposition approach[174].

0-Dimenssional graphene quantum dots were used by Yating Zhang et al. to make graphene quantum dots/α-Fe_2O_3 through an electrodeposition approach[174]. This 0-D graphene-based composite anode material exhibit good electrochemical performance. The specific capacity can achieve 1582.5 mA h g^{-1} at 1 A/g and can maintain 1320 mA h g^{-1} after 110 cycles. Even at high current density (5 A/g), graphene quantum dots/α-Fe_2O_3 can still possess specific a high capacity of 1091 mA h g^{-1}. This enhanced rate performance owes to the highly conducting graphene quantum dots which provide an effective conductive network of Fe_2O_3 (Figure 1.48).

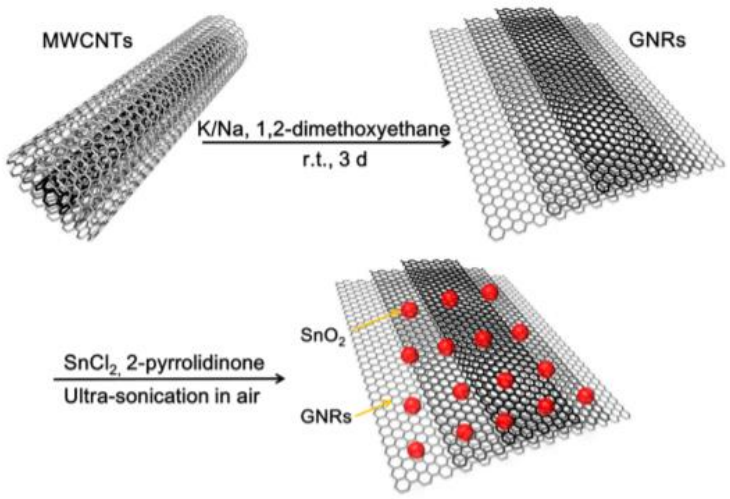

Figure 1.49 Scheme for the synthesis of the GNRs/SnO2 composite[175].

1-D graphene nanoribbons (GNR) and nanorods are also assembled with active materials as either anode or cathode of lithium ion batteries. Jian Lin et al. unzipped multiwall carbon nanotubes to get the graphene nanoribbons and intercalate Sn into graphene nanoribbons stacks to form SnO_2/GNR composites[175] (Figure 1.49). The reversible capacity retains ~825 mAh/g at a current density of 100 mA/g with a Coulombic efficiency of 98% after 50 cycles. Lei Li et al. also used graphene nanoribbons as conductive network to form MnO_2-GNR composite anode, which exhibits specific capacity of 612 mAh/g at 0.4 A/g even after 250 cycles[176]. GNR/V_2O_5 was synthesized by Yang Yang et al. through a intercalation of VCl_4 with concomitant reduction by Na/K[177] (Figure 1.50). This composite was used as a cathode material of LIBs and delivers a high capacity of 278 mAh g^{-1} at 0.1 C.

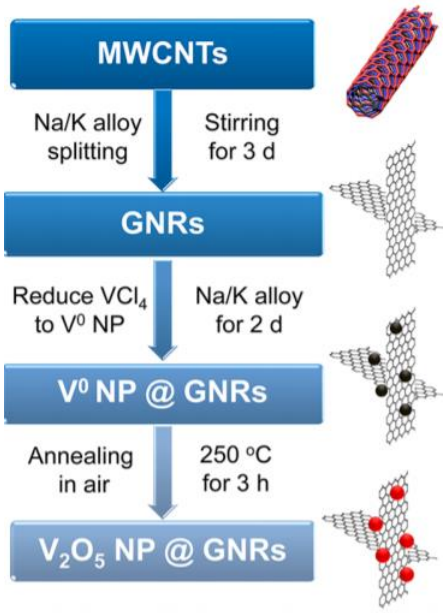

Figure 1.50 Schematic diagram of the fabrication process of GNR-V_2O_5 nanoparticles composites.[177]

2-D graphene is one of the most common materials to make composite electrodes for LIBs. Many active electrode materials such as $LiFePO_4$ have low electrical conductivity which limits their rate performance. Generally, LFP/graphene composites were synthesized through co-precipitation or hydrothermal methods[178-181]. In these works, the LFP precursor was firstly mixed with graphene suspension and then the LFP-graphene composites were obtained by post-heat treatment. For example, Li Wang et al. reported a $LiFePO_4$/graphene composites with a discharge capacity of 160.3 mAh g^{-1} at 0.1 C and 81.5 mAh g^{-1} at 10 C, and illustrate the electron and Li^+ transport mechanism inside the composites (Figure 1.51)[180].

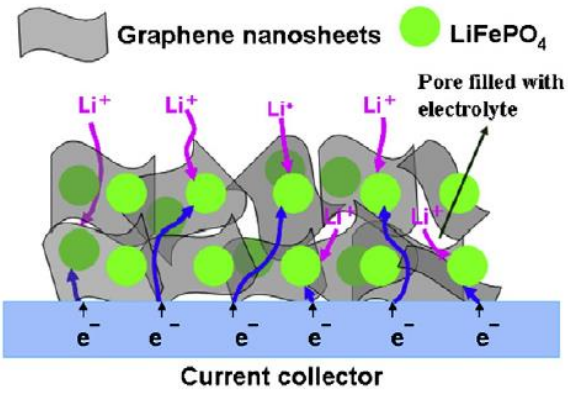

Figure 1.51 Schematic illustration of the structure of the LFPG mixed conducting network[180].

However, graphene suffers from stacking effect: the single-layer or few-layer graphene will spontaneously restack to form aggregates when dispersed in water[182], which severely impact the dispersity of graphene. These restacked graphene sheets and unattached LFP particles were not sufficiently utilized, the stacked graphene sheets only combined in a limited way with LFP[183] (Figure 1.52). Therefore, it is critical to have well-dispersed graphene in nano-composite technology. To solve this problem, researches started to use graphene with functional groups, which has sp3 defects, to improve the dispersity of graphene and apply spray-drying method to tightly anchored the LFP particles to modified-graphene network[184-186]. Nevertheless, such graphene sheets with considerable defects or perhaps graphene oxide have moderate electrical conductivity and cannot effectively improve the rate performance of LFP.

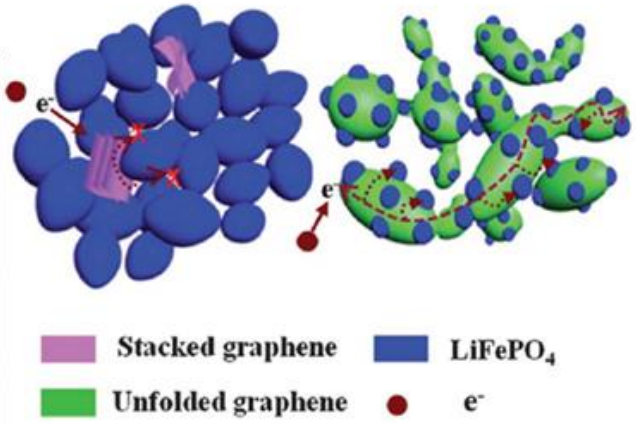

Figure 1.52 Electron-transfer pathway for the LiFePO4–stacked graphene and LiFePO4–unfolded graphene composites[183].

3-D graphene is the third-order structure of the basic single-layer graphene. It can be visualized as the result of folding, twisting or assembling of single-layer or perhaps few-layer graphene. The high-quality 3D graphene was first reported by Huiming Cheng's group. They successfully synthesize three-dimensional foam-like graphene macrostructures by template-directed chemical vapor deposition[115]. Then 3D graphene was brought into the fabrication of composites electrode, which providing more possibilities to produce free-standing electrodes. For example, Dong Ji et al. synthesize MOF-derived CuO wrapped 3D graphene composites as a anode for LIBs[187]. In this design, Cu-based MOF crystals were first uniformly grown on the surface of 3DGN substrate through a solution immersion method and then a subsequent thermal treatment isolated the formation of well-dispersed nanostructured CuO octahedral wrapped 3DGN.

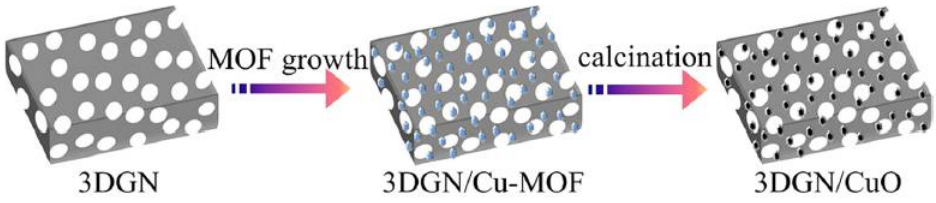

Figure 1.53 Schematic of making 3DGN/CuO[187].

Chapter 2 objective of this dissertation

The objective of this dissertation is to develop novel carbon-based composite materials to solve the current challenges for lithium ion batteries and optimize the composite nanotechnology of both direct assembly approach and bottom-up growth approach by fabricating structural engineered graphene and seeking new type of catalyst for CVD, respectively.

To first tackle the paradox between the dispersibility and conductivity of graphene to produce composite electrodes for LIBs, we aim to synthesize edge-functionalized graphene that can possess both high conductivity and dispersibility. Such edge-functionalized graphene can be further composite with $LiFePO_4$ as an example of its applications in LIBs. The electrochemical performance of this graphene/$LiFePO_4$ composite cathode is worth to be investigated.

On the top of that, to improve the power density of graphite anode, we aim to design a graphite-CNT-graphite sandwich architecture to expand the lithium ion diffusion path and create additional Li^+ reservoirs to push the limits of high-rate performance of graphite anodes.

Last but not least, copper vapour are used as the catalyst to synthesize graphene on non-catalytic substrate through CVD process. With the ability to grow graphene on such substrates, it will broad the bottom-up approaches to fabricate graphene-based composite materials using chemical vapour deposition.

Chapter 3 High-Conductivity-Dispersibility Graphene Made by Catalytic Exfoliation of Graphite for Lithium-Ion Battery

3.1 Introduction

Owning to excellent electron conductivity (2000 S cm^{-1})[1], high surface area (2630 m^2 g^{-1}) [2] and high ambipolar charge-carrier mobility (10^5 cm^2 V^{-1} s^{-1})[3], graphene has been extensively explored for a broad range of applications such as energy storage[64-66], polymer composites[67, 68] and photoelectric devices[69, 70]. Graphene is generally synthesized through a bottom-up or top-down strategy, of which the former approach converts carbon precursors to graphene through a specific process such as chemical vapor deposition[188, 189] and epitaxial growth[190], while the latter approach exfoliates graphite to graphene through a chemical or mechanical route. The former approaches enable the synthesis graphene with high quality but with low yield and high cost; while the latter approaches enable the scale synthesis of graphene at low cost but with low quality[118].

In the context of using graphene as conductive agent for lithium-ion batteries, it is essential to synthesize graphene with high conductivity and dispersibility. The electrical conductivity of graphene is generally associated with the structural integrity; large-lateral-size graphene with less defects offers better conductivity. Dispersibility of graphene, in contrast, is associated with the degree of functionalization; small-lateral-size graphene with a high degree of functionalization (e.g., oxidation) leads to better dispersibility but with reduced electrical conductivity. Despite the extensive efforts made, making graphene with both high conductivity and dispersibility remains challenging.

We envision that both high conductivity and dispersibility could be achieved in edge-functionalized graphene with large lateral size, such that the functional groups in the edge and

well-retained graphene structure in the basal plane can provide dispersibility and conductivity, respectively. Such edge-functionalized graphene can be readily synthesized using an edge-to-interior exfoliation strategy. The edge of graphite flake is first oxidized using a mixture of sulfuric acid and potassium permanganate ($KMnO_4/H_2SO_4$); as resulted edge-oxidized graphite flakes (denoted as eo-GF) is then intercalated with iron chloride ($FeCl_3$), a highly effective catalyst for the decomposition reaction of hydrogen peroxide (H_2O_2) to water and oxygen (O_2). Immersing the $FeCl_3$-intercalating graphite to H_2O_2 generates O_2 and exfoliates the graphite from the edge region, gradually exposing the intercalated catalyst to H_2O_2 and enabling further exfoliation from the edge towards the interior. This catalytic exfoliation method enables scale synthesis of edge-oxidized graphene with large lateral size, denoted hereinafter as eoG with both high conductivity and dispersibility.

Previously, large-lateral-size graphene was synthesized through chemical reduction of graphene oxide followed by a chemical reduction process. Large-lateral-size graphene oxide was first synthesized by physical exfoliation of graphite oxide using ultrasonication or by a chemical exfoliation technique. The chemical exfoliation involved intercalating graphite with a concentrated oxidant (e.g., concentrated K_2FeO_4/H_2SO_4), which reacted and generated O_2 within the graphite layers, exfoliating the graphite that was oxidized to graphene oxide. Using these approaches, large-lateral-size graphene oxides were synthesized; however, it is generally difficult to preserve the conductivity despite the subsequent chemical reduction process. To preserve the conductivity of graphene, non-oxidant compounds were also intercalated to graphite, such as $FeCl_3$[191, 192] and ammonium bicarbonate[193], which facilitated the exfoliation that was assisted by sonication and microwave radiation, respectively. However, both the approaches resulted in small-lateral-size graphene (~ 0.6 μm) with poor dispersibility due to the lack of functionalization of the

graphene. Highly concentrated H_2SO_4 was also intercalated to graphite to facilitate the exfoliation in an anodic oxidation process[194]; the use of strong oxidant, however, resulted in graphene oxide with small lateral size (1-2 μm) and low conductivity (~300 Ohms sq^{-1}). We also note that H_2O_2 was used previously to exfoliate graphene oxide in the presence of Mn^{3+} ions, which resulted in partially oxidized few-layer graphene with small lateral size (~5 μm) and low sheet resistance (119.6 Ohms sq^{-1})[117]. Compared with the current state of arts, our strategy is based on controlled catalytic exfoliation of edge-oxidized graphite avoiding the use of strong oxidant, which enables a scalable synthesis of large-lateral-size graphene with high conductivity and dispersibility in a spontaneous exfoliation process without using external energy field (e.g., sonication and microwave radiation).

3.2 Experimental

Synthesis of edge oxidized graphite. Graphite flake (2 g, Sigma-Aldrich) was added to concentrated H_2SO_4 (40 mL) under 20℃ in the ice-bath and the mixture was kept stirring for 30 min. $KMnO_4$ (2 g, Sigma-Aldrich) was then slowly added within 30 min, the mixture was kept in the ice-bath for 2 h. After that, deionized water was added and furtherly kept stirring for 2 hours. H_2O_2 (2mL) was then added to stop the reaction. The mixture was filtered and washed by deionized water for 3 times. Edge oxidized graphite was obtained by freeze-drying for 24h.

Synthesis of $FeCl_3$-eoGIC. $FeCl_3$ (0.32g, Alfa Aesar) was fully mixed with the obtained edge oxidized graphite (0.08g). Then the mixture was sealed in a stainless-steel autoclave and was heated to 600℃ for 6h. After cooling down, $FeCl_3$-eoGIC was obtained.

Synthesis of edge oxidized graphene (eoG). 0.8g $FeCl_3$-eoGIC was poured into hydrogen peroxide solution (H_2O_2/H_2O=1:1) for 3 min to finish the bubbling exfoliation. After the ultrasonic treatment for 5 min, the obtained eoG was washed by DI water for 3 times. Then the eoG was filtered and freeze dried.

Material characterization. Powder X-ray diffraction (XRD) was determined by using a Rigaku Miniflex II diffractometer with Cu Kα radiation. The morphology, crystalline phase, and composition of the as-synthesized products were obtained on field-emission scanning electron microscopy (FESEM,FEI Nova 430), transmission electron microscopy, high-resolution transmission electron microscopy (HRTEM, FEI Titan STEM), and atomic force microscopy (Bruker Dimension Icon Scanning Probe Microscope). XPS analysis was performed using an

ESCALAB 250Xi spectrometer by a mono Al Kα radiation. Raman spectroscopy was measured with Renishaw 2000 System. AFM images of eoG were taken using Bruker Dimension Icon Scanning Probe Microscope. Thermogravimetric analysis was characterized using Netzsch STA 449 F3 Jupiter. Electrical conductivity and sheet resistance were measured using Signatone Pro4 combined with a source meter (Keithley 2400).

3.3 Results and discussion

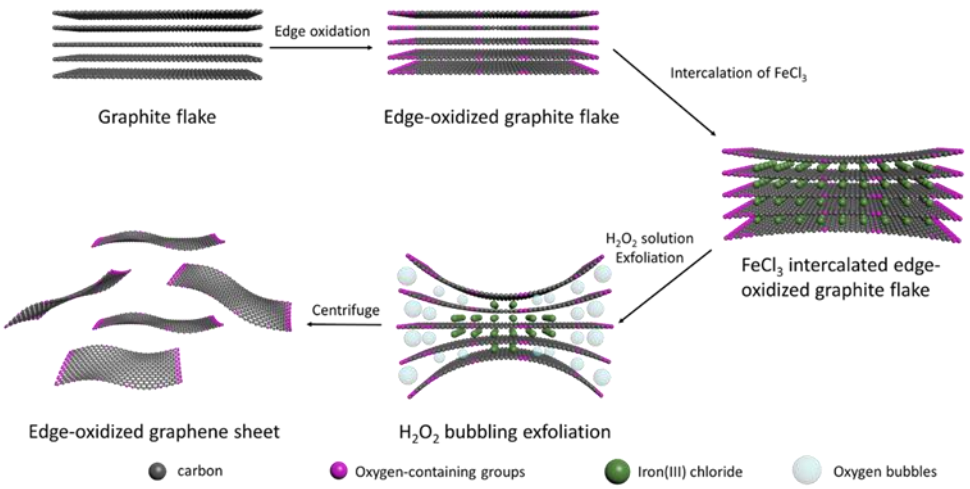

Figure 3.1 A schematic illustrating the synthesis of edge-oxidized graphene with high dispersibility and conductivity using a catalytic exfoliation strategy.

The preparation process of the edge oxidized graphene (eoG) is shown on Figure 3.1. The graphite flakes were firstly partially oxidized by mixing with potassium permanganate and concentrated sulfuric acid for 2 hours. Hydrogen peroxide was used to stop the oxidation process. Since the edge of graphite flake are more active during oxidation process, these edge parts are

prior to be oxidized[117]. The edge oxidized graphite flake (eo-GF) was adequately mixed with ferric chloride and sealed in a stainless-steel autoclave. Then it was heated to 600℃ for 6h. At 600℃in closed system, $FeCl_3$ vapor intercalated into eo-GF interlayers under 1.35 Mpa. Since edge oxidation process were able to open the edge of graphite flakes, it was easier to have a fully intercalation for eo-GF. $FeCl_3$-edge oxidized Graphite Intercalation Compound ($FeCl_3$-eoGIC) was then immersed in 1:1 H_2O_2 aqueous solution. The violent reaction between Fe^{2+}, Fe^{3+}, Mn^{3+} and H_2O_2 generated considerable amount of oxygen bubbles which contribute to peel off graphene sheets from edge to center. Finally, the obtained eoG was collected by proceeding ultrasonic treatment and centrifugation.

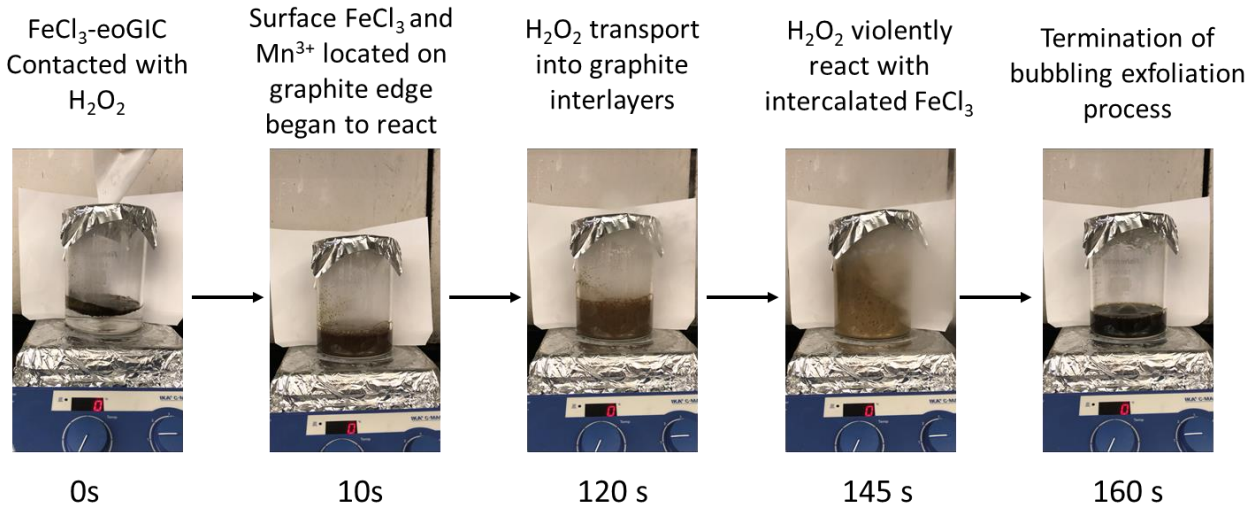

Figure 3.2 Bubbling exfoliation process of edge-oxidized graphite in 200 mL solution of 15wt% H2O2.

In this process, the instantaneous exfoliation process only takes 160s and does not generate environmentally hazardous waste, which is promising to scale up this process to mass production. It is noted that the design of edge oxidized structure has several advanced meanings: the edge of

the graphite interlayers was partly oxidized and opened by $KMnO_4$ and H_2SO_4, which make it easier for the intercalation of $FeCl_3$; Mn ions located in the edge worked like beer opener to trigger the exfoliation while reacting with H_2O_2; The edge-distributed oxygen containing group increase the water solubilities of eoG as well as keeping completeness of sp^2 domain on the basal plane of eoG nanosheets.

The scanning electron microscope (SEM) images of graphite, eo-Graphite and eoG in Figure 3.3 further reveal the structural changes of graphite flake after intercalation and exfoliation. As shown on Figure 3.3a, pristine graphite flake exhibits compact and ordered interlayers architectures. After edge oxidization and $FeCl_3$ intercalation, the interlayer spacing of graphite flake was enlarged according to Figure 3.3b, which is well-corresponding to XRD results. It is clear that the Van der Waals force between graphene sheets was weakened by intercalated $FeCl_3$, this $FeCl_3$-graphene-$FeCl_3$ sandwich structure ensure a layer-by-layer exfoliation while $FeCl_3$ reacting with H_2O_2. After the H_2O_2 bubbling exfoliation process, few-layer eoG sheets were obtained (Figure 3.3c).

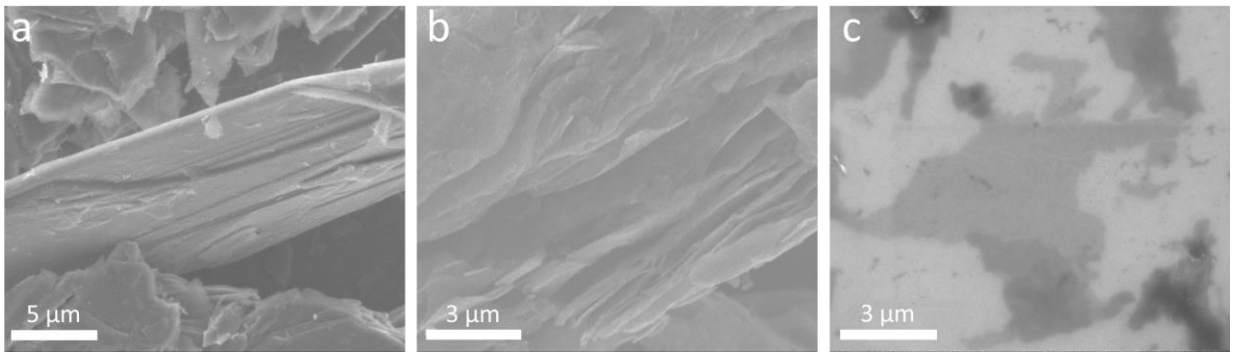

Figure 3.3 Scanning electron microscope (SEM) images of **a** cross-section structure of graphite flake, **b** interlayer structure of FeCl3-Graphite intercalation compounds ($FeCl_3$-GICs) and **c** edge-oxidized graphene (eoG) sheets.

Figure 3.4a shows x-ray diffraction (XRD) pattern of pristine graphite flake, edge-oxidized graphite before and after intercalation of $FeCl_3$, and eoG. The pristine graphite shows a typical pattern with (002) and (004) reflections at two-theta 26.5° and 54.7°, respectively, corresponding an interlayer spacing of 3.35 Å. The eo-GF shows a pattern with the (001) and (002) reflection at two-theta 12.8° and 26.5°, respectively, corresponding to a slightly increased interlayer spacing of 6.77 Å of the edge plane and a retained interlayer spacing of 3.35 Å of the basal plane. Compared with graphene oxide, which generally shows a (001) peak at two theta 10.3° or interlayer spacing of 8.60 Å[195], the eo-GF shows a smaller interlayer spacing, indicating an partially oxidized structure. The $FeCl_3$-intercalated graphite shows the characteristic diffractions of $FeCl_3$ at 9.4°, 18.8°, 28.3°, 35.3° and 50.5°, which are corresponding to 1(001), 1(002), 1(003), 1(005), and 1(006) reflections (the c-axis of (00L) of standard pattern stage-1 $FeCl_3$-GICs), respectively[191, 196, 197]. After exfoliation, eoG shows a broadened (002) peak and the intensity of (002) peak significantly decrease compared with graphite flake (Figure 3.4b), indicating that the edge-oxidized graphite was successfully exfoliated into thin-layer graphene.

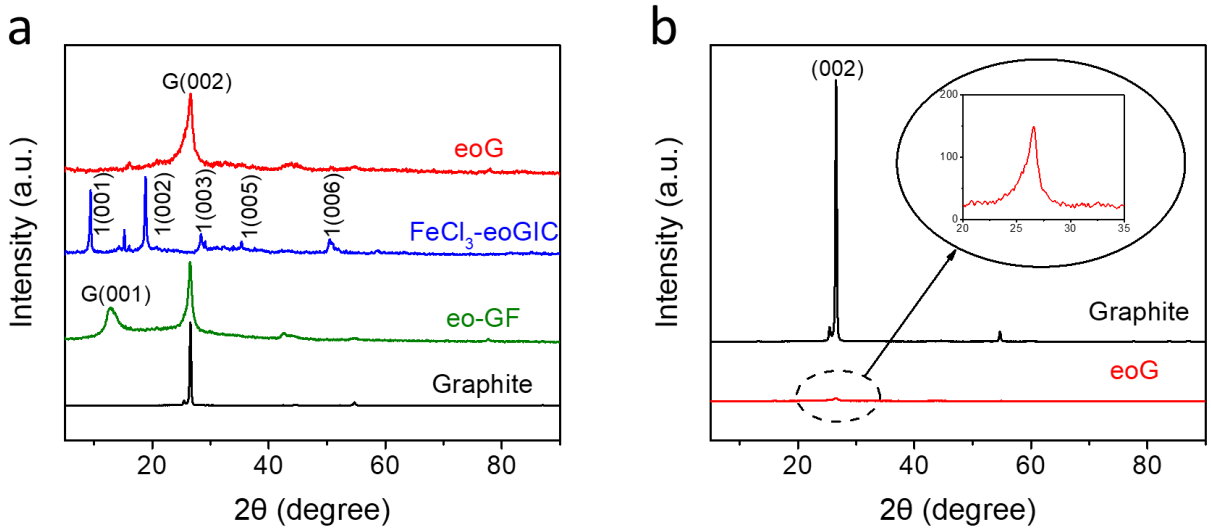

Figure 3.4 a XRD patterns of eoG, FeCl3-eoGIC, edge-oxidized graphite and pristine graphite flake with normalized intensity. **b** XRD patterns of eoG compared with graphite flake.

Interestingly, the (001) peak of eo-GF disappeared in the XRD pattern of eoG after exfoliation. FeCl3 intercalation and H2O2 bubbling exfoliation process does not have a reduction effect on eo-GF, thus it is not the reason for the disappearance of (001) peak of eoG. It is illustrated in Figure 3.5 to explain the phenomena where θ_1 is the Bragg angle of the (002) peak of basal plane of graphene, while θ_2 is the Bragg angle of the (001) peak of edge plane of graphene. Since X-ray has a limited penetration depth, the incident wave can only achieve part of the basal plane exposed on the surface due to a stacked structure of eo-GF. However, after exfoliation more basal planes were exposed to the incident wave and the intensity ratio of $I_{(002)}/I_{(001)}$ increased significantly, leading to the disappearance of (001) peak at $2\theta_2=12.8°$ of eoG.

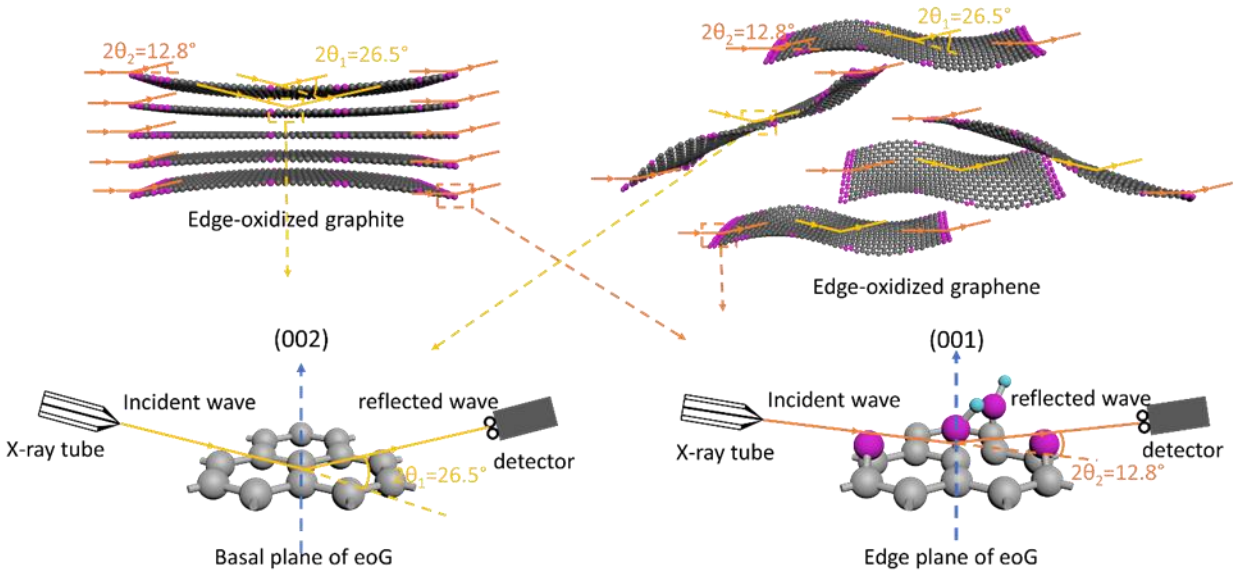

Figure 3.5 Schematic of XRD testing of eo-GF and eoG.

Figure 3.6 shows Raman spectra of eoG exhibiting a typical D band at 1333 cm^{-1}, G band at 1582 cm^{-1} and 2D band at 2666-2685 cm^{-1}. The ratio of D-band intensity over G-band intensity (I_D/I_G) is a key indicator for the degree of oxidization and defects. For such large-lateral-size eoG, spectra were collected from the edge and central locations with I_D/I_G at 0.90 and 0.21, respectively, confirming an edge-oxidized structure. The I_D/I_G value of eoG at the basal plane is similar to that of pristine graphite (I_D/I_G~0.13), confirming the preservation of the graphene structure at the basal plane.

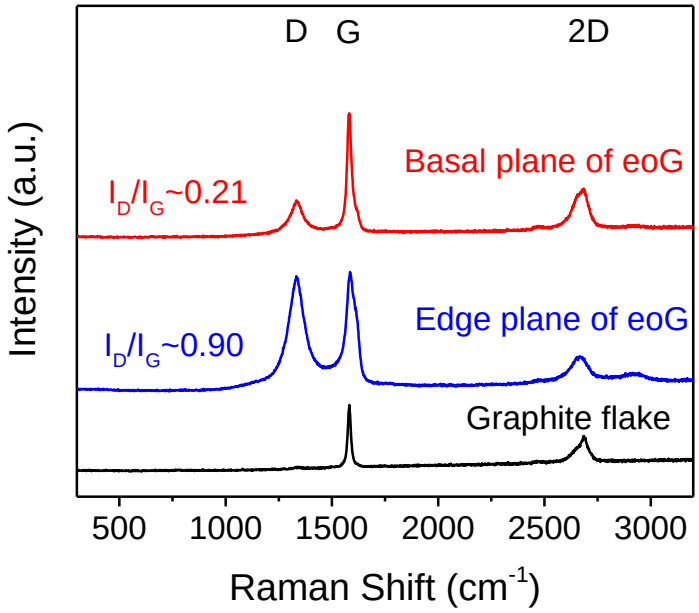

Figure 3.6 Raman spectra of eoG and pristine graphite flake.

Figure 3.7a shows x-ray photoelectron spectroscopy (XPS) spectrum of eo-GF and eoG, exhibiting a typical C1s peak at 284.5 eV and O1s peak at 531.5 eV. The eoG exhibits a larger carbon-to-oxygen ratio (C/O~11) than edge oxidized graphite (C/O~3). This can be explained by

the same reason of XRD results and furtherly confirmed that the oxygen-containing defects are mainly located on the edge plane of eoG. The C1s peak can be deconvoluted into three components, sp2-C (C=C at 284.5 eV), sp3-C (C-C at 284.8 eV) and carbon with epoxy or hydroxyl form (C-O at 285.9 eV) (Figure 3.7b). The domination of sp^2-C structure confirms the formation of eoG with well-preserved graphene structure.

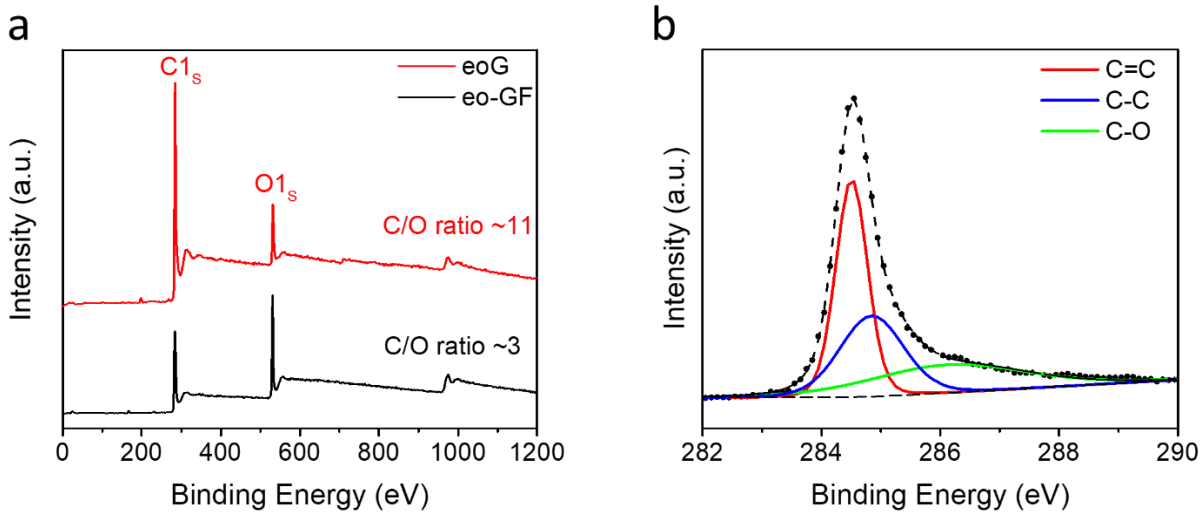

Figure 3.7 a XPS survey spectra of edge-oxidized graphene (eoG) and edge-oxidized graphite flake (eo-GF). **b** C 1s spectra of XPS and deconvoluted peaks of the eoG.

The structure of eoG was further characterized using transmission electron microscopy (TEM), As shown in Figure 3.8a, eoG sheets show a wrinkle structure implying ultrathin nature and good flexibility. High resolution TEM and selected area electron diffraction pattern (SAED) were conducted on both the basal plane and edge plane of eoG. To study the crystallinity of eoG, we first select a basal plane region (the top red mark in Figure 3.8a) to zoom in. Figure 3.8b shows the High-resolution TEM image of the eoG basal plane. The basal plane possesses distinct

crystallinity with a lattice spacing of 0.34 nm, which is similar to that of the (002) plane of graphene. Surprisingly, the SAED pattern shown in Figure 3.8c reveals a single-crystalline structure with (100) and (002) plane, which confirms the completeness of sp^2 domain in eoG basal plane. Then, when we move to the edge plane of eoG (Figure 3.8d), the lattice spacing in edge plane is expanded to 0.44 nm, which is consistent with the edge-oxidized structure that contains oxygen-containing functional groups on the edge plane. Consistently, SAED shows a polycrystalline structure at the edge plane, indicating a disrupted structure.

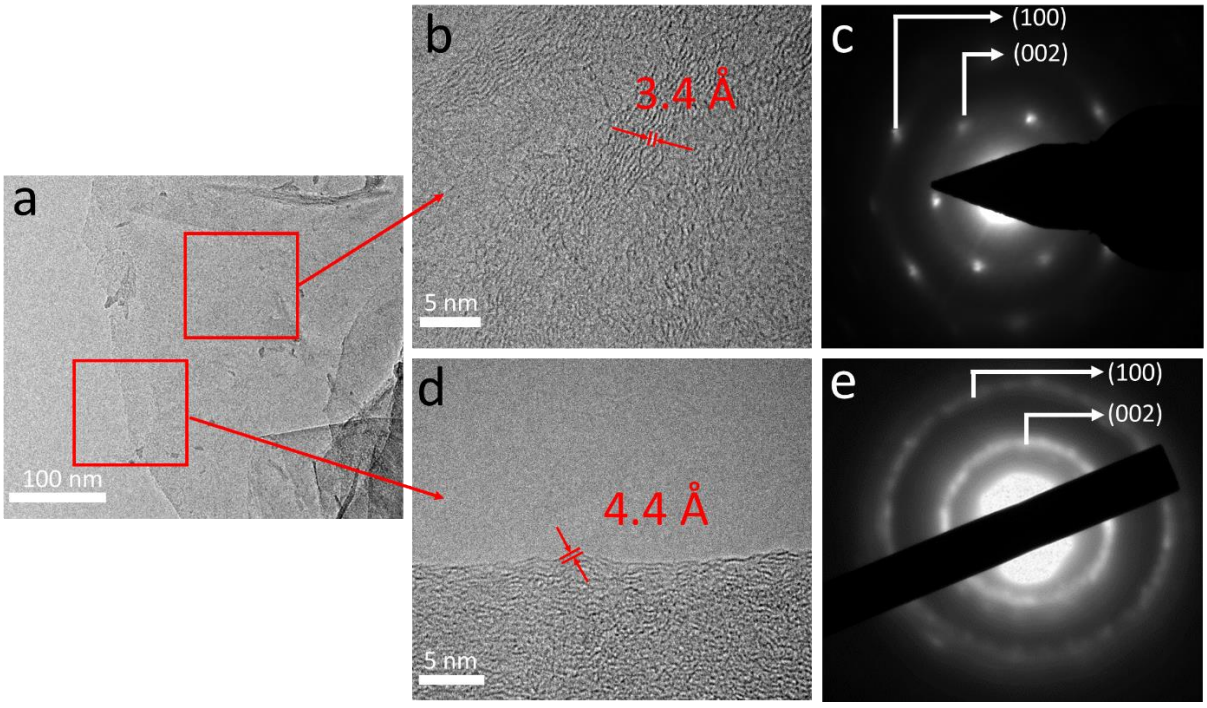

Figure 3.8 a TEM images of eoG sheets. b High-resolution TEM images of the basal plane of eoG

Figure 3.9 a-b shows the SEM images of eoG with a considerable lateral size. The abundance of wrinkles was also convinced by SEM images. After we counted and calculated the size distribution of the eoG sheets from Figure 3.9 a and b, it is found that the number-average width

of eoG sheets is 9~10 μm (Figure 3.9 c) which is consistent with the observation from atomic force microscope (AFM) image.

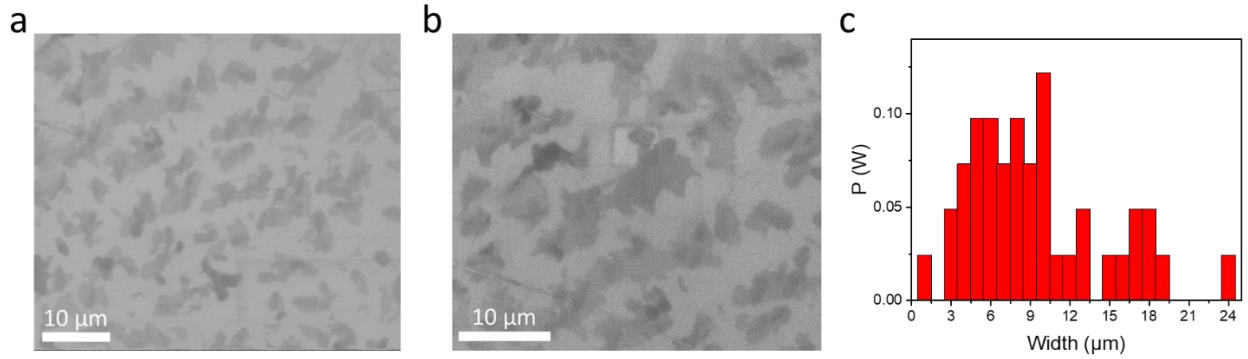

Figure 3.9 a, **b** SEM images of the eoG sheets. c The size distribution of the eoG sheets, counted and calculated from **a** and **b.**

Figure 3.10 presents the AFM images of eoG. As we can see from the height profile, the eoG have a thickness less than 3 nm. Moreover, the eoG sheets shown in Figure 3.10 a and b have a width of 13.5 μm and 11.3 μm, respectively. Together, it confirms large-lateral-size and few-layer (3-7 layers) structure of the eoG.

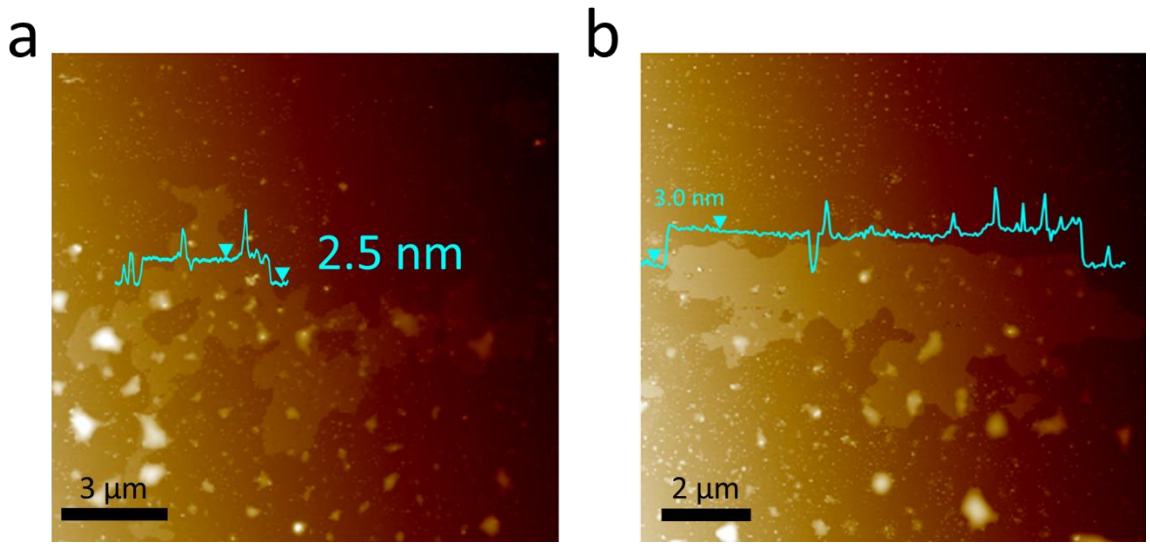

Figure 3.10 a, b AFM image and height profile of the eoG.

Such large-lateral-size eoG with well-preserved graphene structure exhibits high electrical conductivity of 924 S cm^{-1} and excellent water solubility, which remains stable for one month at concentration of 10 mg ml^{-1}. To measure the electrical conductivity of eoG, we press the dry eoG sheets on the insulated paper substrate to form a graphene film with 9 µm thickness. Figure 3.11 a shows the equipment (Signatone Pro4) that was used to measure the sheet resistance and electrical conductivity. The eoG film exhibits a average sheet resistance of 1.2 Ω cm^{-2} and an average electrical conductivity of 924 S cm^{-1}. The eoG sheets were then dispersed in 350 mL water in a concentration of 10 mg mL^{-1}. As shown in Figure 3.12, the eoG aqueous dispersion (10 mg mL^{-1}) can be stable up to 1 month, while the graphite flake aqueous dispersion (10 mg mL^{-1}) started to precipitate within 24 hours and the top dispersion become completely clear after one month.

a

b

Pro4 Test Results

Date: 2019-12-09 02:46
Wafer ID: pro4
Wafer Lot: Test
Wafer Shape: Square
Wafer Size (mm): 120
Edge Exclusion (mm): 20
Number of Points: 5
Current used (mA): 11.25

	Avg	Std Dev	1-Sigma	Min	Max
Rs (Ohm/sq)	1.202157	0.151999	12.64386	0.9127179	1.313442
Res (Ohm-cm)	0.001081941	0.0001367991	12.64386	0.0008214461	0.001163705
Thk (um)	9	0	0	9	9
V/I	0.4657072	0.05869351	12.60309	0.3534539	0.5078106

Point	X (mm)	Y (mm)	Rs (Ohm/sq)	Res (Ohm-cm)	V/I	Thk (um)
1	0.0	0.0	1.293006	0.001163705	0.5024161	9
2	40.0	-40.0	1.306203	0.001175582	0.5041584	9
3	-40.0	-40.0	1.313442	0.001182097	0.5078106	9
4	-40.0	40.0	1.185416	0.001066875	0.4606972	9
5	40.0	40.0	0.9127179	0.0008214461	0.3534539	9

Figure 3.11 a The image of 4-probe test equipment (Signatone) that used to measure the electronic conductivity of eoG. **b** The 4-prob test results of eoG for selecting 5 different points.

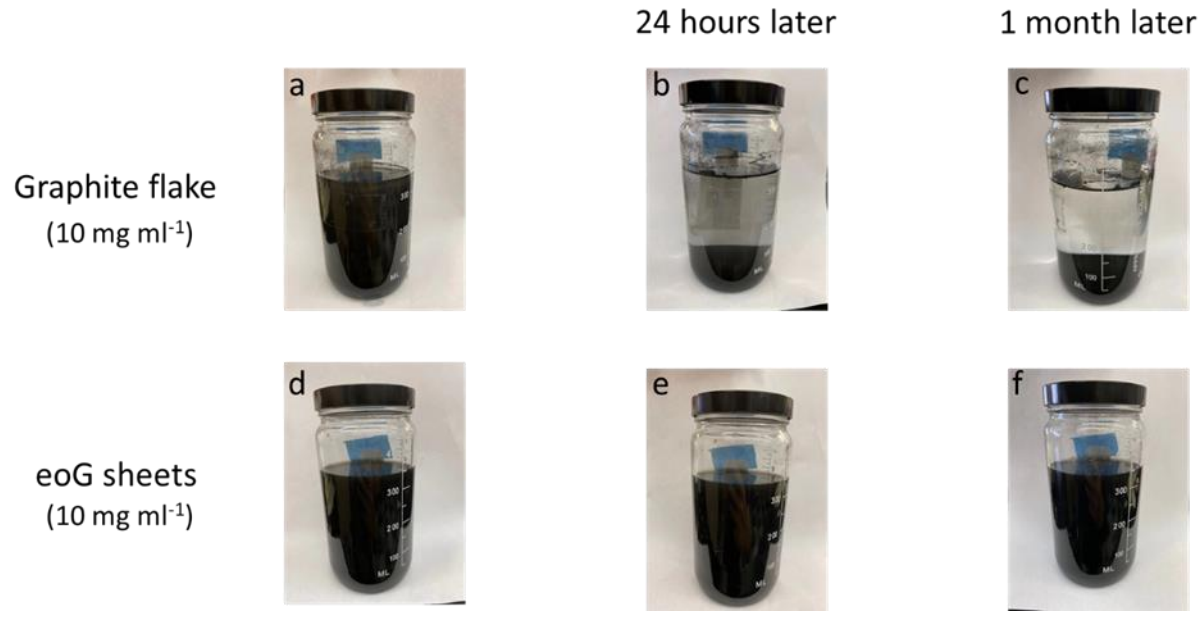

Figure 3.12 Dispersibility of graphite flake and eoG in water. **(**a-c) Digital photograph of graphite flake dispersed in 350 mL water with concentration of 10 mg mL^{-1}, for 0 hours, 24 hours and 1 month. (d-f) Digital photograph of eoG dispersed in 350 mLwater with concentration of 10 mg mL^{-1}, for 0 hours, 24 hours and 1 month. This good water solubility of eoG is caused by the strong interaction between oxygen containing groups located in the edge plane of eoG and H_2O molecule.

Figure 3.13 compares the lateral size, water solubility and electronic conductivity of reported graphene made by liquid phase exfoliation (also see the Supplementary Table 3.1). Such graphene based materials, including graphene oxide(GO), reduced graphene oxide (rGO) and pristine graphene, were made through a reduction of large-scale GO (e.g. Ag-reduced rGO[198]) or an exfoliation of graphite intercalation compound (e.g. imidazole[199], chlorosulphonic acid[200], or FeO_4^{2-} intercalated graphite[201]) followed by sonication. However, eoG have larger lateral size, higher electronic conductivity and better water dispersibility than other modified graphene materials and even pristine graphene which is previously reported[198, 199, 201-207].

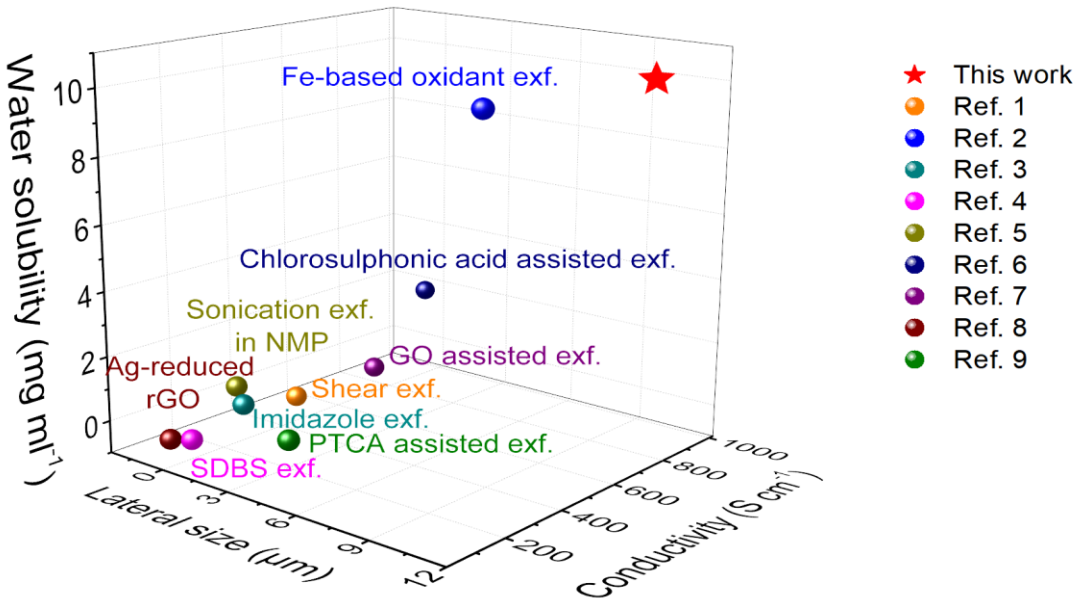

Figure 3.13 A comparison of the lateral size, electronic conductivity and water solubility of eoG with other graphene materials reported.

Table 3.1 A comparison of graphene attributes of our approach and current state of art of liquid phase exfoliation methods[198, 199, 201-207].

Reference	Product	Mehod	I_D/I_G	Lateral Size (μm)	Electronic conductivity (S cm^{-1})	Water solubility (mg ml^{-1})
Ref. 1	graphene	shear exfoliation	0.17	0.7	400	0.1
Ref. 2	GO	Fe-based oxidant exfoliation	0.93	9	372	10
Ref. 3	graphene	imidazole assisted exfoliation	0.25	2	131.7	1
Ref. 4	graphene	SDBS assisted exfoliation	0.34	1	35	0.05
Ref. 5	graphene	sonification-assisted exfoliation in NMP	0.37	1	180	1.2
Ref. 6	Graphene	spontaneous exfoliation in chlorosulphonic acid	N/A	0.25	920	2
Ref. 7	GO-graphene	GO assisted exfoliation	0.12	1.5	620	0.5
Ref. 8	rGO	Ag-reduced rGO	0.8	0.45	5.19	0.05
Ref. 9	graphene	Perylene trtracarboxylate surfactant assisted exfoliation	0.36	5	60	0.8
This work	eoG	$FeCl_3$ intercalating and H_2O_2 bubbling exfoliation	0.23	10	924	10

Except for the excellent water dispersibility, such edge-oxidized structure also enables good solubility in organic solvent. Therefore, we can adapt an extraction separation method to isolate

the eoG directly after exfoliation process by using organic solvent such as toluene[208] and ethyl acetate[209].

After adding organic solvent and vibration, eoG sheets transferred from water phase into organic solvent phase in less than 10 second, while with iron chloride left in the water phase (Figure 3.14). The water phase is then removed from bottom and organic solvent was evaporated leaving high-quality eoG in the funnel. This separation method is suitable for large scale separation.

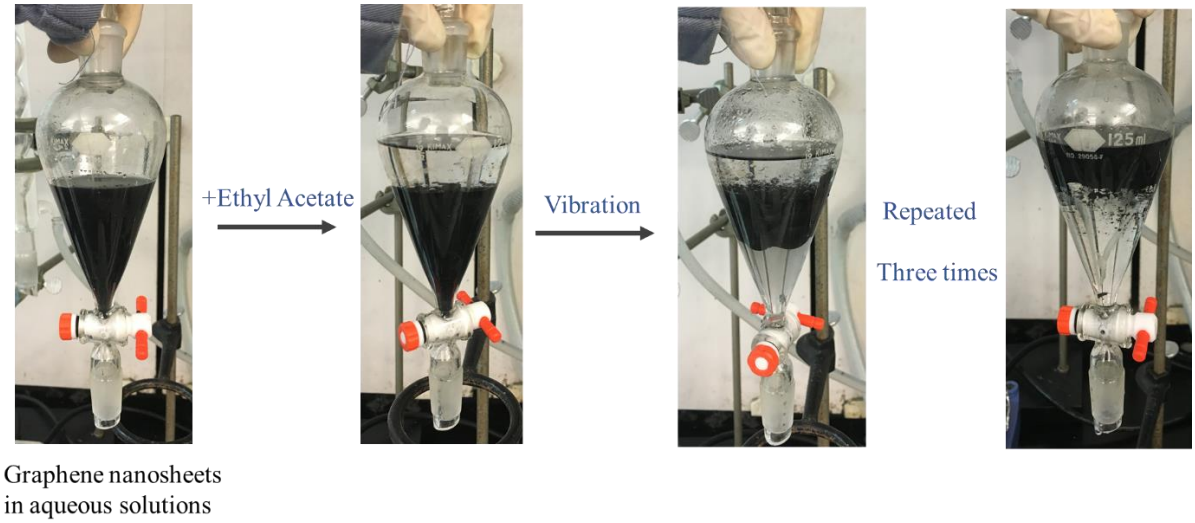

Figure 3.14 photograph of extraction process to separate graphene nanosheets by using ethyl acetate as solvent

3.4 conclusion

In conclusion, we designed large-lateral-size and high-quality graphene with excellent water solubility through $FeCl_3$ intercalation and H_2O_2 bubbling exfoliation paths. This rapid (3 minutes) and potentially scalable method obtained eoG which has excellent structural integrity (basal plane I_D/I_G~0.23, bulk C/O~11), edge-oxidized functional structure (edge plane I_D/I_G~0.97), few-layer thickness (~3-7 layers) and large lateral size (~10 μm). The excellent water dispersity (10 mg mL^{-1} for one month) make eoG a competitive 2D graphene materials to make composite materials. Furthermore, the excellent organic solvent dispersity enables a simple extraction method to separate the eoG without a loss and restacking problems.

Chapter 4 Large-scale and edge-oxidized graphene modified $LiFePO_4$ cathode for high power lithium ion batteries

4.1 Introduction

Lithium-ion batteries (LIBs) have been one of the best roles among energy storage devices due to their long lifespan, high energy density, and relatively light weights[210-212]. In the past decades, LIBs have been revolutionary in the development of Hybrid-electric vehicles (HEV), Plug-in hybrid-electric vehicles and Electric Vehicles (EV)[213-215], bringing automobiles into a new era. Nowadays, it is urgently demanded to improve the energy density, power density and battery safety of LIBs in this field[216-220]. Since the seminal work of Goodenough and co-workers[221], the phospho-olivine $LiFePO_4$ (LFP) have been considered as one of the most promising cathode materials for EVs due to its high open-circuit voltage (3.45 V vs. Li^+/Li), high theoretical capacity (~170 mAh g^{-1}), low cost, environmentally benign and safety[222, 223]. However, $LiFePO_4$ suffers from low electronic conductivity (10^{-9} to 10^{-10} S cm^{-1})[224], poor lithium-ion diffusion coefficient (10^{-14} to 10^{-16} cm^2 s^{-1})[225] and low tap density[222], thus limited charge-discharge rates and volumetric energy density.

To tackle above challenges, graphene which possesses high electron conductivity (2000 S cm^{-1}) [1], ultrahigh surface area (2630 m^2 g^{-1}) [2], high carrier mobility at room temperature (~10000 cm^2 V^{-1} s^{-1})[50] and excellent mechanical strength provides a matrix or substrate for active materials to increase the electronic and ionic conductivity, stable the structure during discharge-charge cycles and thereby improve electrochemical performance. Nevertheless, graphene suffers from stacking effect: the single-layer or few-layer graphene will spontaneously restack to form aggregates when dispersed in water[3, 182], which severely impacts the dispersity of graphene.

In the early researches toward graphene-modified LFP, people fabricated LFP-graphene composite by using co-precipitation and hydrothermal methods[178-181]. In these works, the LFP precursor was firstly mixed with graphene suspension and then the LFP-graphene composites were obtained by post-heat treatment. However, the restacked graphene sheets and unattached LFP particles were not sufficiently utilized, the stacked graphene sheets only combined in a limited way with LFP[183]. Therefore, it is critical to have well-dispersed graphene in nano-composite technology. To solve this problem, researches started to use graphene with functional groups, which has sp^3 defects, to improve the dispersity of graphene and apply the spray-drying method to tightly anchored the LFP particles to modified-graphene network[184-186]. It must be pointed out that these induced sp^3 defects on graphene lower the electronic and ionic conductivity which impact the electrochemical performance of composite electrode materials. Researchers also use the ratio of sp^2/sp^3 to evaluate the quality of graphene[226, 227]. As a result, we need to strike a balance between the sp^2 content (higher electronic and ionic conductivity) and the sp^3 content (better dispersity). Engineered graphene which sets sp^3 defects in the edge plane while retains the completeness of the sp^2 domain in the basal plane is needed to solve this contradictory.

The lateral size of graphene is another important issue that can impact graphene-based composite materials. On the one hand, large-lateral-size graphene has more ordered stack behavior in the composite fabrication process. It improves the long-range conductivity of graphene-based composite materials. However, small-lateral-size graphene tends to compose a disordered pack with active materials, which impedes the transportation of electron and lithium ions. On the other hand, the large-lateral-size graphene with the edge-oxidized structure that we mentioned above will have a higher sp^2 ratio (better conductivity) compared to small-lateral size graphene under the

same weight. Therefore, large-lateral-size and high-quality graphene with edge-oxidized structure can effectively improve the performance of LFP/graphene composite cathode.

Herein, we applied a novel strategy that we discussed in Chapter 4 to produce the high-quality, large-lateral-size and edge-oxidized graphene (eoG) sheets and prepared $LiFePO_4$/eoG (LFP-eoG) composite by spray-drying and annealing process. This engineered graphene improved water solubility and affinity towards $LiFePO_4$ during spray drying, while it retained excellent properties of pristine graphene in electric and ionic conductivity. Once anchored tightly with commercial LFP nanoparticles by using spray-drying method, eoG provides an efficient electron transport pathway for LFP primary nanoparticles. The LFP-eoG composite electrode exhibits low polarization (82 mV at 0.2 C), high electrical conductivity (924 S cm^{-1}), excellent rate capability (76.6 mA h g^{-1} at 20 C) and stable cycle performance (200 cycle with retention rate of 93%). We hope that this work will open the pathway to develop well-designed graphene architecture with high electrical conductivity and good processing capability for composite electrodes materials to tackle the challenges of lithium-ion batteries.

4.2 Experimental

Preparation of LFP-eoG composite cathode materials. The eoG (0.05g) was mixed with commercial $LiFePO_4$ (0.95g) in DI water. After ultrasonication, it formed a homogeneous precursor dispersion. The solution was sprayed in a heated reactor at 220℃ by using air as carrier gas. The obtained LFP-eoG powder was then annealed at 600℃ in argon for 6h.

Material characterization. Powder X-ray diffraction (XRD) was determined by using a Rigaku Miniflex II diffractometer with Cu Kα radiation. The morphology, crystalline phase, and composition of the as-synthesized products were obtained on field-emission scanning electron microscopy (FESEM,FEI Nova 430), transmission electron microscopy, high-resolution transmission electron microscopy (HRTEM, FEI Titan STEM), and atomic force microscopy (Bruker Dimension Icon Scanning Probe Microscope). XPS analysis was performed using an ESCALAB 250Xi spectrometer by a mono Al Kα radiation. Raman spectroscopy was measured with Renishaw 2000 System. AFM images of eoG were taken using Bruker Dimension Icon Scanning Probe Microscope. Thermogravimetric analysis was characterized using Netzsch STA 449 F3 Jupiter.

Electrochemical measurements. The electrodes of LFP-eoG, LFP-GO, and commercial LFP were prepared by slurry-coating method. Active materials (LFP-eoG, LFP-GO, and commercial LFP), super P carbon black, and binder (PVDF) were adequately mixed with a mass ratio of 80:10:10. The mixture were dispersed in N-methyl-2-pyrrolidone forming a slurry, which were afterward coated onto a Al foil. All of the obtained well-dried electrodes were measured to have an areal loading of 1.5 mg cm^{-2}. These electrodes were integrated into CR2032-type coin cells using Lithium metal as counter electrode, Celgard 2250 as the separator, and commercial 1 M $LiPF_6$ in ethylene carbonate/diethyl carbonate (volume ratio 1:1) as the electrolyte.

The charge-discharge profiles were measured using a Land battery test system (LAND CT2001A) at room temperature. CV curves were obtained using Bio-Logic VMP3 electrochemical workstation. Electrochemical impedance measurements were conducted in a frequency range of 0.1-106 Hz with alternating-current voltage amplitude of 10 mV.

Material characterization. Powder X-ray diffraction (XRD) was determined by using a Rigaku Miniflex II diffractometer with Cu Kα radiation. The morphology, crystalline phase, and composition of the as-synthesized products were obtained on field-emission scanning electron microscopy (FESEM,FEI Nova 430), transmission electron microscopy, high-resolution transmission electron microscopy (HRTEM, FEI Titan STEM), and atomic force microscopy (Bruker Dimension Icon Scanning Probe Microscope). XPS analysis was performed using an ESCALAB 250Xi spectrometer by a mono Al Kα radiation. Raman spectroscopy was measured with Renishaw 2000 System. AFM images of eoG were taken using Bruker Dimension Icon Scanning Probe Microscope. Thermogravimetric analysis was characterized using Netzsch STA 449 F3 Jupiter.

4.3 Results and discussion

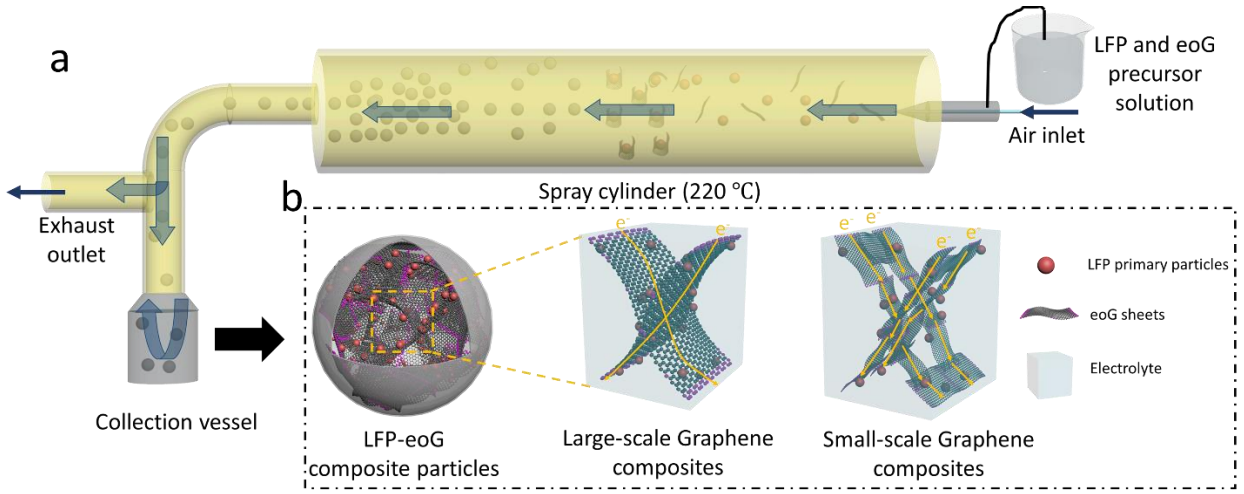

Figure 4.1 **a** A schematic of spray-drying process. **b** A schematic of LFP-eoG composite sphere and the transportation of electrons inside the LFP-eoG electrode.

Commercial LFP was mixed with eoG, stirring and sonicating for 1 hours to form a homogeneous precursor dispersion. This well-dispersed LFP and eoG precursors were then conducted a spray drying as reported in previous work[184] to obtain a LFP-eoG composite cathode materials (Figure 4.1a). In the heating zone at 220℃, the eoG sheets wrapped up LFP primary particles to form a composite sphere which was then harvested in the collection vessel. The architecture of LFP-eoG composite is shown in Figure 4.1b, where the eoG sheets loaded by LFP nanoparticles folded, twisted and encapsulated into a spherical morphology. The LFP primary nanoparticles uniformly anchored on the surface of eoG sheets, which contributes to a lower contact resistance between active materials and conducting network compared with pristine graphene derived composite materials that are assembled in aqueous system. Because the excellent water dispersity of eoG avoids the restacking of graphene, which helps eoG combine in a uniform way with LFP primary particles. Moreover, the large lateral size of eoG is another advantage as an excellent building block of the conductive network. Large-lateral-size graphene has more

ordered stack behavior during the spray-drying process. It improves the long-range conductivity of LFP-eoG composites. On the contrary, small-lateral-size graphene is supposed to compose a disordered pack with active materials, which increase the contact resistance between the different graphene sheets (Figure 4.1b).

4.3.1 Characterization

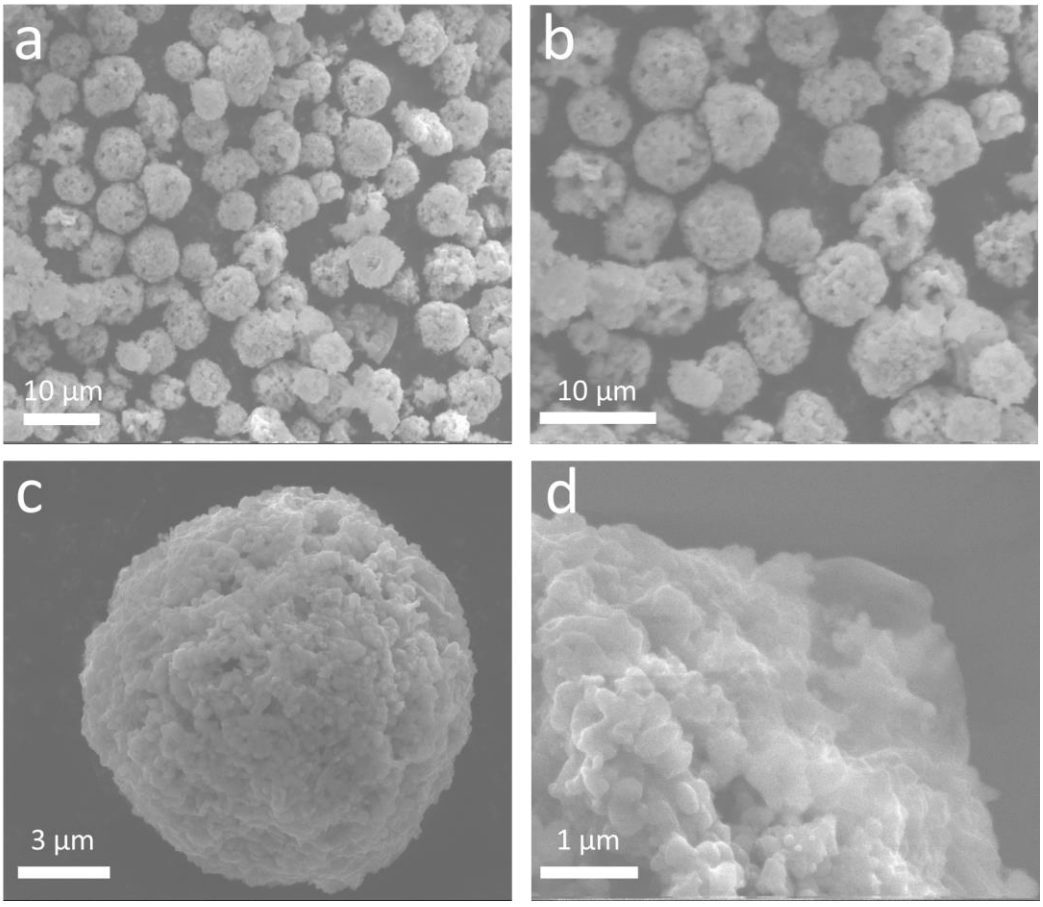

Figure 4.2 a-d SEM images of $LiFePO_4$/eoG (LFP-eoG) particles under different magnification.

The morphologies of LFP-eoG were investigated by using SEM, the corresponding results are shown in Figure 4.2 a-d. From Figure 4.2 a-b, it is seen that LFP-eoG composites show a spherical

morphology with a sphere diameter of 5-10 μm. When we zoomed in to focus on the single LFP-eoG composite sphere (Figure 4.2c), it is found that the LFP-eoG sphere consists of LFP primary nanoparticles with the size of around ~30 nm. It is also observed that wavelet-like wrinkles are wrapping up on the surface of LFP-eoG, which confirms to be the eoG by SEM-EDS and will be verified by TEM results as following (Figure 4.2d). The SEM images of lotus-bud-like LFP-eoG composite reveals that during the spray drying process, the commercial LFP nanoparticles aggregated into a large-size cluster and assembled with eoG sheets to form these spherical composite particles.

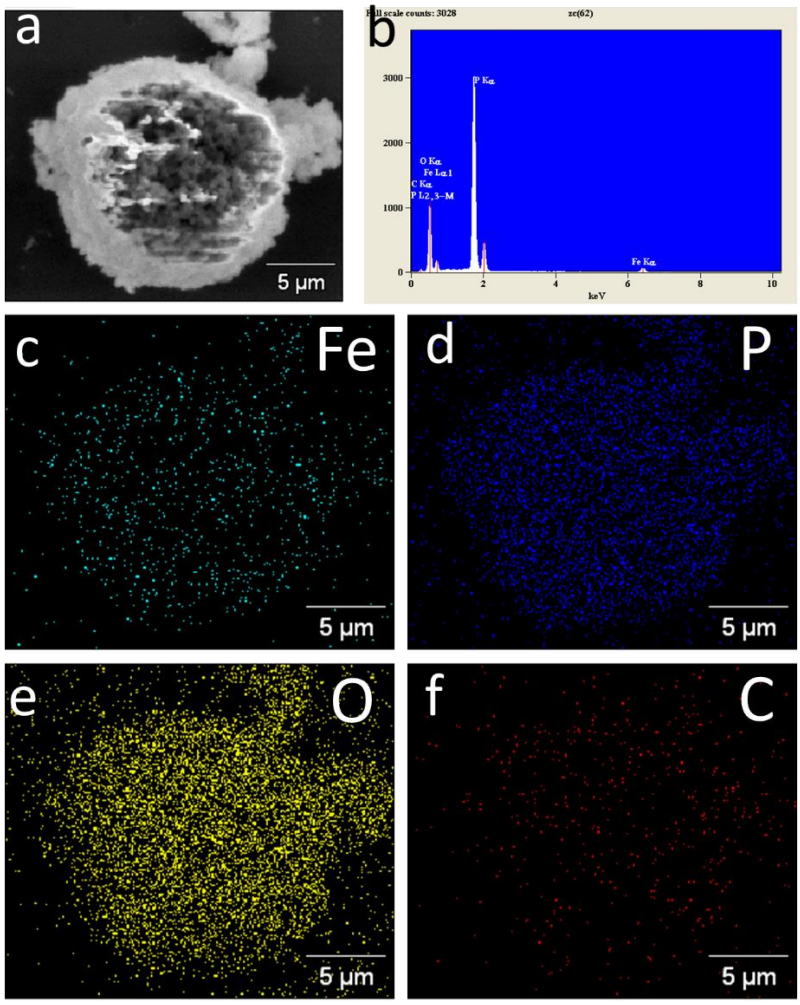

Figure 4.3 a SEM image of LFP-eoG particles under EDS mode **b** EDS spectrum of LFP-eoG **c-f** Element mapping of P, C, O, Fe of LFP-eoG particles.

SEM-EDS was conducted to further study the distribution of the elements on LFP-eoG composite. As shown in Figure 4.3 c-f, the individual elemental mapping of phosphorus, carbon, oxygen and iron reveals the uniform dispersion of $LiFePO_4$ nanoparticles and eoG sheets, which is consistent with the schematic shown in Figure 4.1.

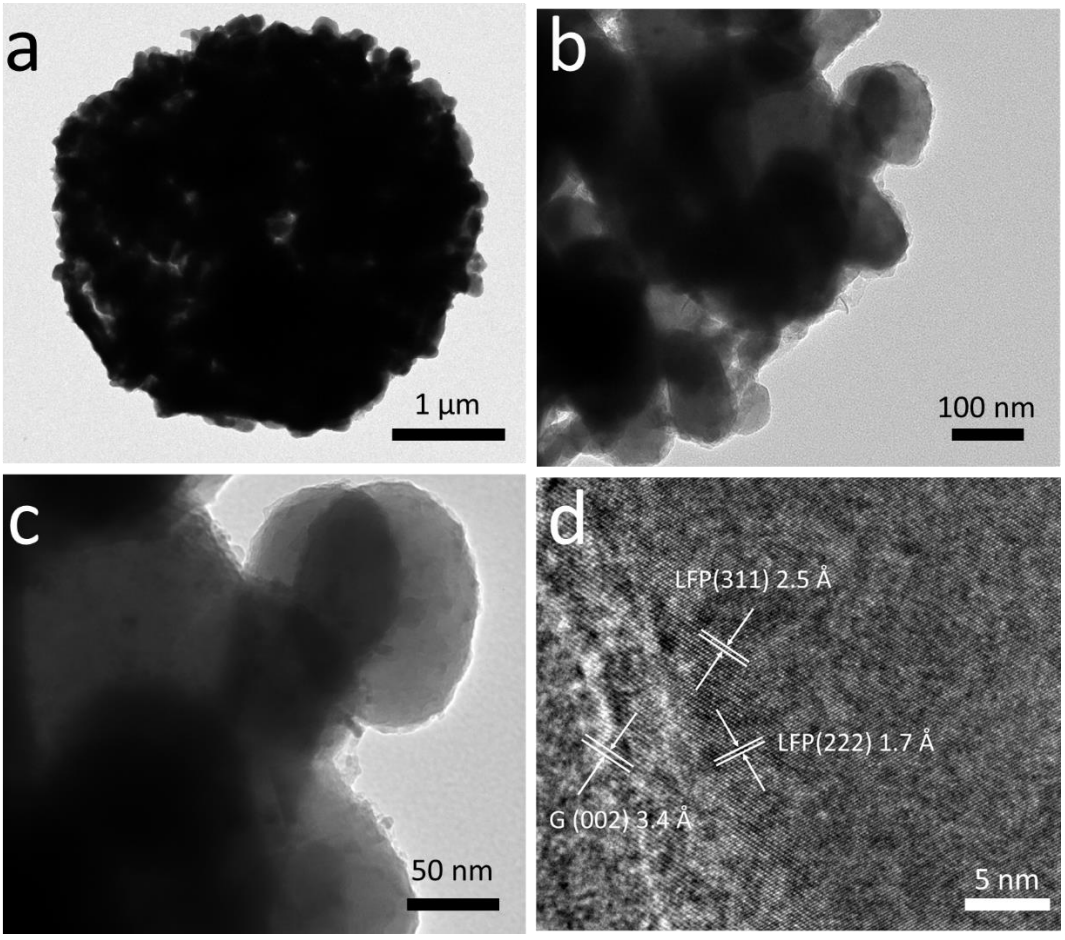

Figure 4.4 a, b, c TEM images of LFP-eoG composites. **h** High-resolution TEM image of LFP-eoG composites.

To study the microscopic structure of LFP-eoG composites, TEM was conducted as shown in Figure 3 g-i. It is revealed that LFP primary particles in the range of 30-50 nm were assembled with eoG sheets into LFP-eoG composite spheres of 5-10 μm size (Figure 4.4 a-c). The eoG sheets folded and bended in the LFP-eoG composites to provide a good electronic transport network. The HRTEM image of LFP-eoG composites in Figure 3 d demonstrates the lattice fringes of the LFP primary particles with d-spacing of 0.25 nm and 0.17 nm, corresponding to the (311) and (222) crystal planes of olivine $LiFePO_4$. The lattice fringes of graphene with d-spacing of 0.34nm are also observed, which are consistent with the (002) plane of graphene.

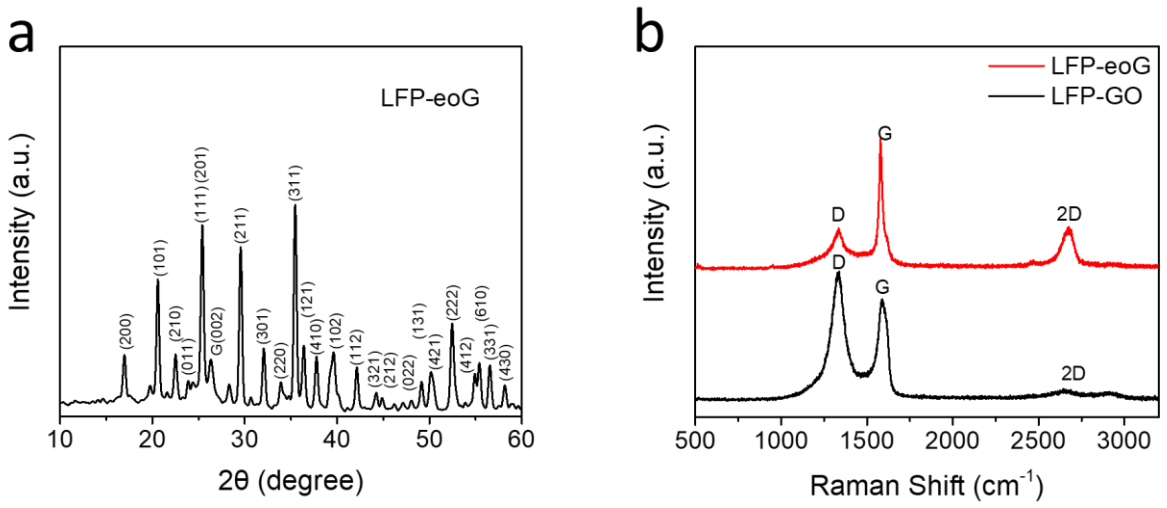

Figure 4.5 a XRD pattern of LFP-eoG composites. **b** Raman spectra of LFP-eoG composites and LFP-GO composites.

The X-ray diffraction patterns of LFP-eoG are shown in Figure 4.5a, which shows peaks that can be attributed to the phospho-olivine $LiFePO_4$ without any impurity phase. The peak at $2\theta=26.5°$ was the graphene (002) peak which furtherly confirms the existence of eoG in the composite particles. The Raman spectra of LFP-eoG composites and LFP-GO composites is shown on Figure 4.5b. The intensity ratio of the D/G bands for the LFP-eoG composites (0.20) is lower than that of

LFP-GO (1.37), confirming that after the spray-drying and annealing process, eoG still has much less disorder defects than GO.

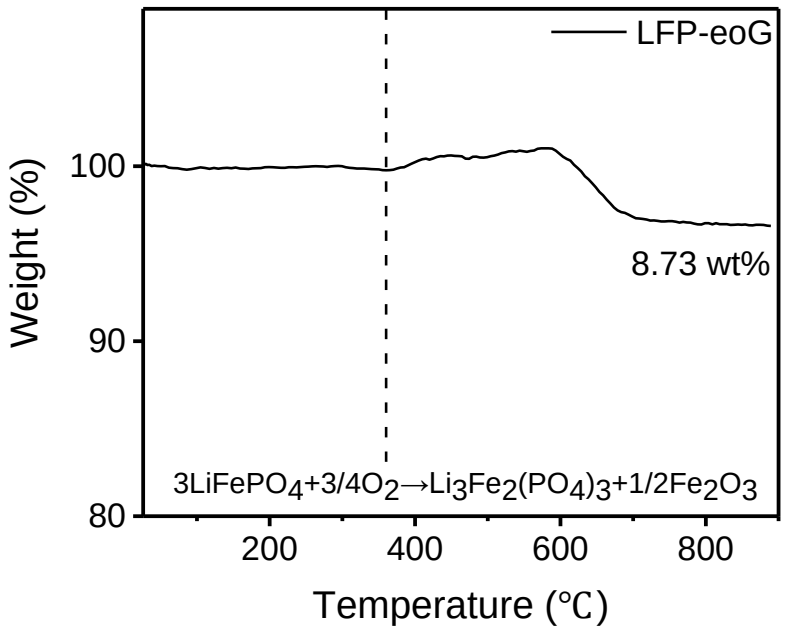

Figure 4.6 Thermogravimetric curves of LFP-eoG in the air atmosphere.

In the thermogravimetric curves shown in Figure 4.6, the weight changed over 2 steps. LFP-eoG composite started to gain weight at around 360℃ because $LiFePO_4$ reacted with oxygen in the air to form Fe_2O_3 and $Li_3Fe_2(PO_4)_3$.[228] At around 600 ℃, graphene reacted with oxygen to produce CO_2 and the weight was decreased. Thus, the weight loss of graphene from carbon decomposition can represent the graphene content in the composite materials. The results show that the graphene contents of LFP-eoG were 8.73 wt%.

4.3.2 Electrochemical performance

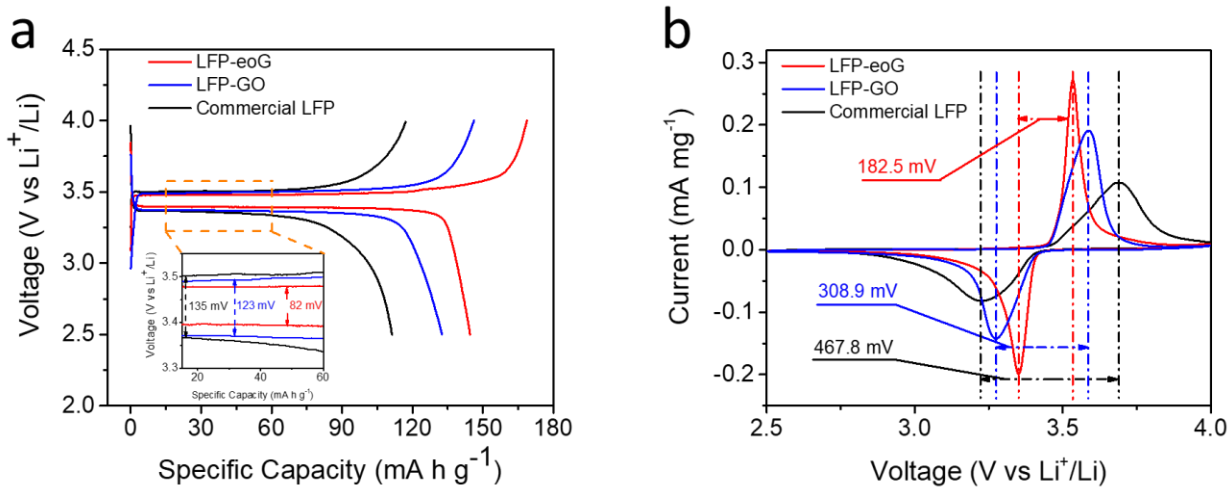

Figure 4.7 Electrochemical performance and kinetic analyses of the LFP-eoG, LFP-GO, and commercial LFP. **a** Charge -discharge profiles of LFP-eoG, LFP-GO and commercial LFP at 0.5 C. **b** CV curves of the LFP-eoG, LFP-GO, and commercial LFP at the sweep rate of 0.05 mV s^{-1}.

The electrochemical performance of the LFP-eoG and commercial LFP electrode were investigated in coin cells with Li metal as both the counter and reference electrode. Figure 4.7a shows the charge-discharge profiles of LFP-eoG and commercial LFP at 0.5C in the potential window of 2.5-4.0V (vs Li^+/Li). The LFP-eoG exhibits a much higher discharge capacity (144.5 mAh g^{-1}) than that of the LFP-GO (132.5 mAh g^{-1}) and commercial LFP (111.3 mAh g^{-1}) under the same conditions. As shown in the embedded Figure 4.7a, LFP-eoG delivers a flatter and longer voltage plateau and shows a lower potential interval (82 mV) than LFP-GO with a potential interval of 123 mV and commercial LFP with a potential interval of 135 mV, suggesting that LFP-eoG suffers from a lower polarization loss. These results demonstrated that the eoG network can significantly improve the kinetics of electron transport in LFP composite electrode.

Cyclic voltammograms (CV) of LFP-eoG, LFP-GO and commercial LFP are shown in Figure 4.7b. Under a scan rate of 0.05 mV s^{-1}, LFP-eoG exhibits the anodic peak at 3.54 V which is

consistent to the oxidation of Fe^{2+} to Fe^{3+}, while the cathodic peak at 3.35 V is corresponded reduction of Fe^{3+} to Fe^{2+}. The potential interval between these two redox peaks of LFP-eoG is 182.5 mV. By comparison, the potential interval of LFP-GO is 308.9 mV and that of commercial LFP is 467.8 mV which is higher than LFP-eoG. The gap between those three potential intervals are due to the different carbon matrixes. Small lateral size GO can provide conductive network of electrons and lithium ions to increase the electronic and lithium ion conductivity, but the defects and contact resistance among GO sheets limited the decrement of overpotential. However, eoG sheets have larger lateral size and fewer defects which leading to lower contact resistance (further proved in EIS results) and high electronic conductivity, thus LFP-eoG electrode decrease the potential interval by 61% compared to the commercial LFP electrode.

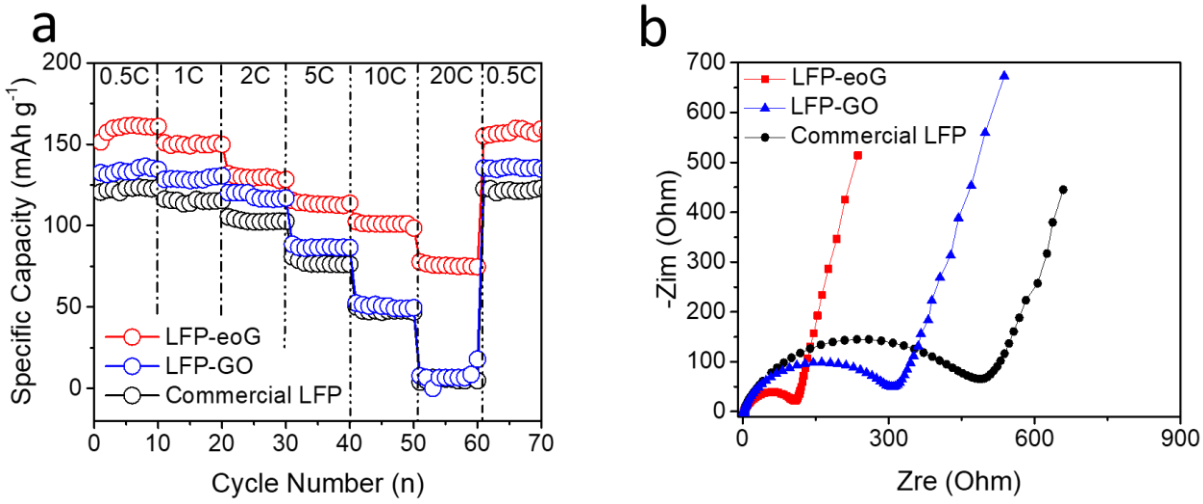

Figure 4.8 a Rate capabilities of the LFP-eoG, LFP-GO, and commercial LFP at various current densities ranging from 0.5 C to 20 C. **b** EIS profile of the LFP-eoG, LFP-GO, and commercial LFP before cycling.

Figure 4.8a presents the rate performance of LFP-eoG, LFP-GO and commercial LFP electrodes at various charge-discharge rates. With the increasing discharge-charge rates from 0.5 C, 1 C, 2 C, 5 C, 10 C to 20 C, the LFP-eoG electrode exhibits reversible specific capacities of

159.9, 150.7, 130, 114.1, 101 and 76.6 mA h g^{-1}, while the LFP-GO electrode presents a significant lower capacity of 133.8, 128.4,120.2, 86.9, 50.5 and 6.6 mA h g^{-1}, respectively. It is noted that when charge-discharge rate was increased to 20C, LFP-eoG electrode still provides a reversible capacity of 76.6 mA h g^{-1}, which is around 12 folds higher than LFP-GO and 16 folds higher than commercial LFP. Beyond that, when returning the current rate to 0.5C, the discharge capacity of LFP-eoG can recovered to 159.5 mA h g^{-1}, indicating an excellent reversibility. The excellent electronic and ionic conductivity can be furtherly confirmed by the electrochemical impedance spectroscopic (EIS) results. As shown in Figure 4.8b, the LFP-eoG electrode exhibits the shortest Warburg region with the smallest semicircle diameter compared to LFP-GO and commercial LFP, indicating higher electronic conductivity and faster lithium-ion diffusion rate than LFP-GO and commercial LFP electrode.

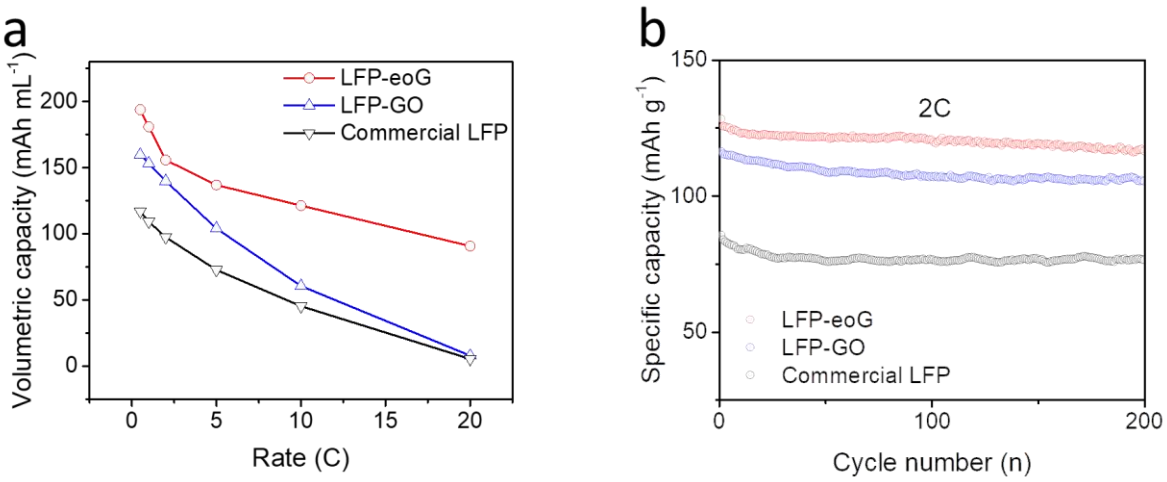

Figure 4.9 a Volumetric capacity of the LFP-eoG, LFP-GO and commercial LFP electrodes at different C rates. **B** Cyclabilities of the LFP-eoG, LFP-GO, and commercial LFP at 2 C.

The volumetric capacity of LFP-eoG, LFP-GO and commercial LFP electrodes were evaluated by various charge-discharge rates, as shown in Figure 4.9a. The volumetric capacities of the anodes reported were estimated based on the tap density and gravimetric specific capacity. This micron-sized spherical morphology significantly increased the tap density of LFP-eoG and LFP-GO to ~1.2 g cm^{-3} and ~1.2 g cm^{-3}, respectively, which is 26% higher than commercial LFP (0.95 g cm^{-3}). The LFP-eoG electrode shows a reversible volumetric capacity of 155 mA h mL^{-1} at 2C, which is significantly higher than that of LFP-GO (139 mA h mL^{-1}) and commercial LFP (97 mA h mL^{-1}). At a higher rate of 20 C, LFP-eoG electrode still provides a volumetric capacity of 91 mA h mL^{-1}, which is 10 folds and 16 folds higher than that of LFP-GO electrode (7.9 mA h mL^{-1}) and commercial LFP electrode (mA h mL^{-1}). This high volumetric capacity of LFP-eoG electrode is contributed to the spray-drying assemble approach.

We also examined the cycling stability of LFP-eoG, LFP-GO and commercial LFP electrodes (Figure 3f). LFP-eoG electrode exhibits an initial discharging capacity of 128 mA h g-1 at 2 C, which is higher than that of LFP-GO (116 mA h g-1) and commercial LFP (86 mA h g-1). After 200 cycles, the LFP-eoG electrode still provides a capacity of 116 mA h g-1 at 2 C, which is much higher than that of commercial LFP electrode (76 mA h g-1) and LFP-GO (105 mA h g-1). Such significant improvement may be attributed to the robust composite structure constructed from large-lateral-size eoG, which maintain the charge transport networks during long cycling process.

4.4 Conclusion

The unique architecture of eoG nanosheets provides excellent affinity towards active materials in aqueous solution to fabricate LFP-eoG composite electrode materials, which exhibit low polarization (82 mV at 0.2 C), high electrical and ionic conductivity (926 S cm^{-1}), excellent rate capability (76.6 mA h g^{-1} at 20 C) and stable cycle performance (200 cycle with retention rate of 93%). We hope that this work will open the pathway to develop the large-lateral-size graphene with excellent water solubility that can tackle the challenges of lithium-ion batteries.

Chapter 5 Carbon nanotube embedded graphite anode for high-power lithium ion batteries

5.1 Introduction

Lithium ion batteries (LIBs) are the most ubiquitous energy storage system, which is commonly used in portable electronic devices, due to their long cycle life, high energy and power density, and high stability. Since it was first found by Rajeeva R. Agarwal and J. Robert Selman that lithium ions can have a reversible electrochemical intercalation with graphite[48], graphite becomes one of the most commonly used anode materials and holds its position as the current commercial anode for LIBs, due to its high theoretical capacity of 372 mA h g^{-1}, good stability and long cycle life. Although graphite has high intrinsic conductivity of 2.26×10^4 S cm^{-1}[74], it suffers from lithium plating issues caused by limited lithium ion diffusion rate in graphite[229, 230], which however limits the rate performance. At high current rate, the transport rate of Li^+ from electrolyte exceed the Li-intercalation rate[231]. This accumulated Li^+ deposits on the surface of graphite, leading to anode polarization and lithium plating phenomenon. As a result, the deposited lithium metal undergoes electrical isolation and has a side reaction with electrolyte, which cause capacity fading and safety issues.

Extensive efforts have been made to improve the lithium ion diffusion rate in graphite, such as making porous structure or void space[148, 232-234], building up aligned architecture[235], and conducting surface modification with amorphous carbon or high-rate anode materials to form composite anodes (e.g. coal tar pitch, carbon nanotubes, $Li_4Ti_5O_{12}$, TiO_{2-x})[163, 236-240], which either increase the lithium intercalation site or shorten the ion-diffusion length. Such porous structure, however, has a moderate improvement for graphite anode due to the limited additional

intercalation site that it can offer to lithium ions. Meanwhile, the aligned architecture of graphite changes the lithium ion pathway in a macroscopic aspect, but it still remained a sluggish intercalation kinetics problem on the surface of graphite. Moreover, such amorphous carbon or carbon nanotubes (CNTs) coating dramatically lowers the initial coulombic efficiency due to the irreversible capacity loss, while LTO or TiO_{2-x} modified graphite anodes exhibit high working voltage, which decrease the overall energy density.

We envision that this limitation can be addressed by designing a novel CNTs embedded graphite (denoted as CNT-Graphite) anode through the graphite intercalation compound route and chemical vapor deposition (CVD), which expands the interlayer spacing of graphite, enabling effective transport of ions and electrons. Meanwhile, the CNTs network which are intercalated into graphite interlayers act as a transit reservoir for lithium ions, accommodating the gap between Li intercalation rate and Li plating rate.

Such CNTs embedded graphite was synthesized by firstly intercalating $FeCl_3$ into graphite at 600℃ and 1.35Mpa. This $FeCl_3$-graphite intercalation compounds ($FeCl_3$-GICs) was then heated in the air at 80℃ to form Fe_2O_3-GICs. Since Fe_2O_3 has catalytic activity towards the formation of CNTs. We grew nitrogen-doped CNTs inside graphite interlayers through a CVD process using acetonitrile as carbon source at 900℃.

Compared with current state of arts, this CNTs-graphite composite anode is designed from a microscopic level to directly change the interlayer structure by expanding interlayer spacing and building up CNTs network that acts as transit reservoirs for lithium ions, which improve the lithium ion diffusion rate as well as electrical conductivity, enabling high reversible capacity and good rate performance for lithium ion batteries.

5.2 experimental

Synthesis of $FeCl_3$-GIC. $FeCl_3$ (0.08g, Alfa Aesar) was fully mixed with the graphite flake (0.08g, Sigma-Aldrich). Then the mixture was sealed in a stainless-steel autoclave and was heated to 600℃ for 6h. After cooling down, $FeCl_3$-GIC was obtained.

Synthesis of Fe/Fe_2O_3-GIC. $FeCl_3$-GIC was washed by ethanol for 3 times to remove the $FeCl_3$ remains on the surface. Such $FeCl_3$-GIC was filtrated and transfer into a quartz boat. Then It was heated at 80℃ for 12h to form a Fe_2O_3-GIC.

Synthesis of CNT-Graphite. Fe/Fe_2O_3-GIC in a quartz boat was first placed in the center of a tube furnace with a gas flow containing Argon (500 mL min^{-1})/ H_2 (50 mL min^{-1}) and heated to 900℃. Then, another Argon stream (100 mL min^{-1}) flowing through a flask of acetonitrile at 80℃ was introduced to the reactor to grow N-doped CNT on the Fe particles inside graphite interlayers. After deposition for 1 hour, as-formed CNT-Fe-GIC was collected and treated with 1 M hydrochloride acid to remove Fe catalyst and form CNT-Graphite composite.

Electrochemical measurements. The electrodes of CNT-Graphite and commercial graphite were prepared by slurry-coating method. Active materials (CNT-Graphite and commercial graphite), super P carbon black, and binder (PVDF) were adequately mixed with a mass ratio of 80:10:10. The mixture were dispersed in N-methyl-2-pyrrolidone forming a slurry, which were afterward coated onto a copper foil. All of the obtained well-dried electrodes were measured to have an areal loading of 1.5 mg cm^{-2}. These electrodes were integrated into CR2032-type coin cells using Lithium metal as counter electrode, Celgard 2250 as the separator, and commercial 1 M $LiPF_6$ in ethylene carbonate/diethyl carbonate (volume ratio 1:1) as the electrolyte.

The charge-discharge profiles were measured using a Land battery test system (LAND CT2001A) at room temperature. CV curves were obtained using Bio-Logic VMP3 electrochemical workstation.

5.3 Results and discussion

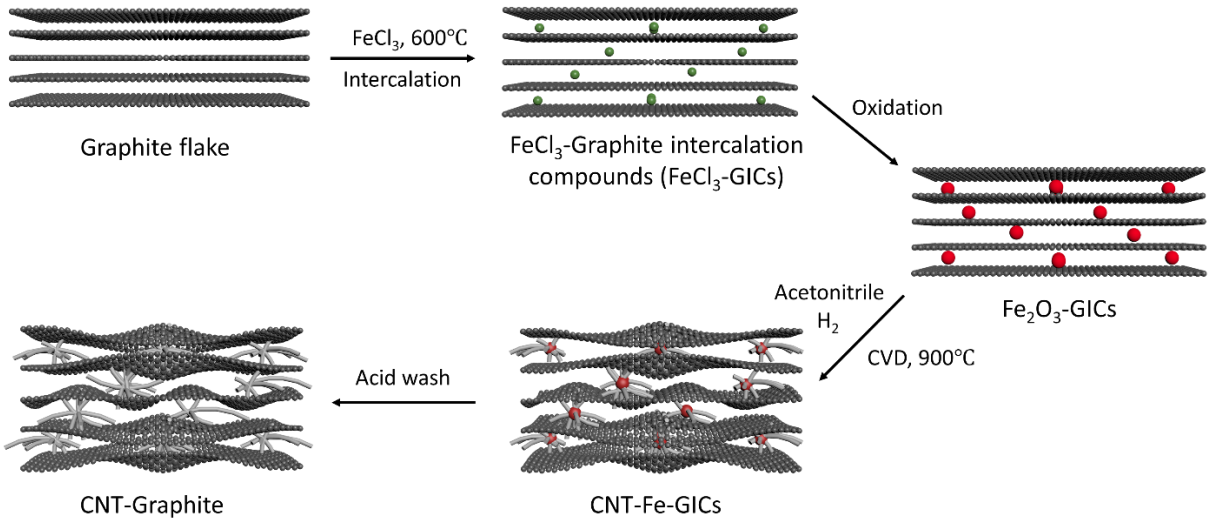

Figure 5.1 Schematic of synthesizing CNT-Graphite through a graphite intercalation compound route and chemical vapor deposition (CVD).

The synthetical process of CNT-graphite is shown in Figure 5.1. The first intercalation step is the same as the method we presented in chapter 3. This gaseous $FeCl_3$ with high temperature ($FeCl_3$) and pressure (1.35 Mpa) is successfully intercalated into graphite interlayer to form $FeCl_3$-Graphite intercalation compounds (denoted as $FeCl_3$-GICs), which is furtherly proved by SEM and XRD results. As-formed $FeCl_3$-GICs is then heated at 80℃ in the air to form Fe_2O_3-GICs. Such Fe_2O_3 was reduced to Fe by hydrogen during the CVD process. It is noted that Fe has the catalytic activity towards the deposition of carbon radicals to grow carbon nanotubes. Therefore, we use acetonitrile as carbon source to grow the nitrogen-doped CNTs onto the Fe particles inside graphite interlayers. After washed by hydrochloride acid, the CNT-Graphite composite was collected by filtration and drying for 8 hours.

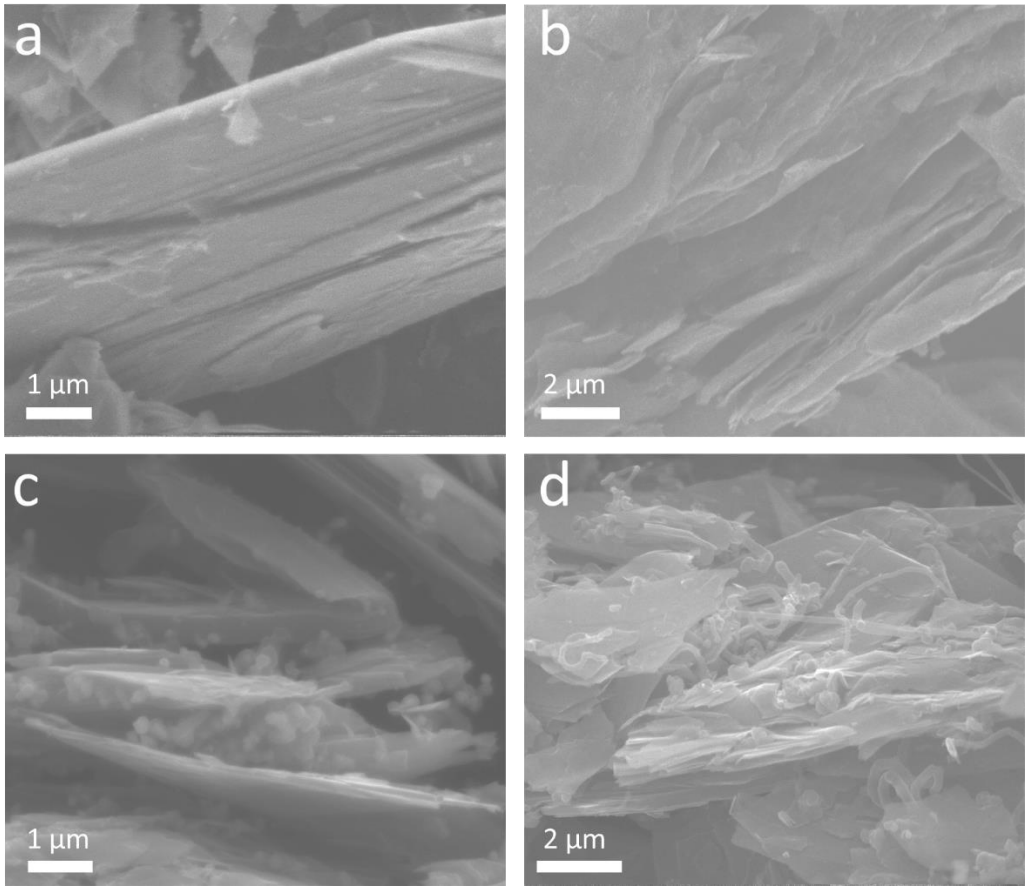

Figure 5.2 SEM images, showing the interlayer structure of **a** graphite flake **b** $FeCl_3$-graphite intercalation compounds ($FeCl_3$-GICs) **c** Fe_2O_3-GICs d CNT-Graphite.

To study the interlayer structure of graphite, SEM was conducted as shown in Figure 5.2. Pristine graphite flake exhibits compact and ordered interlayers architectures (Figure 5.2 a). The SEM images of $FeCl_3$-GICs shows the interlayer spacing was expanded (Figure 5.2b), indicating the effective intercalation of $FeCl_3$. After the oxidization, $FeCl_3$ was reacted to form Fe_2O_3 in the air. We control the temperature at 80℃ to avoid the formation of Fe_2O_3 particles with large size, because large Fe nanoparticles (after H_2 reduction) lead to thick CNTs which, however, cannot insert into graphite interlayers. As show in Figure 5.2c, it turns out that the Fe_2O_3 was formed inside interlayers after oxidization process, and the interlayer spacing of graphite was furtherly

expanded. The morphology of CNT-Graphite was finally obtained after CVD process and acid wash. As we can see from Figure 5.2d, the CNTs stick out from the interlayer with a considerate length (several micron meters).

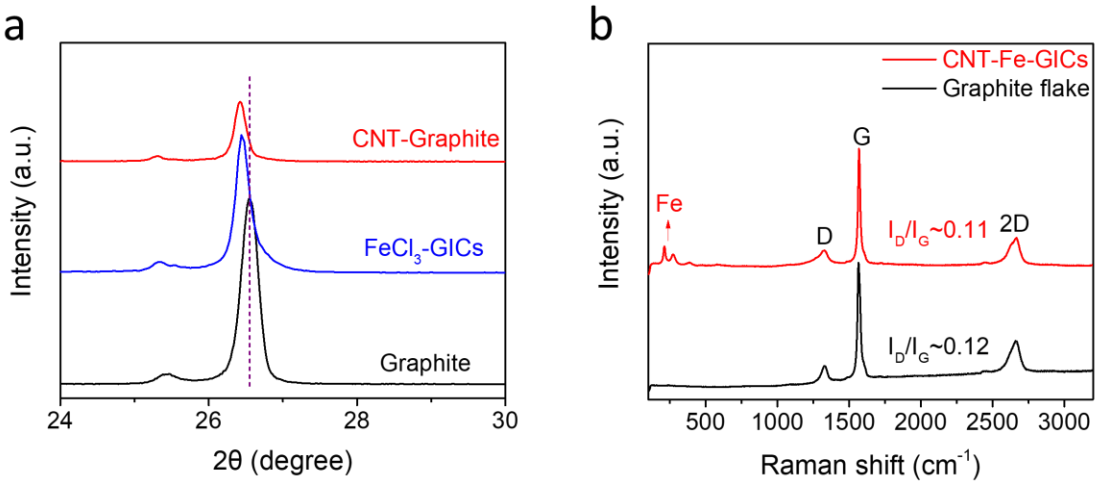

Figure 5.3 a XRD pattern of graphite, $FeCl_3$-GICs and CNT-Graphite. **b** Raman spectrum of CNT-Fe-GICs and Graphite flake.

The XRD pattern was conducted to characterize the crystal structure of CNT-Graphite, which is shown in Figure 5.3a. Compared with graphite and $FeCl_3$-GICs, CNT-Graphite exhibits a significantly lower (002) peak, indicating that the formation of CNTs partly disrupts the layer structure of graphite and the thickness of each graphite particles decreases. It is also noted that both of the CNT-Graphite and $FeCl_3$-GIC shows a slightly shifted (002) peak (26.40° and 26.44°, respectively), compared with graphite (26.56°). It indicates that $FeCl_3$-GIC has an expanded interlayer spacing of 3.357 Å compared with that of graphite (3.343 Å), while CNT-Graphite has even larger interlayer spacing of 3.362 Å which is consistent with SEM results. Such results demonstrate that CNTs are formed between the layers of graphite and help to furtherly expanded

the layer structure, allowing an additional Li^+ reservoir as well as a wide lithium ion transport path of CNT-Graphite composite.

The Figure 5.3b shows the Raman spectrum of CNT-Fe-GICs and graphite. CNT-Fe-GICs show typical D, G, 2D peaks at 1333 cm^{-1}, 1569 cm^{-1} and 2667 cm^{-1}, respectively, while pristine graphite flake exhibit typical D, G, 2D peaks at 1325 cm^{-1}, 1565 cm^{-1} and 2659 cm^{-1}, respectively. The slightly blue shifted D, G and 2D peaks of CNT-Fe-GICs is due to doping effect induced by the charge transfer from graphite to Fe and CNTs, indicating that the graphene sheet is flanked on both sides by Fe and CNTs in CNT-Fe-GICs composite.[152, 191] The intensity ratio of D band to G band (D/G) is generally accepted to reflect the degree of graphitization in carbonaceous materials, where a lower D/G ratio indicates a higher degree of graphitization and better electrical conductivity.[241] The CNT-Fe-GICs and graphite exhibit similar I_D/I_G ratio, indicating that the intercalation of $FeCl_3$ and following CVD process retain the structure integrity of graphene layers. CNT-Fe-GICs also shows a Fe peaks at a range of 200 cm^{-1} to 400 cm^{-1}, proving the existence of Fe after the reduction of $FeCl_3$-GICs by H_2.

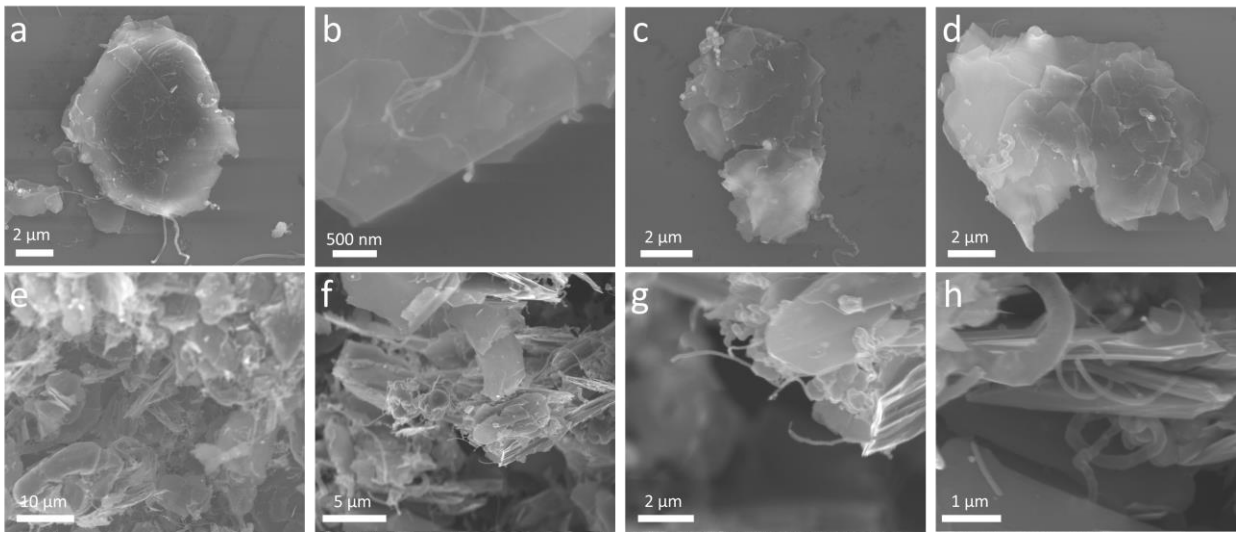

Figure 5.4 SEM images of CNT-Graphite composite from **a-d** vertical view, and **e-h** cross-section view.

To study the morphology of CNT-Graphite composite, SEM was conducted from vertical view or cross-section view as shown in Figure 5.4. It shows very few amount of CNTs on the surface of CNT-Graphite, because the residual $FeCl_3$ that fails to insert into graphite interlayers is washed away by ethanol after $FeCl_3$ intercalation step to produce $FeCl_3$-GICs, there is limited amount of catalyst remain on the surface of graphite. However, since the Fe nanoparticles amass inside the graphite interlayers, the CNTs grow from inside to out and form a graphite-CNT-graphite sandwich structure. Meanwhile, SEM-EDS images from vertical view of CNT-Fe-Graphite confirm the uniform distribution of C Fe and O (Figure 5.5 a-d). The elements contents of C, O and Fe are 86.82%, 6.44% and 6.74%, respectively.

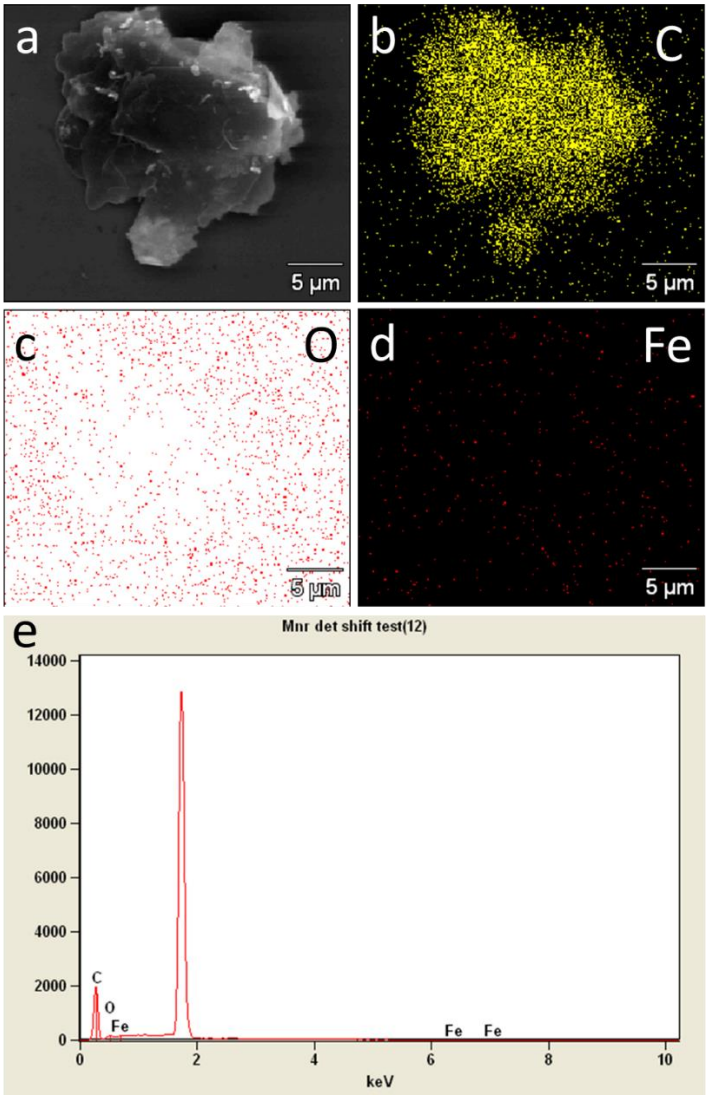

Figure 5.5 a-d Elements mapping of C, O and Fe. **e** elements content of C, O and Fe.

Such CNT-Graphite composite can effectively improve the rate performance and solve the lithium plating issue for graphite anode. On the one hand, CNTs furtherly expanded the interlayer spacing of graphite, allowing a higher lithium ion diffusion rate inside interlayers. On the other hand, CNTs can serve as a Li^+ reservoir that accommodates the gap between Li intercalation rate and Li plating rate and provide more lithium intercalation sites. Figure 5.6 shows the mechanism of lithium ion diffusion and intercalation during the discharge process under different current rates.

At low current rate, the lithium ion diffusion rate in electrolyte is low, thus it can achieve a balance between lithium diffusion rate and lithium intercalation rate. At low current rate, the lithium ions orderly insert to form Li_xC_6, accepting one electron per lithium ion. The situation is similar for CNT-Graphite, but lithium ions can either intercalate into the site in graphite interlayers or in CNTs. Therefore, the rate capacity of CNT-Graphite and graphite do not have big difference at low rates.

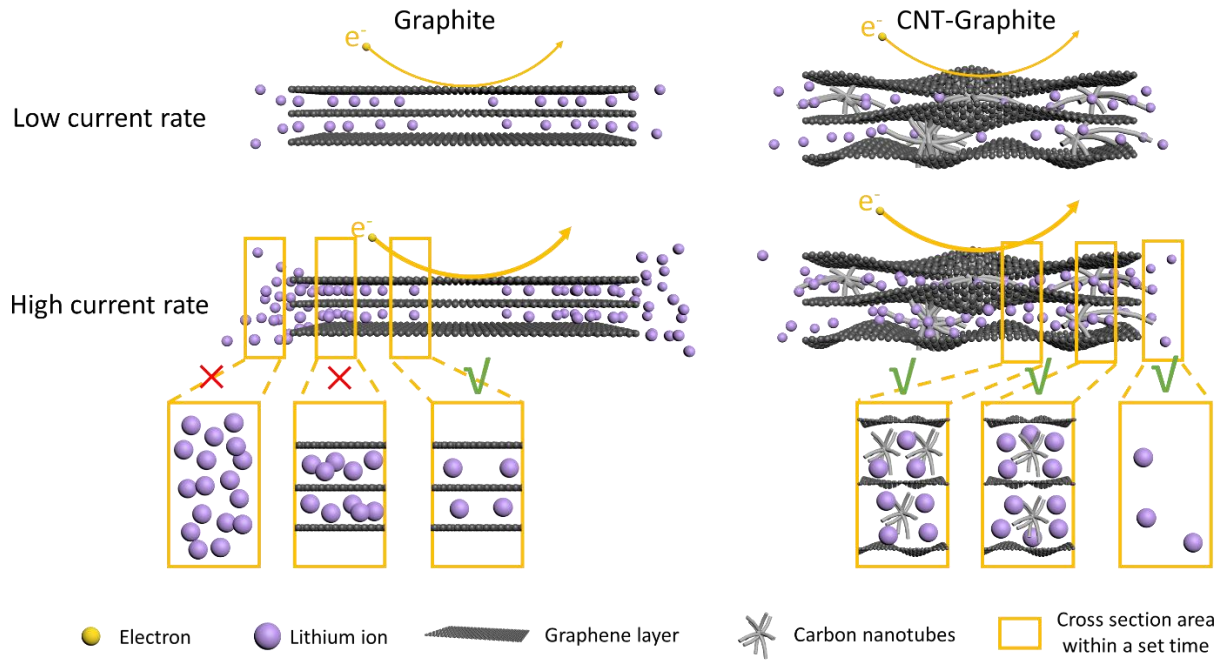

Figure 5.6 Schematic of the mechanism of lithium ion intercalation and diffusion for Graphite and CNT-Graphite composite under different current rates.

Although graphite has high electrical conductivity, the lithium intercalation rate is limited. At high current rates, the electron transport rate as well as lithium ion diffusion rate in electrolyte increase. Once the lithium intercalation rate is not able to match up the lithium diffusion rate in electrolyte, lithium ions will block and gather in the surface of graphite. If we take a cross section to study the diffusion phenomenon, it is clear that the lithium diffusion rate inside limits the

transport of Li^+ in the outer graphite interlayers and furtherly blocks the diffusion from surface to outer intercalation sites. Nevertheless, CNT-Graphite composite has a higher interlayer spacing which is proved by SEM and XRD results, creating a faster Li^+ diffusion path than graphite. In this way, Li^+ transport inside interlayers with a higher speed, enables Li^+ diffuse smoothly from electrolyte to inner sites of CNT-Graphite. Moreover, the CNTs can also adsorb Li^+, creating more Li intercalation site for composite, and thus act as a reservoir to store and transit lithium ions.

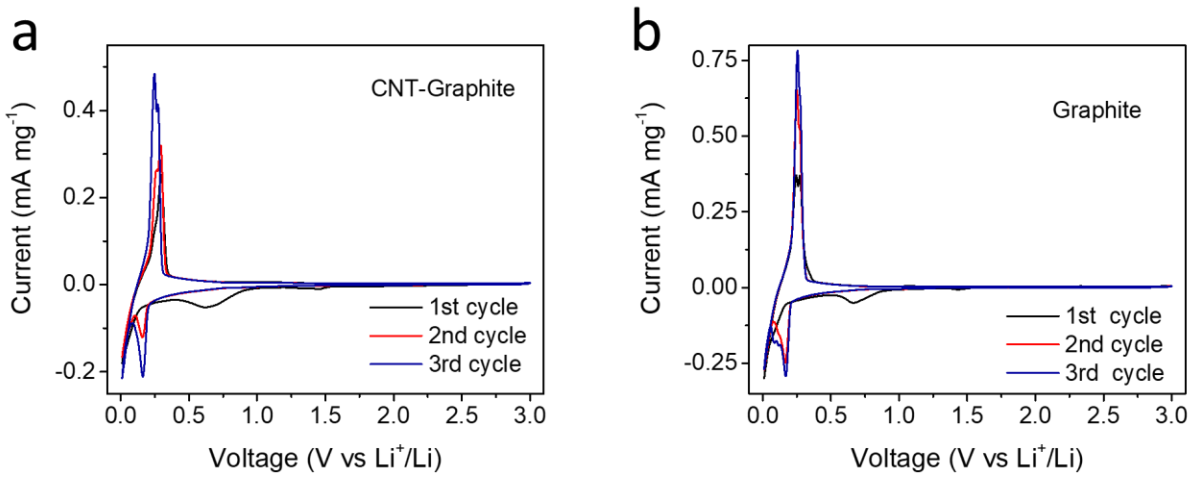

Figure 5.7 The first three CV curves of **a** the CNT-Graphite and **b** the graphite with a scan rate of 0.1 mV s^{-1} between 0.01V and 3.0 V.

The electrochemical performance of CNT-Graphite was investigated in coin cells using Li metal as the anodes, which were compared with that of graphite. The Cyclic voltammograms (CV) curves of the first three cycles of the CNT-Graphite anode and graphite anode at a scan rate of 0.1 mV s^{-1} in the range between 0.01V and 3V are shown in Figure 5.7, respectively. The peak at 0.66 V for the first cycle is caused by the partial reduction of electrolyte components at electrode/electrolyte interface[242], resulting in the formation of SEI layer. The sharp reduction peaks at around 0V represent the intercalation of Li^+, and the sharp oxidation peaks at around 0.25V

correspond to the deintercalation of Li^+. As we can see, after the intercalation of CNTs, CNTs-Graphite composite anode shares the same reduction and oxidation reaction with pristine graphite with the same potential, indicating that the CNTs do not destroy the basic framework of graphite layered structure.

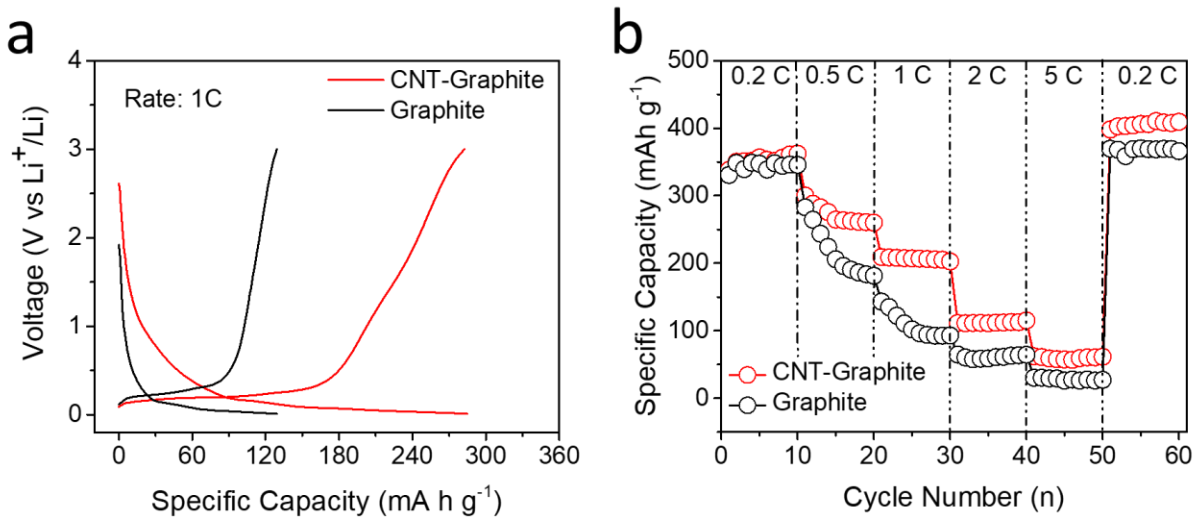

Figure 5.8 Electrochemical performance and kinetic analyses of the CNT-Graphite and graphite anodes. **a** Charge -discharge profiles of CNT-Graphite and graphite anodes at 1 C rate. **b** Rate capabilities of the CNT-Graphite and graphite at various current densities ranging from 0.2 C to 5 C.

Figure 5.8a shows the charge-discharge profiles of CNT-Graphite and graphite anodes at 1 C in the potential window of 0.01V-3.0V (vs Li^+/Li). The CNT-Graphite exhibits a much higher discharge capacity (284.8 mA h g^{-1}) than that of Graphite (129.3 mA h g^{-1}). Both the CNT-Graphite and graphite anodes show a flat and stable plateau at 0.092 V and 0.068 V, respectively, indicating that CNT-Graphite still keeps a layered structure with good capability to insert and extract lithium ions.

The rate performance of CNT-Graphite and graphite electrodes are presented in Figure 5.8b at various charge-discharge rate. With the increasing discharge-charge rates from 0.2 C, 0.5 C, 1 C, 2 C, 5 C, the CNT-Graphite electrode exhibits reversible specific capacities of 361.1 mA h g^{-1}, 264.7 mA h g^{-1}, 207.1 mA h g^{-1}, 112.9 mA h g^{-1} and 61.1 mA h g^{-1}, while the graphite electrode exhibits a significant lower capacity of 351.5 mA h g^{-1}, 183.7 mA h g^{-1}, 92.7 mA h g^{-1}, 59.1 mA h g^{-1} and 26.3 mA h g^{-1}, respectively. It is noted that when discharge-charge is increased to 5 C, CNT-Graphite electrode can still provide a reversible capacity of 61.1 mA h g^{-1}, which is ~1.3 folds higher than graphite. Moreover, upon returning the rate to 0.2C, the discharge capacity of CNT-Graphite is increased to 402.6 mA h g^{-1}, which is even higher than graphite theoretical capacity due to the small amount of CNT in CNT-Graphite electrode, indicating an excellent reversibility.

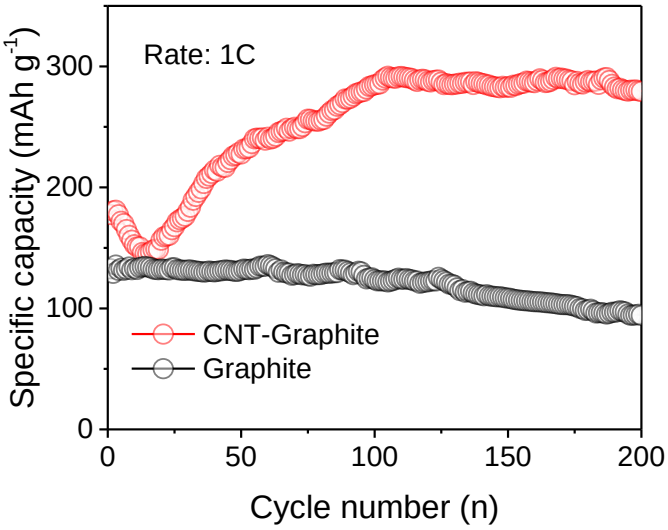

Figure 5.9 Cyclabilities of the CNT-Graphite and graphite electrodes at 1 C.

We also studied the cycling stability of CNT-Graphite and graphite. The CNT-Graphite electrode exhibits an initial charge capacity of 180.5 mA h g^{-1} and reduces to 142.5 mA h g^{-1} after 14 cycles. Then the capacity of CNT-Graphite gradually increases to 291.9 mA h g^{-1} and keeps stable after 105 cycles, which is much higher than that of graphite at the same cycle (121.8 mA h g^{-1}). After 200 cycles, the CNT-Graphite still provides a capacity of 279.7 mA h g^{-1} at 1 C, which is much higher than that of graphite (95 mA h g^{-1}). Such significant improvement is due to the CNT network inside graphite interlayers, which expands Li^+ transport path and improve the ability to intercalate Li^+ for composite electrode.

5.4 Conclusion

In conclusion, we have successfully synthesized a carbon nanotube embedded graphite anode through graphite intercalation compound route and chemical vaper deposition. The CNTs are proved to be grown inside the interlayers of graphite and retain a graphite layered structure without disrupting. It helps to expand interlayer spacing and act as transit reservoirs for lithium ions, which improve the lithium ion diffusion rate as well as electrical conductivity. Such well-designed CNT-graphite anode exhibits high reversible capacity and good rate performance (e.g. 291.9 mA h g^{-1} at 1 C) and excellent cycling stability (e.g. >100% retention rate for 200 cycles at 2 C). It is believed that this work opens a pathway to develop high-power composite electrodes with excellent stability for lithium ion batteries.

Chapter 6 Conclusion of dissertation

In this dissertation, we have developed a catalytic exfoliation method, which enabling scale synthesis of edge oxidized graphene with large-lateral-size (10 μm), high conductivity (924 S cm^{-1}), and dispersibility (10 mg mL^{-1} in water). This method addresses the paradox of conductivity and dispersibility of graphene, opening a new avenue for application that requires graphene with both conductivity and dispersibility. Using the edge-oxidized graphene/$LiFePO_4$ composite as an example, adaption of such edge oxidized graphene leads to electrodes with dramatically improved rate preperformance (e.g. 76.6 mA h g^{-1} at 20 C), cycling stability (200 cycle with retention rate of 93% at 2 C), and volumetric capacity (e.g. 193.8 mAh mL^{-1} at 0.5 C and 91 mAh mL^{-1} at 20 C).

Based on the principle to synthesize edge-oxidized graphene, we have successfully fabricated a carbon nanotube embedded graphite anode through graphite intercalation compound route and chemical vaper deposition. The CNTs are proved to be grown inside the interlayers of graphite and retain a graphite layered structure without disrupting. It helps to expand interlayer spacing and act as transit reservoirs for lithium ions, which improve the lithium ion diffusion rate as well as electrical conductivity. Such well-designed CNT-graphite anode exhibits high reversible capacity and good rate performance (e.g. 291.9 mA h g^{-1} at 1 C) and excellent cycling stability (e.g. >100% retention rate for 200 cycles at 2 C)

We hope the work of this dissertation could broaden the composite nanotechnology by fabricating structural engineered graphene and seeking new type of catalyst for CVD. Meanwhile, it is believed that such novel carbon-based composite materials above could address the current challenges of lithium ion batteries.

Chapter 7 Reference

1. Wu, Z.-S.; Ren, W.; Gao, L.; Zhao, J.; Chen, Z.; Liu, B.; Tang, D.; Yu, B.; Jiang, C.; Cheng, H.-M., Synthesis of graphene sheets with high electrical conductivity and good thermal stability by hydrogen arc discharge exfoliation. *ACS nano* **2009,** *3* (2), 411-417.

2. Stoller, M. D.; Park, S.; Zhu, Y.; An, J.; Ruoff, R. S., Graphene-based ultracapacitors. *Nano letters* **2008,** *8* (10), 3498-3502.

3. Matsumoto, M.; Saito, Y.; Park, C.; Fukushima, T.; Aida, T., Ultrahigh-throughput exfoliation of graphite into pristine 'single-layer'graphene using microwaves and molecularly engineered ionic liquids. *Nature chemistry* **2015,** *7* (9), 730.

4. Aneke, M.; Wang, M., Energy storage technologies and real life applications–A state of the art review. *Applied Energy* **2016,** *179*, 350-377.

5. Larcher, D.; Tarascon, J.-M., Towards greener and more sustainable batteries for electrical energy storage. *Nature chemistry* **2015,** *7* (1), 19-29.

6. Øvergaard, S., Issue paper: Definition of primary and secondary energy. *Statistics Norway, Oslo* **2008**.

7. Bahnfleth, W. P.; Song, J., Constant flow rate charging characteristics of a full-scale stratified chilled water storage tank with double-ring slotted pipe diffusers. *Applied thermal engineering* **2005,** *25* (17-18), 3067-3082.

8. Mahlia, T.; Saktisahdan, T.; Jannifar, A.; Hasan, M.; Matseelar, H., A review of available methods and development on energy storage; technology update. *Renewable and Sustainable Energy Reviews* **2014,** *33*, 532-545.

9. Sahin, F.; Vandenput, A. In *Design considerations of the flywheel-mounted axial-flux permanent-magnet machine for a hybrid electric vehicle*, 8th European Conference on Power Electronics and Applications (EPE 1999), 1999; pp 1-9.

10. Mellor, P.; Schofield, N.; Howe, D., Flywheel and supercapacitor peak power buffer technologies. **2000**.

11. Iglesias, I.; Garcia-Tabares, L.; Agudo, A.; Cruz, I.; Arribas, L. In *Design and simulation of a stand-alone wind-diesel generator with a flywheel energy storage system to supply the required active and reactive power*, 2000 IEEE 31st Annual Power Electronics Specialists Conference. Conference Proceedings (Cat. No. 00CH37018), IEEE: 2000; pp 1381-1386.

12. Kan, H.; Chau, K.; Cheng, M. In *Development of doubly salient permanent magnet motor flywheel energy storage for building integrated photovoltaic system*, APEC 2001. Sixteenth Annual IEEE Applied Power Electronics Conference and Exposition (Cat. No. 01CH37181), IEEE: 2001; pp 314-320.

13. Kim, Y.-H.; Lee, K.-H.; Cho, Y.-H.; Hong, Y.-K. In *Comparison of harmonic compensation based on wound/squirrel-cage rotor type induction motors with flywheel*, Proceedings IPEMC 2000. Third International Power Electronics and Motion Control Conference (IEEE Cat. No. 00EX435), IEEE: 2000; pp 531-536.

14. Zhang, J.; Chen, Z.; Cai, L.; Zhao, Y. In *Flywheel energy storage system design for distribution network*, 2000 IEEE Power Engineering Society Winter Meeting. Conference Proceedings (Cat. No. 00CH37077), IEEE: 2000; pp 2619-2623.

15. Reiner, G.; Wehlau, N. In *Concept of a 50 MW/650 MJ power source based on industry-established MDS flywheel*, PPPS-2001 Pulsed Power Plasma Science 2001. 28th IEEE International Conference on Plasma Science and 13th IEEE International Pulsed Power Conference. Digest of Papers (Cat. No. 01CH37251), IEEE: 2001; pp 187-190.

16. Richard, T.; Belhomme, R.; Buchheit, N.; Gorgette, F. In *Power quality improvement case study of the connection of four 1.6 MVA flywheel dynamic UPS systems to a medium voltage distribution network*, 2001 IEEE/PES Transmission and Distribution Conference and Exposition. Developing New Perspectives (Cat. No. 01CH37294), IEEE: 2001; pp 253-258.

17. Aanstoos, T.; Kajs, J.; Brinkman, W.; Liu, H.; Ouroua, A.; Hayes, R.; Hearn, C.; Sarjeant, J.; Gill, H., High voltage stator for a flywheel energy storage system. *IEEE transactions on magnetics* **2001,** *37* (1), 242-247.

18. Akhil, A. A.; Huff, G.; Currier, A. B.; Kaun, B. C.; Rastler, D. M.; Chen, S. B.; Cotter, A. L.; Bradshaw, D. T.; Gauntlett, W. D., *DOE/EPRI 2013 electricity storage handbook in collaboration with NRECA*. Sandia National Laboratories Albuquerque, NM: 2013.

19. Cavallo, A., Controllable and affordable utility-scale electricity from intermittent wind resources and compressed air energy storage (CAES). *Energy* **2007,** *32* (2), 120-127.

20. Holden, P.; Moen, D.; DeCorso, M.; Howard, J. In *Alabama electric cooperative compressed air energy storage (CAES) plant improvements*, ASME Turbo Expo 2000: Power for Land, Sea, and Air, American Society of Mechanical Engineers Digital Collection: 2000.

21. Connolly, D., A review of energy storage technologies. *Ireland: University of Limerick* **2009**.

22. Dunn, B.; Kamath, H.; Tarascon, J.-M., Electrical energy storage for the grid: a battery of choices. *Science* **2011,** *334* (6058), 928-935.

23. Manwell, J. F.; McGowan, J. G., Lead acid battery storage model for hybrid energy systems. *Solar Energy* **1993,** *50* (5), 399-405.

24. Sebastián, R.; Alzola, R. P., Effective active power control of a high penetration wind diesel system with a Ni–Cd battery energy storage. *Renewable Energy* **2010,** *35* (5), 952-965.

25. Singh, M.; Cuenca, R.; Formento, J.; Gaines, L.; Marr, B.; Santini, D.; Wang, M.; Adelman, S.; Kline, D.; Mark, J., Total energy cycle assessment of electric and conventional vehicles: An energy and environmental analysis. *Argonne National Lab., National Renewable Energy Lab., and Pacific Northwest National Lab., US Dept. of Energy, Springfield, Virginia* **1998**.

26. Rantik, M., LIFE CYCLE ASSESSMENT OF FIVE BATTERIES FOR ELECTRIC VEHICLES UNDER DIFFERENT CHARGING REGIMES. **1999**.

27. Feng, F.; Geng, M.; Northwood, D., Electrochemical behaviour of intermetallic-based metal hydrides used in Ni/metal hydride (MH) batteries: a review. *International Journal of Hydrogen Energy* **2001,** *26* (7), 725-734.

28. De las Casas, C.; Li, W., A review of application of carbon nanotubes for lithium ion battery anode material. *Journal of Power Sources* **2012,** *208*, 74-85.

29. Etacheri, V.; Marom, R.; Elazari, R.; Salitra, G.; Aurbach, D., Challenges in the development of advanced Li-ion batteries: a review. *Energy & Environmental Science* **2011,** *4* (9), 3243-3262.

30. Grosjean, C.; Miranda, P. H.; Perrin, M.; Poggi, P., Assessment of world lithium resources and consequences of their geographic distribution on the expected development of the electric vehicle industry. *Renewable and Sustainable Energy Reviews* **2012,** *16* (3), 1735-1744.

31. Mine, I., "Mining Intelligence and Technology.

32. Moores, S.; Miller, A., Tesla battery plant will need 6 new flake graphite mines. *Industrial Minerals. Available from:< http://www. indmin. com/Article/3315690/Tesla-battery-plant-will-need-6-new-flake-graphite-mines. html* **2014**.

33. Sulfur Price, National Iranian Gas Company. **2014**.

34. Levene, J. I.; Mann, M. K.; Margolis, R. M.; Milbrandt, A., An analysis of hydrogen production from renewable electricity sources. *Solar Energy* **2007,** *81* (6), 773-780.

35. Chu, A.; Braatz, P., Comparison of commercial supercapacitors and high-power lithium-ion batteries for power-assist applications in hybrid electric vehicles: I. Initial characterization. *Journal of power sources* **2002,** *112* (1), 236-246.

36. Nikolaidis, P.; Poullikkas, A., A comparative review of electrical energy storage systems for better sustainability. *Journal of power technologies* **2017**.

37. Ferrier, M., Stockage d'energie dans un enroulement supraconducteur. *International Institute of Refrigeration, Low Temperatures and Electric Power, London* **1970**, 425-432.

38. Chen, H.; Cong, T. N.; Yang, W.; Tan, C.; Li, Y.; Ding, Y., Progress in electrical energy storage system: A critical review. *Progress in natural science* **2009,** *19* (3), 291-312.

39. Buckles, W.; Hassenzahl, W. V., Superconducting magnetic energy storage. *IEEE Power Engineering Review* **2000,** *20* (5), 16-20.

40. Ibrahim, H.; Ilinca, A.; Perron, J., Energy storage systems—Characteristics and comparisons. *Renewable and sustainable energy reviews* **2008,** *12* (5), 1221-1250.

41. Tixador, P. In *Superconducting magnetic energy storage: Status and perspective*, IEEE/CSC&ESAS European superconductivity news forum, 2008.

42. Naish, C.; McCubbin, I.; Edberg, O.; Harfoot, M., Outlook of energy storage technologies. *European Parliament, Policy Department, Economic and Scientific Policy* **2008**.

43. Luo, X.; Wang, J.; Dooner, M.; Clarke, J., Overview of current development in electrical energy storage technologies and the application potential in power system operation. *Applied energy* **2015,** *137*, 511-536.

44. Meister, P.; Jia, H.; Li, J.; Kloepsch, R.; Winter, M.; Placke, T., Best practice: performance and cost evaluation of lithium ion battery active materials with special emphasis on energy efficiency. *Chemistry of Materials* **2016,** *28* (20), 7203-7217.

45. Burchell, T. D., *Carbon materials for advanced technologies*. Elsevier: 1999.

46. Unwin, P. R.; Güell, A. G.; Zhang, G., Nanoscale electrochemistry of sp2 carbon materials: from graphite and graphene to carbon nanotubes. *Accounts of chemical research* **2016,** *49* (9), 2041-2048.

47. McClure, J., Theory of diamagnetism of graphite. *Physical review* **1960,** *119* (2), 606.

48. Agarwal, R. R.; Selman, J. R., Electrochemical Intercalation of Lithium in Graphite Using a Molten-Salt Cell. *ECS Proceedings Volumes* **1986,** *1986*, 377-388.

49. Dresselhaus, M. S., Fifty years in studying carbon-based materials. *Physica Scripta* **2012,** *2012* (T146), 014002.

50. Novoselov, K. S.; Geim, A. K.; Morozov, S. V.; Jiang, D.; Zhang, Y.; Dubonos, S. V.; Grigorieva, I. V.; Firsov, A. A., Electric field effect in atomically thin carbon films. *science* **2004,** *306* (5696), 666-669.

51. Dresselhaus, M.; Dresselhaus, G., Intercalation compounds of graphite. *Advances in Physics* **1981,** *30* (2), 139-326.

52. Iijima, S.; Ichihashi, T., Single-shell carbon nanotubes of 1-nm diameter. *nature* **1993,** *363* (6430), 603-605.

53. An, K. H.; Kim, W. S.; Park, Y. S.; Choi, Y. C.; Lee, S. M.; Chung, D. C.; Bae, D. J.; Lim, S. C.; Lee, Y. H., Supercapacitors using single-walled carbon nanotube electrodes. *Advanced Materials* **2001,** *13* (7), 497-500.

54. Peng, C.; Zhang, S.; Jewell, D.; Chen, G. Z., Carbon nanotube and conducting polymer composites for supercapacitors. *Progress in Natural science* **2008,** *18* (7), 777-788.

55. An, K. H.; Kim, W. S.; Park, Y. S.; Moon, J. M.; Bae, D. J.; Lim, S. C.; Lee, Y. S.; Lee, Y. H., Electrochemical properties of high-power supercapacitors using single-walled carbon nanotube electrodes. *Advanced functional materials* **2001,** *11* (5), 387-392.

56. Jia, X.; Kan, Y.; Zhu, X.; Ning, G.; Lu, Y.; Wei, F., Building flexible Li4Ti5O12/CNT lithium-ion battery anodes with superior rate performance and ultralong cycling stability. *Nano Energy* **2014,** *10*, 344-352.

57. Jia, X.; Yan, C.; Chen, Z.; Wang, R.; Zhang, Q.; Guo, L.; Wei, F.; Lu, Y., Direct growth of flexible LiMn 2 O 4/CNT lithium-ion cathodes. *Chemical Communications* **2011,** *47* (34), 9669-9671.

58. Huang, J.; Jiang, Z., The preparation and characterization of Li4Ti5O12/carbon nano-tubes for lithium ion battery. *Electrochimica Acta* **2008,** *53* (26), 7756-7759.

59. Shao, Y.; Yin, G.; Gao, Y.; Shi, P., Durability study of Pt / C and Pt / CNTs catalysts under simulated PEM fuel cell conditions. *Journal of the Electrochemical Society* **2006,** *153* (6), A1093-A1097.

60. Selvaraj, V.; Alagar, M.; Kumar, K. S., Synthesis and characterization of metal nanoparticles-decorated PPY–CNT composite and their electrocatalytic oxidation of formic acid and formaldehyde for fuel cell applications. *Applied Catalysis B: Environmental* **2007,** *75* (1-2), 129-138.

61. Zhang, W.; Chen, J.; Swiegers, G. F.; Ma, Z.-F.; Wallace, G. G., Microwave-assisted synthesis of Pt/CNT nanocomposite electrocatalysts for PEM fuel cells. *Nanoscale* **2010,** *2* (2), 282-286.

62. Balandin, A. A.; Ghosh, S.; Bao, W.; Calizo, I.; Teweldebrhan, D.; Miao, F.; Lau, C. N., Superior thermal conductivity of single-layer graphene. *Nano letters* **2008,** *8* (3), 902-907.

63. Lee, C.; Wei, X.; Kysar, J. W.; Hone, J., Measurement of the elastic properties and intrinsic strength of monolayer graphene. *science* **2008,** *321* (5887), 385-388.

64. Mo, R.; Li, F.; Tan, X.; Xu, P.; Tao, R.; Shen, G.; Lu, X.; Liu, F.; Shen, L.; Xu, B., High-quality mesoporous graphene particles as high-energy and fast-charging anodes for lithium-ion batteries. *Nature communications* **2019,** *10* (1), 1474.

65. Hu, L.-H.; Wu, F.-Y.; Lin, C.-T.; Khlobystov, A. N.; Li, L.-J., Graphene-modified LiFePO 4 cathode for lithium ion battery beyond theoretical capacity. *Nature communications* **2013,** *4*, 1687.

66. Luo, J.; Zhao, X.; Wu, J.; Jang, H. D.; Kung, H. H.; Huang, J., Crumpled graphene-encapsulated Si nanoparticles for lithium ion battery anodes. *The journal of physical chemistry letters* **2012,** *3* (13), 1824-1829.

67. Villar-Rodil, S.; Paredes, J. I.; Martínez-Alonso, A.; Tascón, J. M., Preparation of graphene dispersions and graphene-polymer composites in organic media. *Journal of Materials Chemistry* **2009,** *19* (22), 3591-3593.

68. Du, J.; Cheng, H. M., The fabrication, properties, and uses of graphene/polymer composites. *Macromolecular Chemistry and Physics* **2012,** *213* (10-11), 1060-1077.

69. Xia, F.; Mueller, T.; Lin, Y.-m.; Valdes-Garcia, A.; Avouris, P., Ultrafast graphene photodetector. *Nature nanotechnology* **2009,** *4* (12), 839.

70. Gan, X.; Shiue, R.-J.; Gao, Y.; Meric, I.; Heinz, T. F.; Shepard, K.; Hone, J.; Assefa, S.; Englund, D., Chip-integrated ultrafast graphene photodetector with high responsivity. *Nature Photonics* **2013,** *7* (11), 883.

71. Wyckoff, R. W., Crystal Structures, Vol. 1, Interscience Publ. *Inc., New York* **1963**.

72. Tománek, D.; Louie, S. G.; Mamin, H. J.; Abraham, D. W.; Thomson, R. E.; Ganz, E.; Clarke, J., Theory and observation of highly asymmetric atomic structure in scanning-tunneling-microscopy images of graphite. *Physical Review B* **1987,** *35* (14), 7790.

73. Chung, D., Review graphite. *Journal of materials science* **2002,** *37* (8), 1475-1489.

74. Spain, L., Electronic Properties of oriented graphite. *Philosophical Trans. Royal Soc., A* **1967,** *262*, 1128.

75. Yazami, R.; Touzain, P., A reversible graphite-lithium negative electrode for electrochemical generators. *Journal of Power Sources* **1983,** *9* (3), 365-371.

76. Cassagneau, T.; Fendler, J. H., High density rechargeable lithium-ion batteries self-assembled from graphite oxide nanoplatelets and polyelectrolytes. *Advanced Materials* **1998,** *10* (11), 877-881.

77. Eklund, P.; Dresselhaus, G.; Dresselhaus, M.; Fischer, J., Raman scattering from in-plane lattice modes in low-stage graphite-alkali-metal compounds. *Physical Review B* **1977,** *16* (8), 3330.

78. Zhao, W.; Tan, P. H.; Liu, J.; Ferrari, A. C., Intercalation of few-layer graphite flakes with FeCl3: Raman determination of Fermi level, layer decoupling and stability. *arXiv preprint arXiv:1012.1836* **2010**.

79. Dresselhaus, M. S.; Dresselhaus, G., Intercalation compounds of graphite. *Advances in physics* **2002,** *51* (1), 1-186.

80. Xiu-Yun, C., Graphene-like nanosheets synthesized by natural flaky graphite in Shandong, China. *International Nano Letters* **2013,** *3* (1), 6.

81. Skowroński, J.; Rozmanowski, T.; Krawczyk, P., Enhancement of electrochemical hydrogen storage in NiCl 2–FeCl 3–PdCl 2–graphite intercalation compound effected by chemical exfoliation. *Applied Surface Science* **2013,** *275*, 282-288.

82. Skowroński, J. M.; Krawczyk, P.; Rozmanowski, T.; Urbaniak, J., Electrochemical behavior of exfoliated NiCl 2–graphite intercalation compound affected by hydrogen sorption. *Energy Conversion and Management* **2008,** *49* (9), 2440-2446.

83. Iijima, S., Helical microtubules of graphitic carbon. *nature* **1991,** *354* (6348), 56-58.

84. Miao, M., Electrical conductivity of pure carbon nanotube yarns. *Carbon* **2011,** *49* (12), 3755-3761.

85. Raccichini, R.; Varzi, A.; Passerini, S.; Scrosati, B., The role of graphene for electrochemical energy storage. *Nature materials* **2015,** *14* (3), 271-279.

86. Zhang, R.; Wen, Q.; Qian, W.; Su, D. S.; Zhang, Q.; Wei, F., Superstrong ultralong carbon nanotubes for mechanical energy storage. *Advanced materials* **2011,** *23* (30), 3387-3391.

87. Tang, C.; Zhang, Q.; Zhao, M.-Q.; Tian, G.-L.; Wei, F., Resilient aligned carbon nanotube/graphene sandwiches for robust mechanical energy storage. *Nano Energy* **2014,** *7*, 161-169.

88. Hill, F.; Havel, T.; Livermore, C., Modeling mechanical energy storage in springs based on carbon nanotubes. *Nanotechnology* **2009,** *20* (25), 255704.

89. Zhu, Y. G.; Wang, Y.; Shi, Y.; Wong, J. I.; Yang, H. Y., CoO nanoflowers woven by CNT network for high energy density flexible micro-supercapacitor. *Nano Energy* **2014,** *3*, 46-54.

90. Wang, Q.; Wen, Z.; Li, J., A hybrid supercapacitor fabricated with a carbon nanotube cathode and a TiO2–B nanowire anode. *Advanced Functional Materials* **2006,** *16* (16), 2141-2146.

91. Yu, C.; Masarapu, C.; Rong, J.; Wei, B.; Jiang, H., Stretchable supercapacitors based on buckled single-walled carbon-nanotube macrofilms. *Advanced Materials* **2009,** *21* (47), 4793-4797.

92. Varzi, A.; Bresser, D.; von Zamory, J.; Müller, F.; Passerini, S., ZnFe2O4-C/LiFePO4-CNT: A Novel High-Power Lithium-Ion Battery with Excellent Cycling Performance. *Advanced energy materials* **2014,** *4* (10), 1400054.

93. Wang, Y.; Tang, B.; Zhang, S., Single-walled carbon nanotube/phase change material composites: sunlight-driven, reversible, form-stable phase transitions for solar thermal energy storage. *Advanced Functional Materials* **2013,** *23* (35), 4354-4360.

94. Sarı, A.; Bicer, A.; Al-Sulaiman, F.; Karaipekli, A.; Tyagi, V., Diatomite/CNTs/PEG composite PCMs with shape-stabilized and improved thermal conductivity: Preparation and thermal energy storage properties. *Energy and Buildings* **2018,** *164*, 166-175.

95. Li, B.; Nie, S.; Hao, Y.; Liu, T.; Zhu, J.; Yan, S., Stearic-acid/carbon-nanotube composites with tailored shape-stabilized phase transitions and light–heat conversion for thermal energy storage. *Energy Conversion and Management* **2015,** *98*, 314-321.

96. Thostenson, E. T.; Ren, Z.; Chou, T.-W., Advances in the science and technology of carbon nanotubes and their composites: a review. *Composites science and technology* **2001,** *61* (13), 1899-1912.

97. Dresselhaus, M. S.; Dresselhaus, G.; Eklund, P. C., *Science of fullerenes and carbon nanotubes: their properties and applications*. Elsevier: 1996.

98. Saito, Y.; Nishikubo, K.; Kawabata, K.; Matsumoto, T., Carbon nanocapsules and single-layered nanotubes produced with platinum-group metals (Ru, Rh, Pd, Os, Ir, Pt) by arc discharge. *Journal of applied physics* **1996,** *80* (5), 3062-3067.

99. Collins, P. G.; Avouris, P., Nanotubes for electronics. *Scientific american* **2000,** *283* (6), 62-69.

100. Vajtai, R.; Wei, B.; Jung, Y. J.; Cao, A.; Biswas, S. K.; Ramanath, G.; Ajayan, P. M., Building and testing organized architectures of carbon nanotubes. *IEEE transactions on nanotechnology* **2003,** *2* (4), 355-361.

101. Raccichini, R.; Varzi, A.; Passerini, S.; Scrosati, B., The role of graphene for electrochemical energy storage. *Nature materials* **2015,** *14* (3).

102. Wu, Z.; Zhou, G.; Yin, L.; Ren, W.; Li, F.; Cheng, H., Graphene/metal oxide composite electrode materials for energy storage Nano Energy 2012, 1, 107–131. DOI.

103. Avouris, P., Graphene: electronic and photonic properties and devices. *Nano letters* **2010,** *10* (11), 4285-4294.

104. Schwierz, F., Graphene transistors. *Nature nanotechnology* **2010,** *5* (7), 487-496.

105. Avouris, P.; Chen, Z.; Perebeinos, V., Carbon-based electronics. *Nature nanotechnology* **2007,** *2* (10), 605-615.

106. Xia, F.; Mueller, T.; Golizadeh-Mojarad, R.; Freitag, M.; Lin, Y.-m.; Tsang, J.; Perebeinos, V.; Avouris, P., Photocurrent imaging and efficient photon detection in a graphene transistor. *arXiv preprint arXiv:0912.4788* **2009**.

107. Mueller, T.; Xia, F.; Avouris, P., Graphene photodetectors for high-speed optical communications. *Nature photonics* **2010,** *4* (5), 297-301.

108. Reed, G. T.; Mashanovich, G.; Gardes, F.; Thomson, D., Silicon optical modulators. *Nature photonics* **2010,** *4* (8), 518-526.

109. Xu, Y.; Lin, Z.; Zhong, X.; Huang, X.; Weiss, N. O.; Huang, Y.; Duan, X., Holey graphene frameworks for highly efficient capacitive energy storage. *Nature communications* **2014,** *5*, 4554.

110. Liu, F.; Song, S.; Xue, D.; Zhang, H., Folded structured graphene paper for high performance electrode materials. *Advanced Materials* **2012,** *24* (8), 1089-1094.

111. Wei, D.; Kivioja, J., Graphene for energy solutions and its industrialization. *Nanoscale* **2013,** *5* (21), 10108-10126.

112. Ohta, T.; Bostwick, A.; Seyller, T.; Horn, K.; Rotenberg, E., Controlling the electronic structure of bilayer graphene. *Science* **2006,** *313* (5789), 951-954.

113. Li, X.; Cai, W.; An, J.; Kim, S.; Nah, J.; Yang, D.; Piner, R.; Velamakanni, A.; Jung, I.; Tutuc, E., Large-area synthesis of high-quality and uniform graphene films on copper foils. *science* **2009,** *324* (5932), 1312-1314.

114. Miller, J. R.; Outlaw, R.; Holloway, B., Graphene double-layer capacitor with ac line-filtering performance. *Science* **2010,** *329* (5999), 1637-1639.

115. Chen, Z.; Ren, W.; Gao, L.; Liu, B.; Pei, S.; Cheng, H.-M., Three-dimensional flexible and conductive interconnected graphene networks grown by chemical vapour deposition. *Nature materials* **2011,** *10* (6), 424.

116. Tian, S.; Sun, J.; Yang, S.; He, P.; Wang, G.; Di, Z.; Ding, G.; Xie, X.; Jiang, M., Controllable Edge Oxidation and Bubbling Exfoliation Enable the Fabrication of High Quality Water Dispersible Graphene. *Scientific reports* **2016,** *6*.

117. Tian, S.; Sun, J.; Yang, S.; He, P.; Wang, G.; Di, Z.; Ding, G.; Xie, X.; Jiang, M., Controllable edge oxidation and bubbling exfoliation enable the fabrication of high quality water dispersible graphene. *Scientific reports* **2016,** *6*, 34127.

118. Novoselov, K. S.; Fal, V.; Colombo, L.; Gellert, P.; Schwab, M.; Kim, K., A roadmap for graphene. *nature* **2012,** *490* (7419), 192-200.

119. Voiry, D.; Yang, J.; Kupferberg, J.; Fullon, R.; Lee, C.; Jeong, H. Y.; Shin, H. S.; Chhowalla, M., High-quality graphene via microwave reduction of solution-exfoliated graphene oxide. *Science* **2016,** *353* (6306), 1413-1416.

120. Goodenough, J.; Abruna, H.; Buchanan, M. *Basic Research Needs for Electrical Energy Storage. Report of the Basic Energy Sciences Workshop on Electrical Energy Storage, April 2-4, 2007*; DOESC (USDOE Office of Science (SC)): 2007.

121. Roy, P.; Srivastava, S. K., Nanostructured anode materials for lithium ion batteries. *Journal of Materials Chemistry A* **2015,** *3* (6), 2454-2484.

122. Wu, F.; Yushin, G., Conversion cathodes for rechargeable lithium and lithium-ion batteries. *Energy & Environmental Science* **2017,** *10* (2), 435-459.

123. Julien, C. M.; Mauger, A.; Zaghib, K.; Groult, H., Comparative issues of cathode materials for Li-ion batteries. *Inorganics* **2014,** *2* (1), 132-154.

124. Shim, J.-H.; Lee, K.-S.; Missyul, A.; Lee, J.; Linn, B.; Lee, E. C.; Lee, S., Characterization of Spinel Li x Co2O4-Coated LiCoO2 Prepared with Post-Thermal Treatment as a Cathode Material for Lithium Ion Batteries. *Chemistry of Materials* **2015,** *27* (9), 3273-3279.

125. Zheng, J.; Yan, P.; Cao, R.; Xiang, H.; Engelhard, M. H.; Polzin, B. J.; Wang, C.; Zhang, J.-G.; Xu, W., Effects of Propylene Carbonate Content in CsPF6-Containing Electrolytes on the Enhanced Performances of Graphite Electrode for Lithium-Ion Batteries. *ACS applied materials & interfaces* **2016,** *8* (8), 5715-5722.

126. Kunduraci, M.; Al-Sharab, J. F.; Amatucci, G. G., High-Power Nanostructured LiMn2-x Ni x O4 High-Voltage Lithium-Ion Battery Electrode Materials: Electrochemical Impact of Electronic Conductivity and Morphology. *Chemistry of materials* **2006,** *18* (15), 3585-3592.

127. Kunduraci, M.; Amatucci, G., Synthesis and characterization of nanostructured 4.7 V Li x Mn1. 5Ni0. 5O4 spinels for high-power lithium-ion batteries. *Journal of The Electrochemical Society* **2006,** *153* (7), A1345-A1352.

128. Ellis, B. L.; Lee, K. T.; Nazar, L. F., Positive electrode materials for Li-ion and Li-batteries. *Chemistry of Materials* **2010,** *22* (3), 691-714.

129. Idris, M. S.; West, A., The effect on cathode performance of oxygen non-stoichiometry and interlayer mixing in layered rock salt LiNi0. 8Mn0. 1Co0. 1O2-δ. *Journal of The Electrochemical Society* **2012,** *159* (4), A396-A401.

130. Lee, S.-W.; Kim, H.; Kim, M.-S.; Youn, H.-C.; Kang, K.; Cho, B.-W.; Roh, K. C.; Kim, K.-B., Improved electrochemical performance of LiNi 0.6 Co 0.2 Mn 0.2 O 2 cathode material synthesized by citric acid assisted sol-gel method for lithium ion batteries. *Journal of Power Sources* **2016,** *315*, 261-268.

131. Fergus, J. W., Recent developments in cathode materials for lithium ion batteries. *Journal of Power Sources* **2010,** *195* (4), 939-954.

132. Pouillerie, v. C.; Croguennec, L.; Delmas, C., The Li x Ni 1− y Mg y O 2 (y= 0.05, 0.10) system: structural modifications observed upon cycling. *Solid State Ionics* **2000,** *132* (1), 15-29.

133. Yuan, S.; Liu, L. B.; Tang, Y. P.; Wang, J. H.; Guo, Y. Z. In *Synthesis and Electrochemical Properties of Cathode Material LiNi0. 8Co0. 1Mn0. 1O2 via Li, Mg, Al Dopping*, Advanced Materials Research, Trans Tech Publ: 2014; pp 302-306.

134. Chen, Y.; Zhang, Y.; Chen, B.; Wang, Z.; Lu, C., An approach to application for LiNi 0.6 Co 0.2 Mn 0.2 O 2 cathode material at high cutoff voltage by TiO 2 coating. *Journal of Power Sources* **2014,** *256*, 20-27.

135. Zheng, J.; Wu, X.; Yang, Y., Improved electrochemical performance of Li [Li 0.2 Mn 0.54 Ni 0.13 Co 0.13] O 2 cathode material by fluorine incorporation. *Electrochimica Acta* **2013,** *105*, 200-208.

136. Thackeray, M. M.; Kang, S.-H.; Johnson, C. S.; Vaughey, J. T.; Benedek, R.; Hackney, S., Li 2 MnO 3-stabilized LiMO 2 (M= Mn, Ni, Co) electrodes for lithium-ion batteries. *Journal of Materials chemistry* **2007,** *17* (30), 3112-3125.

137. Zheng, J.; Gu, M.; Xiao, J.; Zuo, P.; Wang, C.; Zhang, J.-G., Corrosion/fragmentation of layered composite cathode and related capacity/voltage fading during cycling process. *Nano letters* **2013,** *13* (8), 3824-3830.

138. Zheng, J.; Shi, W.; Gu, M.; Xiao, J.; Zuo, P.; Wang, C.; Zhang, J.-G., Electrochemical kinetics and performance of layered composite cathode material Li [Li0. 2Ni0. 2Mn0. 6] O2. *Journal of The Electrochemical Society* **2013,** *160* (11), A2212-A2219.

139. Balogun, M.-S.; Luo, Y.; Qiu, W.; Liu, P.; Tong, Y., A review of carbon materials and their composites with alloy metals for sodium ion battery anodes. *Carbon* **2016,** *98*, 162-178.

140. Chan, C. K.; Peng, H.; Liu, G.; McIlwrath, K.; Zhang, X. F.; Huggins, R. A.; Cui, Y., High-performance lithium battery anodes using silicon nanowires. *Nature nanotechnology* **2008,** *3* (1), 31.

141. Chen, X.; Du, Y.; Zhang, N. Q.; Sun, K. N., 3D self-supported nanoarchitectured arrays electrodes for lithium-ion batteries. *Journal of Nanomaterials* **2012,** *2012*.

142. Dong, Y.; Liu, S.; Liu, Y.; Tang, Y.; Yang, T.; Wang, X.; Wang, Z.; Zhao, Z.; Qiu, J., Rational design of metal oxide hollow nanostructures decorated carbon nanosheets for superior lithium storage. *Journal of Materials Chemistry A* **2016,** *4* (45), 17718-17725.

143. Lee, J. K.; Oh, C.; Kim, N.; Hwang, J.-Y.; Sun, Y.-K., Rational design of silicon-based composites for high-energy storage devices. *Journal of Materials Chemistry A* **2016,** *4* (15), 5366-5384.

144. Qi, W.; Shapter, J. G.; Wu, Q.; Yin, T.; Gao, G.; Cui, D., Nanostructured anode materials for lithium-ion batteries: principle, recent progress and future perspectives. *Journal of Materials Chemistry A* **2017,** *5* (37), 19521-19540.

145. Liu, D.; Cao, G., Engineering nanostructured electrodes and fabrication of film electrodes for efficient lithium ion intercalation. *Energy & Environmental Science* **2010,** *3* (9), 1218-1237.

146. Maier, J., Nanoionics: ion transport and electrochemical storage in confined systems. *Nature materials* **2005,** *4* (11), 805-815.

147. Bruce, P. G., Energy storage beyond the horizon: Rechargeable lithium batteries. *Solid State Ionics* **2008,** *179* (21-26), 752-760.

148. Kim, N.; Chae, S.; Ma, J.; Ko, M.; Cho, J., Fast-charging high-energy lithium-ion batteries via implantation of amorphous silicon nanolayer in edge-plane activated graphite anodes. *Nature communications* **2017,** *8* (1), 1-10.

149. Liu, N.; Wu, H.; McDowell, M. T.; Yao, Y.; Wang, C.; Cui, Y., A yolk-shell design for stabilized and scalable Li-ion battery alloy anodes. *Nano letters* **2012,** *12* (6), 3315-3321.

150. Winter, M.; Besenhard, J. O.; Spahr, M. E.; Novak, P., Insertion electrode materials for rechargeable lithium batteries. *Advanced materials* **1998,** *10* (10), 725-763.

151. Huggins, R. A., Use of Polymeric Materials As Battery Components. *Advanced Batteries: Materials Science Aspects* **2009**, 433-440.

152. Wang, F.; Yi, J.; Wang, Y.; Wang, C.; Wang, J.; Xia, Y., Graphite intercalation compounds (GICs): a new type of promising anode material for lithium - ion batteries. *Advanced Energy Materials* **2014,** *4* (2), 1300600.

153. Zhao, J.; Buldum, A.; Han, J.; Lu, J. P., First-principles study of Li-intercalated carbon nanotube ropes. *Physical review letters* **2000,** *85* (8), 1706.

154. Senami, M.; Ikeda, Y.; Fukushima, A.; Tachibana, A., Theoretical study of adsorption of lithium atom on carbon nanotube. *AIP Advances* **2011,** *1* (4), 042106.

155. Ji, L.; Lin, Z.; Alcoutlabi, M.; Zhang, X., Recent developments in nanostructured anode materials for rechargeable lithium-ion batteries. *Energy & Environmental Science* **2011,** *4* (8), 2682-2699.

156. Wang, X. X.; Wang, J. N.; Chang, H.; Zhang, Y. F., Preparation of short carbon nanotubes and application as an electrode material in Li - ion batteries. *Advanced Functional Materials* **2007,** *17* (17), 3613-3618.

157. Frackowiak, E.; Gautier, S.; Gaucher, H.; Bonnamy, S.; Beguin, F., Electrochemical storage of lithium in multiwalled carbon nanotubes. *Carbon* **1999,** *37* (1), 61-69.

158. Xia, H.; Lai, M.; Lu, L., Nanoflaky MnO 2/carbon nanotube nanocomposites as anode materials for lithium-ion batteries. *Journal of Materials Chemistry* **2010,** *20* (33), 6896-6902.

159. Wen, Z.; Ci, S.; Mao, S.; Cui, S.; He, Z.; Chen, J., CNT@ TiO 2 nanohybrids for high-performance anode of lithium-ion batteries. *Nanoscale research letters* **2013,** *8* (1), 1-6.

160. Wang, B.; Xin, H.; Li, X.; Cheng, J.; Yang, G.; Nie, F., Mesoporous CNT@ TiO 2-C nanocable with extremely durable high rate capability for lithium-ion battery anodes. *Scientific reports* **2014,** *4*, 3729.

161. Shi, Y.; Wang, Y.; Wong, J. I.; Tan, A. Y. S.; Hsu, C.-L.; Li, L.-J.; Lu, Y.-C.; Yang, H. Y., Self-assembly of hierarchical MoS x/CNT nanocomposites (2< x< 3): towards high performance anode materials for lithium ion batteries. *Scientific reports* **2013,** *3*, 2169.

162. Bindumadhavan, K.; Srivastava, S. K.; Mahanty, S., MoS 2–MWCNT hybrids as a superior anode in lithium-ion batteries. *Chemical Communications* **2013,** *49* (18), 1823-1825.

163. Zhang, J.; Xie, Z.; Li, W.; Dong, S.; Qu, M., High-capacity graphene oxide/graphite/carbon nanotube composites for use in Li-ion battery anodes. *Carbon* **2014,** *74*, 153-162.

164. Yan, Y.; Li, C.; Liu, C.; Mutlu, Z.; Dong, B.; Liu, J.; Ozkan, C. S.; Ozkan, M., Bundled and dispersed carbon nanotube assemblies on graphite superstructures as free-standing lithium-ion battery anodes. *Carbon* **2019,** *142*, 238-244.

165. Fan, Z.-J.; Yan, J.; Wei, T.; Ning, G.-Q.; Zhi, L.-J.; Liu, J.-C.; Cao, D.-X.; Wang, G.-L.; Wei, F., Nanographene-constructed carbon nanofibers grown on graphene sheets by chemical vapor deposition: high-performance anode materials for lithium ion batteries. *ACS nano* **2011,** *5* (4), 2787-2794.

166. Ferg, E.; Gummow, R.; De Kock, A.; Thackeray, M., Spinel anodes for lithium-ion batteries. *Journal of the Electrochemical Society* **1994,** *141* (11), L147.

167. Yin, S.; Song, L.; Wang, X.; Zhang, M.; Zhang, K.; Zhang, Y., Synthesis of spinel Li4Ti5O12 anode material by a modified rheological phase reaction. *Electrochimica acta* **2009,** *54* (24), 5629-5633.

168. Yao, Z.; Xia, X.; Xie, D.; Wang, Y.; Zhou, C. a.; Liu, S.; Deng, S.; Wang, X.; Tu, J., Enhancing ultrafast lithium ion storage of Li4Ti5O12 by tailored TiC/C core/shell skeleton plus nitrogen doping. *Advanced Functional Materials* **2018,** *28* (31), 1802756.

169. Jaiswal, A.; Horne, C.; Chang, O.; Zhang, W.; Kong, W.; Wang, E.; Chern, T.; Doeff, M., Nanoscale LiFePO4 and Li4Ti5O12 for high rate Li-ion batteries. *Journal of The Electrochemical Society* **2009,** *156* (12), A1041-A1046.

170. Li, H.; Huang, X.; Chen, L.; Wu, Z.; Liang, Y., A high capacity nano Si composite anode material for lithium rechargeable batteries. *Electrochemical and solid-state letters* **1999,** *2* (11), 547-549.

171. Kim, H.; Seo, M.; Park, M. H.; Cho, J., A critical size of silicon nano-anodes for lithium rechargeable batteries. *Angewandte Chemie International Edition* **2010,** *49* (12), 2146-2149.

172. Chen, S.; Chen, Z.; Xu, X.; Cao, C.; Xia, M.; Luo, Y., Scalable 2D Mesoporous Silicon Nanosheets for High-Performance Lithium-Ion Battery Anode. *Small* **2018,** *14* (12), 1703361.

173. Kucinskis, G.; Bajars, G.; Kleperis, J., Graphene in lithium ion battery cathode materials: A review. *Journal of Power Sources* **2013,** *240*, 66-79.

174. Zhang, Y.; Zhang, K.; Jia, K.; Liu, G.; Ren, S.; Li, K.; Long, X.; Li, M.; Qiu, J., Preparation of coal-based graphene quantum dots/α-Fe2O3 nanocomposites and their lithium-ion storage properties. *Fuel* **2019,** *241*, 646-652.

175. Lin, J.; Peng, Z.; Xiang, C.; Ruan, G.; Yan, Z.; Natelson, D.; Tour, J. M., Graphene nanoribbon and nanostructured SnO2 composite anodes for lithium ion batteries. *ACS nano* **2013,** *7* (7), 6001-6006.

176. Li, L.; Raji, A. R. O.; Tour, J. M., Graphene - Wrapped MnO2 – Graphene Nanoribbons as Anode Materials for High - Performance Lithium Ion Batteries. *Advanced Materials* **2013,** *25* (43), 6298-6302.

177. Yang, Y.; Li, L.; Fei, H.; Peng, Z.; Ruan, G.; Tour, J. M., Graphene nanoribbon/V2O5 cathodes in lithium-ion batteries. *ACS applied materials & interfaces* **2014,** *6* (12), 9590-9594.

178. Ding, Y.; Jiang, Y.; Xu, F.; Yin, J.; Ren, H.; Zhuo, Q.; Long, Z.; Zhang, P., Preparation of nano-structured LiFePO4/graphene composites by co-precipitation method. *Electrochemistry Communications* **2010,** *12* (1), 10-13.

179. Wu, K.; Hu, G.; Du, K.; Peng, Z.; Cao, Y., Improved electrochemical properties of LiFePO4/graphene/carbon composite synthesized from FePO4· 2H2O/graphene oxide. *Ceramics International* **2015,** *41* (10), 13867-13871.

180. Wang, L.; Wang, H.; Liu, Z.; Xiao, C.; Dong, S.; Han, P.; Zhang, Z.; Zhang, X.; Bi, C.; Cui, G., A facile method of preparing mixed conducting LiFePO4/graphene composites for lithium-ion batteries. *Solid State Ionics* **2010,** *181* (37-38), 1685-1689.

181. Tian, Z.; Liu, S.; Ye, F.; Yao, S.; Zhou, Z.; Wang, S., Synthesis and characterization of LiFePO4 electrode materials coated by graphene. *Applied Surface Science* **2014,** *305*, 427-432.

182. De, S.; King, P. J.; Lotya, M.; O'Neill, A.; Doherty, E. M.; Hernandez, Y.; Duesberg, G. S.; Coleman, J. N., Flexible, transparent, conducting films of randomly stacked graphene from surfactant-stabilized, oxide-free graphene dispersions. *Small* **2010,** *6* (3), 458-464.

183. Yang, J.; Wang, J.; Tang, Y.; Wang, D.; Li, X.; Hu, Y.; Li, R.; Liang, G.; Sham, T.-K.; Sun, X., LiFePO 4–graphene as a superior cathode material for rechargeable lithium batteries: impact of stacked graphene and unfolded graphene. *Energy & Environmental Science* **2013,** *6* (5), 1521-1528.

184. Zhou, X.; Wang, F.; Zhu, Y.; Liu, Z., Graphene modified LiFePO 4 cathode materials for high power lithium ion batteries. *Journal of Materials Chemistry* **2011,** *21* (10), 3353-3358.

185. Yu, F.; Zhang, L.; Lai, L.; Zhu, M.; Guo, Y.; Xia, L.; Qi, P.; Wang, G.; Dai, B., High electrochemical performance of LiFePO4 cathode material via in-situ microwave exfoliated graphene oxide. *Electrochimica Acta* **2015,** *151*, 240-248.

186. Kim, M.-S.; Lee, G.-W.; Lee, S.-W.; Jeong, J. H.; Mhamane, D.; Roh, K. C.; Kim, K.-B., Synthesis of LiFePO4/graphene microspheres while avoiding restacking of graphene sheet's for high-rate lithium-ion batteries. *Journal of industrial and engineering chemistry* **2017,** *52*, 251-259.

187. Ji, D.; Zhou, H.; Tong, Y.; Wang, J.; Zhu, M.; Chen, T.; Yuan, A., Facile fabrication of MOF-derived octahedral CuO wrapped 3D graphene network as binder-free anode for high performance lithium-ion batteries. *Chemical Engineering Journal* **2017,** *313*, 1623-1632.

188. Mo, R.; Rooney, D.; Sun, K.; Yang, H. Y., 3D nitrogen-doped graphene foam with encapsulated germanium/nitrogen-doped graphene yolk-shell nanoarchitecture for high-performance flexible Li-ion battery. *Nature communications* **2017,** *8*, 13949.

189. Losurdo, M.; Giangregorio, M. M.; Capezzuto, P.; Bruno, G., Graphene CVD growth on copper and nickel: role of hydrogen in kinetics and structure. *Physical Chemistry Chemical Physics* **2011,** *13* (46), 20836-20843.

190. Sutter, P., Epitaxial graphene: How silicon leaves the scene. *Nature materials* **2009,** *8* (3), 171.

191. Qi, X.; Qu, J.; Zhang, H.-B.; Yang, D.; Yu, Y.; Chi, C.; Yu, Z.-Z., FeCl 3 intercalated few-layer graphene for high lithium-ion storage performance. *Journal of Materials Chemistry A* **2015,** *3* (30), 15498-15504.

192. Zhang, B.; Song, J.; Yang, G.; Han, B., Large-scale production of high-quality graphene using glucose and ferric chloride. *Chemical science* **2014,** *5* (12), 4656-4660.

193. Lin, J.; Huang, Y.; Wang, S.; Chen, G., Microwave-assisted rapid exfoliation of graphite into graphene by using ammonium bicarbonate as the intercalation agent. *Industrial & Engineering Chemistry Research* **2017,** *56* (33), 9341-9346.

194. Pei, S.; Wei, Q.; Huang, K.; Cheng, H.-M.; Ren, W., Green synthesis of graphene oxide by seconds timescale water electrolytic oxidation. *Nature communications* **2018,** *9* (1), 1-9.

195. Yasin, G.; Arif, M.; Shakeel, M.; Dun, Y.; Zuo, Y.; Khan, W. Q.; Tang, Y.; Khan, A.; Nadeem, M., Exploring the Nickel–Graphene Nanocomposite Coatings for Superior Corrosion Resistance: Manipulating the Effect of Deposition Current Density on its Morphology, Mechanical Properties, and Erosion‐Corrosion Performance. *Advanced Engineering Materials* **2018,** *20* (7), 1701166.

196. Zhang, C.; Ma, J.; Han, F.; Liu, H.; Zhang, F.; Fan, C.; Liu, J.; Li, X., Strong anchoring effect of ferric chloride-graphite intercalation compounds (FeCl 3-GICs) with tailored epoxy groups for high-capacity and stable lithium storage. *Journal of Materials Chemistry A* **2018,** *6* (37), 17982-17993.

197. Zhang, H.; Shen, W.; Wang, Z.; Zhang, F., Formation of iron chloride-graphite intercalation compounds in propylene carbonate by electrolysis. *Carbon* **1997,** *35* (2), 285-290.

198. Shen, J.; Shi, M.; Yan, B.; Ma, H.; Li, N.; Ye, M., One-pot hydrothermal synthesis of Ag-reduced graphene oxide composite with ionic liquid. *Journal of Materials Chemistry* **2011,** *21* (21), 7795-7801.

199. Chen, I.-W. P.; Chen, Y.-S.; Kao, N.-J.; Wu, C.-W.; Zhang, Y.-W.; Li, H.-T., Scalable and high-yield production of exfoliated graphene sheets in water and its application to an all-solid-state supercapacitor. *Carbon* **2015,** *90*, 16-24.

200. Behabtu, N.; Lomeda, J. R.; Green, M. J.; Higginbotham, A. L.; Sinitskii, A.; Kosynkin, D. V.; Tsentalovich, D.; Parra-Vasquez, A. N. G.; Schmidt, J.; Kesselman, E., Spontaneous high-concentration dispersions and liquid crystals of graphene. *Nature nanotechnology* **2010,** *5* (6), 406-411.

201. Peng, L.; Xu, Z.; Liu, Z.; Wei, Y.; Sun, H.; Li, Z.; Zhao, X.; Gao, C., An iron-based green approach to 1-h production of single-layer graphene oxide. *Nature communications* **2015,** *6*, 5716.

202. Paton, K. R.; Varrla, E.; Backes, C.; Smith, R. J.; Khan, U.; O'Neill, A.; Boland, C.; Lotya, M.; Istrate, O. M.; King, P., Scalable production of large quantities of defect-free few-layer graphene by shear exfoliation in liquids. *Nature materials* **2014,** *13* (6), 624.

203. Lotya, M.; Hernandez, Y.; King, P. J.; Smith, R. J.; Nicolosi, V.; Karlsson, L. S.; Blighe, F. M.; De, S.; Wang, Z.; McGovern, I., Liquid phase production of graphene by exfoliation of graphite in surfactant/water solutions. *Journal of the American Chemical Society* **2009,** *131* (10), 3611-3620.

204. Khan, U.; O'Neill, A.; Lotya, M.; De, S.; Coleman, J. N., High-concentration solvent exfoliation of graphene. *Small* **2010,** *6* (7), 864-871.

205. Behabtu, N.; Lomeda, J. R.; Green, M. J.; Higginbotham, A. L.; Sinitskii, A.; Kosynkin, D. V.; Tsentalovich, D.; Parra-Vasquez, A. N. G.; Schmidt, J.; Kesselman, E., Spontaneous high-concentration dispersions and liquid crystals of graphene. *Nature nanotechnology* **2010,** *5* (6), 406.

206. Tung, T. T.; Yoo, J.; Alotaibi, F. K.; Nine, M. J.; Karunagaran, R.; Krebsz, M.; Nguyen, G. T.; Tran, D. N.; Feller, J.-F.; Losic, D., Graphene oxide-assisted liquid phase exfoliation of graphite into graphene for highly conductive film and electromechanical sensors. *ACS applied materials & interfaces* **2016,** *8* (25), 16521-16532.

207. Narayan, R.; Lim, J.; Jeon, T.; Li, D. J.; Kim, S. O., Perylene tetracarboxylate surfactant assisted liquid phase exfoliation of graphite into graphene nanosheets with facile re-dispersibility in aqueous/organic polar solvents. *Carbon* **2017,** *119*, 555-568.

208. Hernandez, Y.; Lotya, M.; Rickard, D.; Bergin, S. D.; Coleman, J. N., Measurement of Multicomponent Solubility Parameters for Graphene Facilitates Solvent Discovery. *Langmuir* **2010,** *26* (5), 3208-3213.

209. Das, S.; Wajid, A. S.; Shelburne, J. L.; Liao, Y.-C.; Green, M. J., Localized in-situ polymerization on graphene surfaces for stabilized graphene dispersions. *arXiv preprint arXiv:1011.1008* **2010**.

210. Palacin, M. R., Recent advances in rechargeable battery materials: a chemist's perspective. *Chemical Society Reviews* **2009,** *38* (9), 2565-2575.

211. Li, M.; Lu, J.; Chen, Z.; Amine, K., 30 years of lithium-ion batteries. *Advanced Materials* **2018,** *30* (33), 1800561.

212. Tarascon, J.-M.; Armand, M., Issues and challenges facing rechargeable lithium batteries. In *Materials for Sustainable Energy: A Collection of Peer-Reviewed Research and Review Articles from Nature Publishing Group*, World Scientific: 2011; pp 171-179.

213. Lu, L.; Han, X.; Li, J.; Hua, J.; Ouyang, M., A review on the key issues for lithium-ion battery management in electric vehicles. *Journal of power sources* **2013,** *226*, 272-288.

214. Millner, A. In *Modeling lithium ion battery degradation in electric vehicles*, 2010 IEEE Conference on Innovative Technologies for an Efficient and Reliable Electricity Supply, IEEE: 2010; pp 349-356.

215. Lu, J.; Chen, Z.; Ma, Z.; Pan, F.; Curtiss, L. A.; Amine, K., The role of nanotechnology in the development of battery materials for electric vehicles. *Nature nanotechnology* **2016,** *11* (12), 1031.

216. Chiang, Y.-M., Building a better battery. *Science* **2010,** *330* (6010), 1485-1486.

217. Simon, P.; Gogotsi, Y., Materials for electrochemical capacitors. In *Nanoscience And Technology: A Collection of Reviews from Nature Journals*, World Scientific: 2010; pp 320-329.

218. Kim, N.; Chae, S.; Ma, J.; Ko, M.; Cho, J., Fast-charging high-energy lithium-ion batteries via implantation of amorphous silicon nanolayer in edge-plane activated graphite anodes. *Nature communications* **2017,** *8* (1), 812.

219. Liu, K.; Liu, Y.; Lin, D.; Pei, A.; Cui, Y., Materials for lithium-ion battery safety. *Science advances* **2018,** *4* (6), eaas9820.

220. Doughty, D. H.; Roth, E. P., A general discussion of Li ion battery safety. *The Electrochemical Society Interface* **2012,** *21* (2), 37-44.

221. Padhi, A. K.; Nanjundaswamy, K. S.; Goodenough, J. B., Phospho - olivines as positive - electrode materials for rechargeable lithium batteries. *Journal of the electrochemical society* **1997,** *144* (4), 1188-1194.

222. Xie, H. M.; Wang, R. S.; Ying, J. R.; Zhang, L. Y.; Jalbout, A. F.; Yu, H. Y.; Yang, G. L.; Pan, X. M.; Su, Z. M., Optimized LiFePO4–polyacene cathode material for lithium - ion batteries. *Advanced Materials* **2006,** *18* (19), 2609-2613.

223. Wang, X.; Feng, Z.; Huang, J.; Deng, W.; Li, X.; Zhang, H.; Wen, Z., Graphene-decorated carbon-coated LiFePO4 nanospheres as a high-performance cathode material for lithium-ion batteries. *Carbon* **2018,** *127*, 149-157.

224. Chung, S.-Y.; Bloking, J. T.; Chiang, Y.-M., Electronically conductive phospho-olivines as lithium storage electrodes. *Nature materials* **2002,** *1* (2), 123.

225. Prosini, P. P.; Lisi, M.; Zane, D.; Pasquali, M., Determination of the chemical diffusion coefficient of lithium in LiFePO4. *Solid State Ionics* **2002,** *148* (1-2), 45-51.

226. Dean, C. R.; Young, A. F.; Meric, I.; Lee, C.; Wang, L.; Sorgenfrei, S.; Watanabe, K.; Taniguchi, T.; Kim, P.; Shepard, K. L., Boron nitride substrates for high-quality graphene electronics. *Nature nanotechnology* **2010,** *5* (10), 722.

227. Jiao, L.; Wang, X.; Diankov, G.; Wang, H.; Dai, H., Facile synthesis of high-quality graphene nanoribbons. *Nature nanotechnology* **2010,** *5* (5), 321.

228. Sofyan, N.; Setiadanu, G. T.; Zulfia, A.; Kartini, E., Effect of Different Calcination Temperatures and Carbon Coating on the Characteristics of LiFePO4 Prepared by Hydrothermal Route. *Int. J. Eng. Technol* **2017,** *9* (4), 3310-3317.

229. Takami, N.; Satoh, A.; Hara, M.; Ohsaki, T., Structural and kinetic characterization of lithium intercalation into carbon anodes for secondary lithium batteries. *Journal of The Electrochemical Society* **1995,** *142* (2), 371-379.

230. Levi, M. D.; Aurbach, D., Diffusion coefficients of lithium ions during intercalation into graphite derived from the simultaneous measurements and modeling of electrochemical impedance and potentiostatic intermittent titration characteristics of thin graphite electrodes. *The Journal of Physical Chemistry B* **1997,** *101* (23), 4641-4647.

231. Liu, Q.; Du, C.; Shen, B.; Zuo, P.; Cheng, X.; Ma, Y.; Yin, G.; Gao, Y., Understanding undesirable anode lithium plating issues in lithium-ion batteries. *RSC advances* **2016,** *6* (91), 88683-88700.

232. Li, X.; Yan, P.; Xiao, X.; Woo, J. H.; Wang, C.; Liu, J.; Zhang, J.-G., Design of porous Si/C–graphite electrodes with long cycle stability and controlled swelling. *Energy & Environmental Science* **2017,** *10* (6), 1427-1434.

233. Shearing, P. R.; Howard, L. E.; Jørgensen, P. S.; Brandon, N. P.; Harris, S. J., Characterization of the 3-dimensional microstructure of a graphite negative electrode from a Li-ion battery. *Electrochemistry communications* **2010,** *12* (3), 374-377.

234. Deng, T.; Zhou, X., The preparation of porous graphite and its application in lithium ion batteries as anode material. *Journal of Solid State Electrochemistry* **2016,** *20* (10), 2613-2618.

235. Billaud, J.; Bouville, F.; Magrini, T.; Villevieille, C.; Studart, A. R., Magnetically aligned graphite electrodes for high-rate performance Li-ion batteries. *Nature Energy* **2016,** *1* (8), 1-6.

236. Han, Y.-J.; Kim, J.; Yeo, J.-S.; An, J. C.; Hong, I.-P.; Nakabayashi, K.; Miyawaki, J.; Jung, J.-D.; Yoon, S.-H., Coating of graphite anode with coal tar pitch as an effective precursor for enhancing the rate performance in Li-ion batteries: Effects of composition and softening points of coal tar pitch. *Carbon* **2015,** *94*, 432-438.

237. Lee, M.-L.; Li, Y.-H.; Liao, S.-C.; Chen, J.-M.; Yeh, J.-W.; Shih, H. C., Li4Ti5O12-coated graphite as an anode material for lithium-ion batteries. *Applied surface science* **2012,** *258* (16), 5938-5942.

238. Lee, M.-L.; Li, Y. H.; Liao, S.-C.; Chen, J.-M.; Yeh, J.-W.; Shih, H. C., Li4Ti5O12-coated graphite anode materials for lithium-ion batteries. *Electrochimica Acta* **2013,** *112*, 529-534.

239. Gao, K.; Li, S.-D., Li4Ti5O12 coated graphite anodes with piperidinium-based hybrid electrolytes for lithium ion batteries. *Journal of Power Sources* **2014,** *270*, 304-311.

240. Kim, D. S.; Chung, D. J.; Bae, J.; Jeong, G.; Kim, H., Surface engineering of graphite anode material with black TiO2-x for fast chargeable lithium ion battery. *Electrochimica Acta* **2017,** *258*, 336-342.

241. Elias, D. C.; Nair, R. R.; Mohiuddin, T.; Morozov, S.; Blake, P.; Halsall, M.; Ferrari, A. C.; Boukhvalov, D.; Katsnelson, M.; Geim, A., Control of graphene's properties by reversible hydrogenation: evidence for graphane. *Science* **2009,** *323* (5914), 610-613.

242. Patnaik, S. G.; Vedarajan, R.; Matsumi, N., BIAN based functional diimine polymer binder for high performance Li ion batteries. *Journal of Materials Chemistry A* **2017,** *5* (34), 17909-17919.